

# **FY2002 Progress Summary, Program Plan, Statement of Work and Deliverables for Development of High Average Power Diode-Pumped Solid State Lasers, and Complementary Technologies, for Applications in Energy and Defense**

**U.S. Department of Energy**

Lawrence  
Livermore  
National  
Laboratory

*A. Bayramian, C. Bibeau, R. Beach, B. Behrendt, C. Ebbers, J. Latkowski, W. Meier, S. Payne, J. Perkins, K. Schaffers, K. Skulina, L. Hackel, J. Lindl, T. Ditmire, J. Kelly, L. Waxer, P. Rudi, M. Randles, D. Witter, H. Meissner, O. Meissner*

**December 13, 2001**

## DISCLAIMER

This document was prepared as an account of work sponsored by an agency of the United States Government. Neither the United States Government nor the University of California nor any of their employees, makes any warranty, express or implied, or assumes any legal liability or responsibility for the accuracy, completeness, or usefulness of any information, apparatus, product, or process disclosed, or represents that its use would not infringe privately owned rights. Reference herein to any specific commercial product, process, or service by trade name, trademark, manufacturer, or otherwise, does not necessarily constitute or imply its endorsement, recommendation, or favoring by the United States Government or the University of California. The views and opinions of authors expressed herein do not necessarily state or reflect those of the United States Government or the University of California, and shall not be used for advertising or product endorsement purposes.

This work was performed under the auspices of the U. S. Department of Energy by the University of California, Lawrence Livermore National Laboratory under Contract No. W-7405-Eng-48.

This report has been reproduced directly from the best available copy.

Available electronically at <http://www.doe.gov/bridge>

Available for a processing fee to U.S. Department of Energy  
and its contractors in paper from  
U.S. Department of Energy  
Office of Scientific and Technical Information  
P.O. Box 62  
Oak Ridge, TN 37831-0062  
Telephone: (865) 576-8401  
Facsimile: (865) 576-5728  
E-mail: [reports@adonis.osti.gov](mailto:reports@adonis.osti.gov)

Available for the sale to the public from  
U.S. Department of Commerce  
National Technical Information Service  
5285 Port Royal Road  
Springfield, VA 22161  
Telephone: (800) 553-6847  
Facsimile: (703) 605-6900  
E-mail: [orders@ntis.fedworld.gov](mailto:orders@ntis.fedworld.gov)  
Online ordering: <http://www.ntis.gov/ordering.htm>

OR

Lawrence Livermore National Laboratory  
Technical Information Department's Digital Library  
<http://www.llnl.gov/tid/Library.html>

**FY2002 Progress Summary, Program Plan,  
Statement of Work and Deliverables**

**For**

**Development of High Average Power  
Diode-Pumped Solid State Lasers,  
And Complementary Technologies,  
For Applications in Energy and Defense**

**Prepared by  
Lawrence Livermore National Laboratory**

**Presented to  
Ralph Schneider, DP/DOE,  
Virtual Office of Inertial Fusion Energy**

**Continuation of DOE Contract Number DE-AL03-94SF19892**

**For further information contact:**

**Dr. Stephen A. Payne**

**Laser Science and Technology Program**

**L-482**

**Lawrence Livermore National Laboratory**

**Livermore, CA 94550**

**Phone: (925) 423-0570**

**Fax: (925) 423-6195**

**payne3@llnl.gov**

As an Authorized Derivative Classifier, I have  
reviewed this information and verify that it  
does not contain classified information.

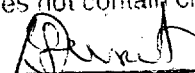


## TABLE OF CONTENTS

1. Introduction.....	3
2. Summary of Progress in FY2001.....	6
3. Descriptive Narrative of Program Plan in FY2001.....	67
4. Statements of Work and Deliverables for FY2002.....	78
5. Costing by Element for FY2002 Program.....	82
6. Contributors to this Plan.....	83

# 1. INTRODUCTION

The High Average Power Laser Program (HAPL) is a multi-institutional, coordinated effort to develop a high-energy, repetitively pulsed laser system for Inertial Fusion Energy and other DOE and DOD applications. This program is building a laser-fusion energy base to complement the laser-fusion science developed by DOE Defense programs over the past 25 years. The primary institutions responsible for overseeing and coordinating the research activities are the Naval Research Laboratory NRL and LLNL. The current LLNL proposal is a companion proposal to that submitted by (NRL), for which the driver development element is focused on the krypton fluoride excimer laser option. Aside from the driver development aspect, the NRL and LLNL companion proposals pursue complementary activities with the associated rep-rated laser technologies relating to target fabrication, target injection, final optics, fusion chamber, materials and power plant economics.

This report requests continued funding in FY02 to support LLNL in its program to build a 1kW, 100J, diode-pumped, crystalline laser. In addition, research in high gain laser target design, fusion chamber issues and survivability of the final optic element will be pursued. These technologies are crucial to the feasibility of inertial fusion energy power plants and also have relevance in rep-rated stewardship experiments.

The HAPL Program pursues technologies needed for laser-driven inertial fusion energy (IFE). System level considerations indicate that a rep-rated laser technology will be needed, operating at about 10Hz. Since a total energy of 2-4 MJ will ultimately be required to achieve a suitable target gain with direct drive targets, the architecture must be scaleable. The Mercury Laser is intended to offer such architecture – progress in FY01 and plans for FY02 appear in subsequent sections. Mercury is a solid state laser, which is pumped large diode arrays and employs a crystalline medium known as Yb:S-FAP. Yb:S-FAP offers highly desirable properties including favorable gain cross section, long energy storage time, and uniaxial crystalline structure (to mitigate thermally induced birefringence). The four-pass amplifier architecture minimizes beam modulation in optics, and suppresses ghost and pencil beams, amplified spontaneous emission, and reflections. Activities to incorporate beam smoothing, frequency conversion to  $3\omega$ , and pulse-shaping are also underway. During FY02, the emphasis is on continuing to produce large Yb:S-FAP crystals and powerful diode arrays, and activating the first amplifier head. High-speed gas cooling, previously verified to operate properly, is employed to cool the Yb:S-FAP laser slabs. The laser efficiency goal is 10%, in order for the recirculated power in an electrical plant to be manageable for anticipated levels of target gain.

A particular area of interest to Defense Programs lies in increasing the data base for high energy density plasma (HEDP) experiments such as radiation opacity and equation-of-state at high pressures. Data is typically gathered from large, single shot, expensive experiments which make it difficult to accumulate sufficient amounts of data. Repetitively pulsed systems offer shots-on-demand with flexibility in runtime settings (e.g. laser energy, target parameters, etc.). No such high-energy facility exists today, and the rep-rated technology to be developed would be advantageous. This is one of the goals of the High Average Power Laser program. The cutting edge attractiveness of this work to recruit young researchers and offer spin-off value to the DoD for directed-energy applications, is also desirable.

The scope of the current proposal is consistent with the goals outlined in the DPSSL five-year program plan, which was developed to create a pathway for scientific and engineering readiness to build and Integrated Research Experiment (IRE). The IRE, together with data on IFE technologies (e.g. chamber and final optic survival) and target physics validation on the NIF, is thought to be sufficient for proceeding to the next step of integration for making IFE a reality. Five-year plans were also developed for the Krypton Fluoride Laser at NRL. The plan calls for critical component development (Yb:S-FAP crystals, diodes, Pockels cell, frequency converter), demonstration of the 100 J Mercury Laser facility, and a multi-kilojoule IRE design. The DPSSL plan is shown in Fig. 1.1 below.

The end-goal of the Mercury Laser is to demonstrate 10% electrical efficiency at 10 Hz and 100 J with a 2-10 ns pulse length at the 1.047  $\mu\text{m}$  wavelength. The efficiency and rep-rate requirement relate

directly to inertial fusion energy objectives. We will be developing the beam quality technology for FY03 (spectral sculpting, bandwidth, temporal formatting, deformable mirror, transmissive phase masks) needed for Mercury to be a true user facility and for the full scale IRE program. When completed, Mercury will allow rep-rated target experiments with multiple target chambers for high energy density physics research. The primary FY02 goal is to activate one amplifier with 7 Yb:S-FAP slabs, build the second amplifier, and fabricate 7 additional slabs. Demonstration of the laser architecture with one power amplifier filled with seven Yb:S-FAP slabs will yield up to 20 J at 10 Hz. Experiments to benchmark our data against computational codes will also be performed.

### The 5 Year Plan for DPSSL Development

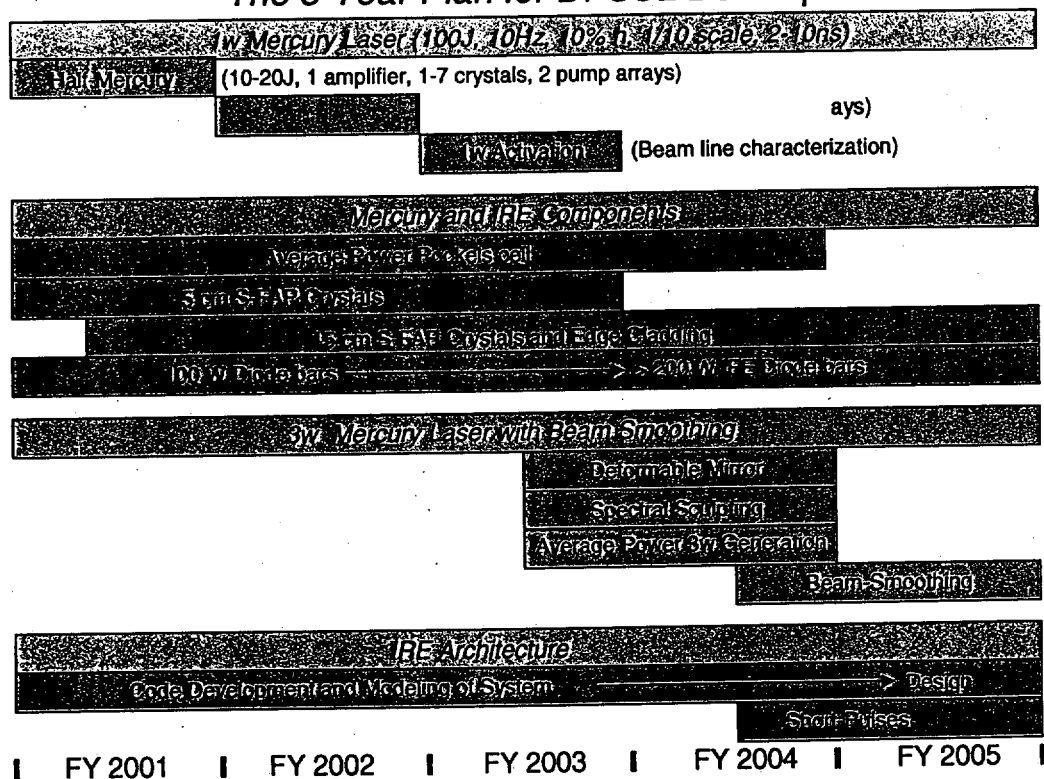


Fig. 1.1 Five-Year Plan for validation rep-rated DPSSL technology for IFE and DP.

In addition to the laser physics and engineering, additional areas to be pursued include target physics, chambers, system studies and final-optic/first-wall x-ray ablation. Target physics includes advanced direct-drive implosions (using a thin metal film) and determination of the "threat spectra" (i.e. x-ray, ions, debris  $n^\circ$  and gammas). The chamber study of the fast-ignitor will be explored to determine its potential for IFE. Radiation ( $n^\circ$  and  $\gamma$ ) physics studies of reflective and transmissive optics will be performed. A new initiative in x-ray ablation of optics and chambers will be started probably based on the use of a rep-rated z-pinch source. The cost of the entire program at LLNL is \$10,094,000. A detailed break-out of tasks is described in Sections 3 and 4.

The development of the Mercury Laser and evaluation of fusion chamber and final optic technologies, all have dual use applications to the defense and energy missions of the Department of Energy. The high average power lasers may be required to operate at  $\sim 10$  Hz, or simply in a shots-on-demand mode. Below we list the potential missions that may be served by the development of advanced target shooters and laser drivers:

- *Energy*
  - Driver development for achieving the scalability, efficiency, rep-rate, beam smoothness, and reliability required for power plant operation
  - Develop target tracking and injection, beam transport through chamber gases, and debris mitigation
  - X-ray ablation studies of candidate first-wall materials
  - Studies of beam uniformity (for direct drive) with time-resolved x-ray imaging of irradiated foils
  - Development of a radiation-hard final optic
- *National Security*
  - Ultra-precise equation-of-state and shock break-out measurements, as well as shock-induced phase change measurements, based on use of statistical averaging of x-ray probes
  - Fundamental pump-probe studies of nonlinear laser-plasma interactions (e.g. stimulated Raman and Brillouin scattering, and Thomson scattering probes) relevant in ICF targets
  - Three-dimensional x-ray tomographic imaging of nuclear components
  - Ultra-precise atomic absorption measurements based on extensive statistical averaging, for improved radiation transport modeling
- *National Ignition Facility technology*
  - Large area optical damage testing of NIF components
  - Calibration, fine-tuning and development of NIF x-ray and optical diagnostics
  - Debris assessment for various target materials and laser intensities
  - Pre-staging of NIF experiments, based on future availability of kJ-class "cheap shots"
  - Definition of laser technology for next-generation stockpile stewardship
- *Science Spin-Offs*
  - Development of laboratory x-ray lasers, including collisionally-excited plasmas
  - Relativistic propagation of laser beams in plasmas
  - Laser technology suitable for the next generation linear collider (see discussion below)
  - Three-dimension x-ray microscopy of biological and electronics samples
  - Synchrotron-like sources with higher brightness and accessibility
- *Department of Defense Spin-Offs*
  - Development of laser components such as high performance, low-cost laser diode arrays, large crystals, and cooling technology relevant to solid state laser tactical weapons (ground / ship / aircraft point-defense)
  - Space debris clearing by deflection (i.e. repetitive plasma impulse on debris in orbit)
  - Power beaming to recharge satellites in earth's shadow to prolong solar cell lifetime

Of the various spin-offs outlined above we have been actively working with several scientists involved in the planning stages of the Next Linear Collider (NLC). They have tentatively chosen the Mercury Laser architecture as the baseline system for creating short pulse, high repetition rate beams with near diffraction limited quality. The NLC will be used to probe basic particle structures through the production of high-energy gammas from collisions between high-energy electrons and extended "trains" of 1J energy pulses of approximately 2 picoseconds in duration. Twelve such lasers would have to be time multiplexed to achieve the NLC laser requirements.

In the long term, the goal is to develop the components of a power plant based on laser fusion, where the stringent requirements of driver efficiency, irradiation uniformity, and durability of  $>10^8$  shots, are paramount.

## **2. SUMMARY PROGRESS IN FY 2001**

### **TABLE OF CONTENTS**

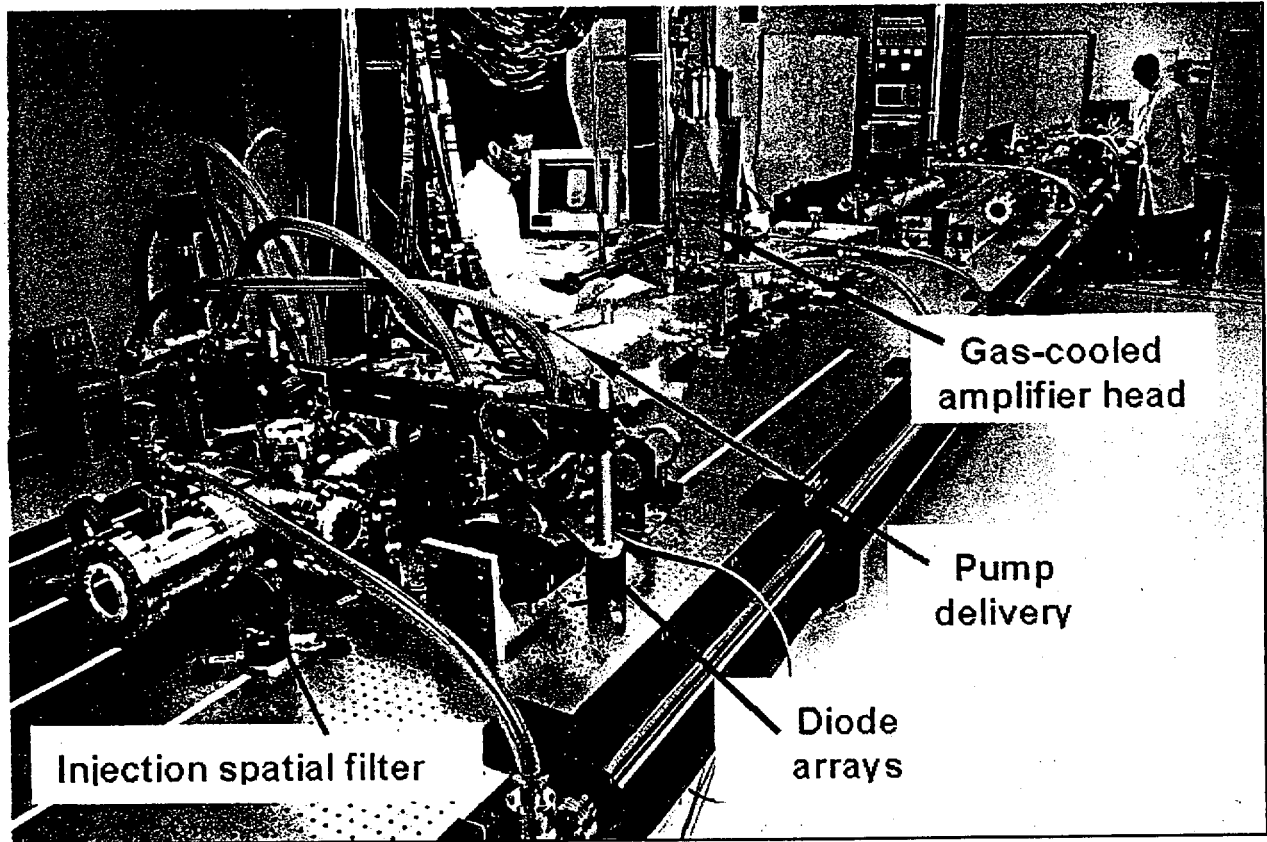
<b>2.1</b>	<b>DPSSL Development</b>	<b>7</b>
2.1.1	Mercury Laser Executive Summary	
2.1.2	Conceptual Layout and Gas Cooling	
2.1.3	Integration Experiments	
2.1.4	System Modeling	
2.1.5	Laser Diagnostics	
2.1.6	Pockels Cell Development	
2.1.7	Czochralski Crystal Growth	
2.1.8	Laser Diodes	
2.1.9	Diode Power Conditioning	
2.1.10	Computer Controls	
2.1.11	Laser Generation of Neutrons (University of Texas)	
2.1.12	Spectral Sculpting Experiments (University of Rochester)	
<b>2.2</b>	<b>Chambers</b>	<b>54</b>
2.2.1	Magnetic Protection	
2.2.2	Fast Ignition	
2.2.3	Safety and Environment	
2.2.4	Radiation Damage Modeling for Chamber Materials	
2.2.5	Systems Modeling	
<b>2.3</b>	<b>Final Optic</b>	<b>61</b>
2.3.1	Gamma and Neutron Irradiation Studies	
2.3.2	Molecular Dynamics Simulations of Neutron-Induced Defects	
2.3.3	X-Ray Ablation of Optical Materials	
<b>2.4</b>	<b>Target Physics</b>	<b>65</b>
<b>2.5</b>	<b>Table of Deliverables and Progress</b>	<b>66</b>



## 2.1 DPSSL Development

### 2.1.1 Mercury Laser Executive Summary

Our primary goals in FY2001 were to build and characterize the laser system with 320 kW of peak diode power (4 backplanes) and seven neodymium-doped glass slabs mounted in the gas cooled amplifier. The Nd:Glass slabs serve as surrogate material in the amplifier assembly until the Yb:S-FAP crystalline slabs are completed. The glass slabs are mounted in an aerodynamic aluminum vane structure to allow turbulent helium gas to flow across the faces. The concept of face cooling is advantageous over other technologies in that the thermal wavefront distortions are minimized, low order, and easily correctable. Measurements of the diode light delivery efficiency, uniformity, and polarization were made with 160 kW of diode power (2 backplanes). The remaining two backplanes were fabricated and are currently being assembled into the laser system for integrated tests. Propagation experiments of the seed beam through the amplifier were conducted along with the activation of the diagnostics packages. A picture of the laboratory is shown below along with callouts of the major components. In the final configuration, the Mercury laser will require two amplifiers in order to produce 100 J of 1.047  $\mu\text{m}$  light.



2.1.1.1 Mercury laser laboratory.

The growth and fabrication of the Yb:S-FAP slabs constitute another major element of our program objectives. Our goal was to produce at least 2 half sized defect free crystals, which could be bonded into one large 4x6 cm<sup>2</sup> crystal. Growth efforts at LLNL and at Northrop Grumman, our industrial collaborator, resulted in the production of 8 half-sized crystals that have been bonded together at ONYX

Optics Inc. to form 4 full-sized slabs. (Fig. 2.1.1.2) The slabs are in the final finishing and coating stages. Yb:S-FAP crystals were chosen as the preferred gain media to neodymium-doped glass because they offer higher energy storage, reducing laser diode cost, and a practical gain cross section. In addition, the high thermal conductivity of Yb:S-FAP permits operation at  $> 10$  Hz repetition rates. A total of 14 slabs will eventually be required for the two amplifiers.

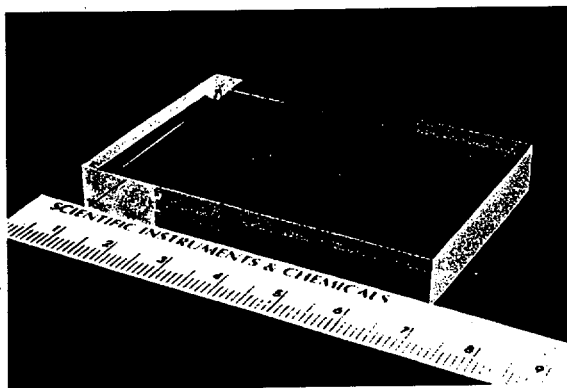


Fig. 2.1.1.2 A full sized Yb:S-FAP slab (amplifier medium) that has been bonded.

The diode bars needed to pump or excite the Yb:S-FAP crystals have been developed at Coherent Inc. and are now commercially available. The packaging technology, required to cool the diode bars was developed at LLNL (called V-BASIS), meets the stringent requirements pertaining to peak power, bandwidth, wavelength chirp and reliability. Our goal was to fabricate one-half or 144 of the diode packages or "tiles" needed for Mercury and mount them on a copper-cooling block. Over 150 tiles were fabricated and tested. Through a close relationship with Directed Energy Inc., of-the-shelf pulsers were upgraded to accommodate Mercury operating conditions and are now available commercially. A photograph showing the diodes firing at 10 Hz is shown in Fig. 2.1.1.3. Activation of the remaining two backplanes is imminent and will allow us to pump the surrogate glass slab from both sides.

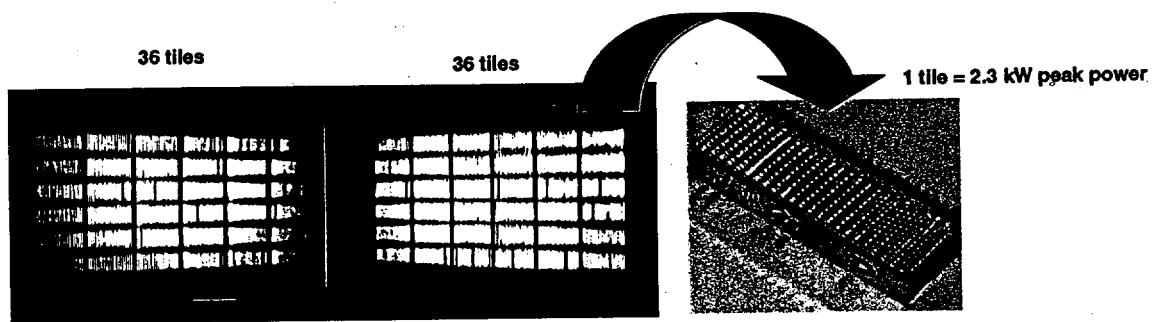


Fig. 2.1.1.3 A picture of diode tiles (pump laser) firing producing up to 160 kW of peak power at 900 nm.

The following sections discuss the above accomplishments in more technical detail and include component development, system modeling, and advanced crystal growth efforts with an industrial partner.

## 2.1.2 Conceptual Layout and Gas cooling

The conceptual layout for “half” of the laser is shown in Fig. 2.1.2.1. The overall layout employs an angularly multiplexed scheme with a front-end laser and a gas-cooled amplifier. The front-end laser is injected off-axis and near the focus to take advantage of angularly multiplexed concepts which avoid the use of optical switches at large apertures and high average powers at the output of the laser. After the beam is reflected back from the end mirror it returns to a different spatial location near the focus. A series of mirrors is used to reinject the beam back into the amplifier chain for two final passes. The image relay planes are located at the amplifier heads to reduce the probability of damage. The beam makes a total of 4 passes through the system.

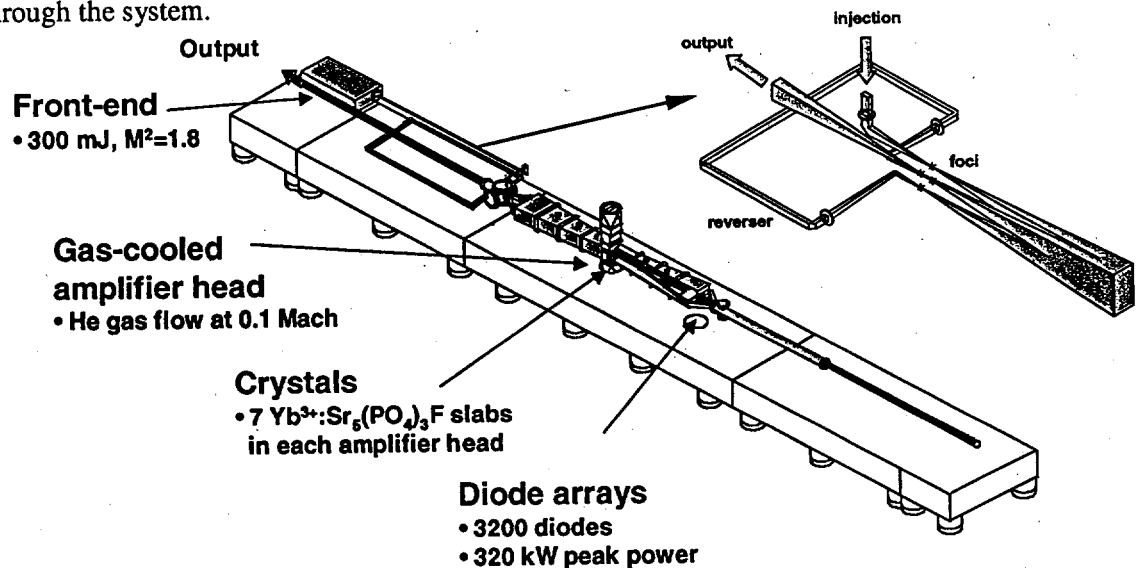


Fig. 2.1.2.1 Mercury laser system layout and enlargement of injection and reverser system.

The amplifier head is optically pumped from both sides. The dual pumping design allows for more uniform pumping and thermal loading on the crystals. The light from the diode array light is first condensed with a hollow lens duct followed by a hollow non-concentrating element that homogenizes spatial profile of the pump beam. Both the duct and the homogenizer are coated on the inside surfaces with a silver coating. The coating was chosen for its high reflectivity (>99%) at grazing incidence angles. The duct and homogenizer also serve to contain stray diode light. The light emerging from the output of the homogenizer is finally directed into the amplifier head to pump the Yb:S-FAP slabs.

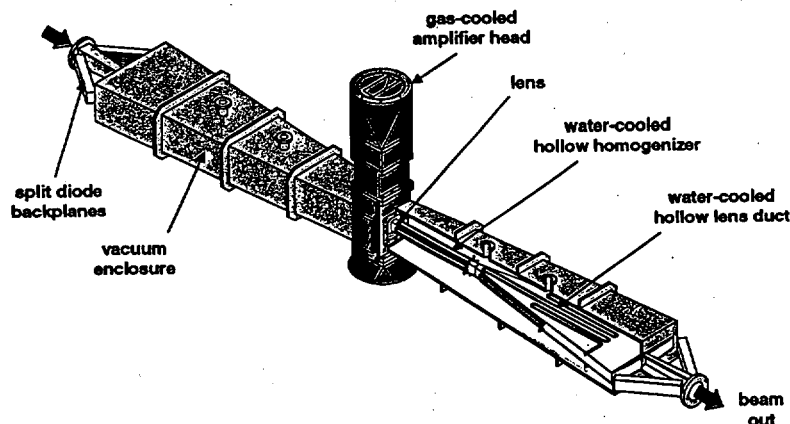


Fig. 2.1.2.2 Dual pumping geometry with 4 backplanes.

### ***Gas Cooled Amplifier with Wedged Slab Geometry***

The gas cooled amplifier head hardware was modified to allow for wedged-shaped amplifier slabs. The small wedge in the slabs was introduced to avoid etalon effects due to imperfect AR coatings. Studies have shown that the multiple reflections from the slab surfaces can lead to unwanted parasitic build-up of the reflected light in the amplifier chain.

The amplifier slabs ( $4 \times 6 \times 0.75 \text{ cm}^3$ ) are mounted or potted into aerodynamic aluminum vane elements as shown in Fig. 2.1.2.3a below. The seven vanes are precision mounted into a cassette (Fig. 2.1.2.3a that is inserted into the helium gas flow assembly.

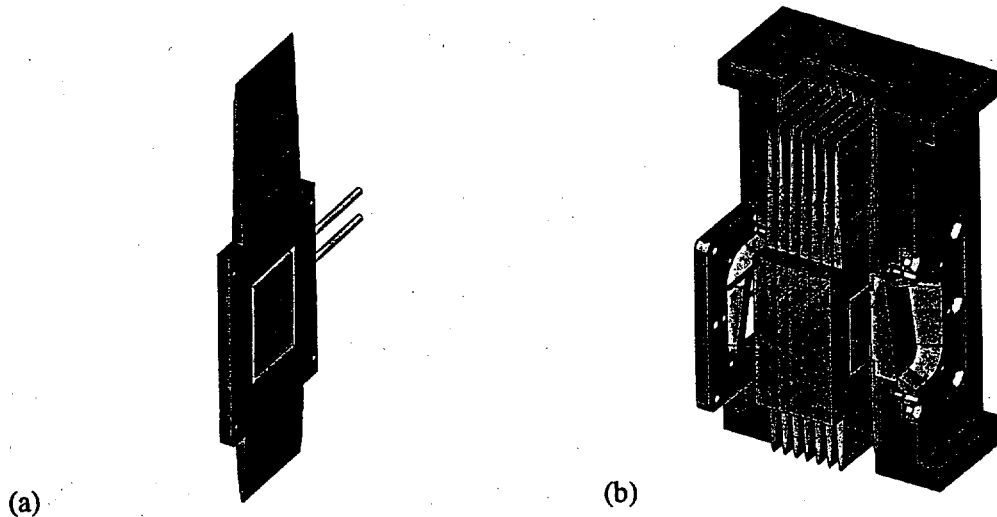


Fig. 2.1.2.3 (a) Single vane element, (b) Seven vane elements mounted into amplifier cassette

The vanes were fabricated in two sets: solid vanes (no cutout for slab) and hollow vanes (a cutout for slab). The solid vanes are being used in preliminary measurements to test whether the vane contours properly flow gas without inducing vibrations in the system. Aerodynamic considerations were preserved (as in the previous design) to include an acceleration section upstream and a trailing diffuser section for deceleration. The design minimizes flow induced optical distortions in the laser slabs in order to minimally impact laser performance. The solid vanes have been fabricated and are being flow tested in the helium gas system with 0.1 Mach flow conditions and 4 atmospheres of static pressure.

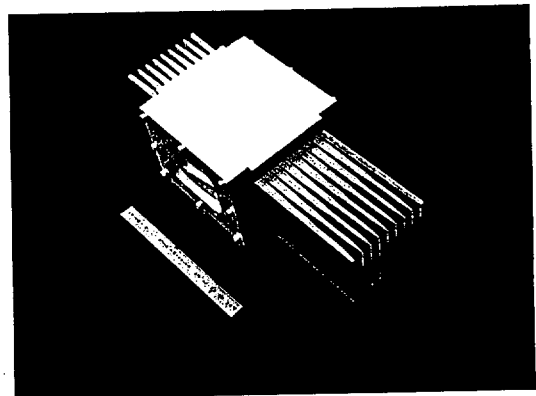
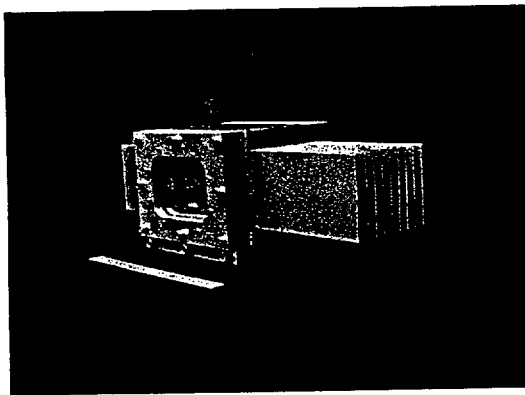


Fig. 2.1.2.4 Fabricated solid vanes will be used as surrogates for flow and vibration testing.

The hollow vanes have also been fabricated and are in the process of being inspected as shown in Fig. 2.1.2.4. We have established a new procedure for mounting the amplifier slabs in the vanes. In order to not perturb the flow, the slab must be mounted into the vane with a mating tolerance of  $<100\text{ }\mu\text{m}$ . Mock-up hardware fixtures were fabricated and results thus far indicate that we can mount the wedged slabs to within  $200\text{ }\mu\text{m}$ . We are working on improving our procedures and fixtures to bring the mating tolerance down by a factor of 2.

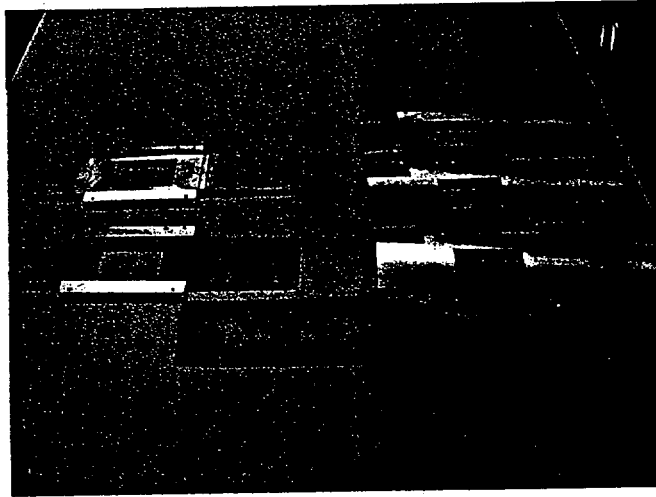


Fig. 2.1.2.5 Hollow vanes are being inspected and prepared for final surface finishing.

After tests with the solid vanes have been successfully completed, tests will be performed with the hollow vanes potted with wedged amplifier slabs. These tests will confirm whether the potting process causes any flow disturbances. Previous tests on non-wedged vanes were successful so we anticipate the experiments will go smoothly.

## 2.1.3 Integrated Experiments

Several measurements were made in the laboratory to test the pump delivery system and the integrated assembly of the pump delivery system with the amplifier assembly. We made good progress in benchmarking experimental data against our ray trace and energetics codes. The following three sections summarize our efforts.

### *Measurements of the pump light distribution, efficiency, and polarization*

The output pump light from the diode backplanes is highly divergent and spatially non-uniform which necessitates the use of additional optical elements to spatially smooth and shape the pump light profile. The design of our pump delivery system, shown in Fig. 2.1.3.1, incorporates a lens duct and homogenizer to accomplish this task. The purpose of the lens duct is to concentrate the light down to the desired aperture ( $3 \times 5 \text{ cm}^2$ ) and create a uniform divergence along both the x and y directions. The homogenizer serves to smooth the spatial profile without affecting the divergence. Both of these processes must be accomplished as efficiently as possible in order to maximize the transfer of the diode pump light onto the amplifier. Our initial integrated experiments were aimed towards: benchmarking our ray trace codes (which are used for creating input gain profiles for beam propagation codes and system design studies) and to evaluate the optical performance of the lens duct and homogenizer in term of hardware surface finish, reflectivity, and ease of alignment. The diode arrays and pump delivery system were assembled in the configuration shown in Fig. 2.1.3.1. Measurements of spatial uniformity were made using sheets of photo paper at image locations. The light scattered through the paper was then imaged onto a Photometrics CCD array capable of 16-bit operation over  $1024 \times 1024$  pixels allowing very high-resolution images. Direct imaging of the diode light onto the CCD array is not possible since the diode light is highly divergent at the output of the homogenizer and it is very difficult with imaging optics to adequately collect enough light into the camera.

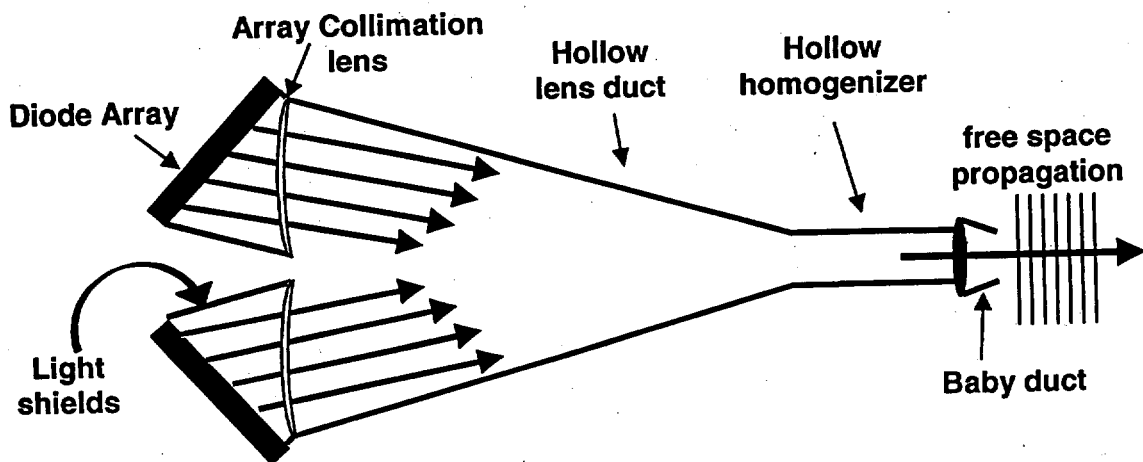


Fig. 2.1.3.1 A schematic illustrating the experimental arrangement for measuring the output energy, intensity profiles, and transfer efficiency of the diode pump delivery system. The lens shown in the above figure functions to collimate the laser light and does not greatly effect the diode light propagation. The so called "baby duct" is a temporary optic used to help guild the diode light into the amplifier assembly. It will be removed once the amplifier hardware is modified to allow the lens to be moved in closer to the amplifier assembly.

The experimental spatial profile at the output of the homogenizer is shown in Fig. 2.1.3.2 along with the ray-trace predictions generated from OPTICAD ray trace model. During our experiments we found that the diode backplanes require precision alignment, since as little as 0.1 degree tilt in the

backplanes can lead to spatial fluctuations in the intensity profile, clipping, and transmission losses of the diode light. This sensitivity arises from the long (1 m) length of the lens duct. We have since added finer adjustments to the hardware to allow for the precision alignment needed.

The model and experiment are in good agreement as can be seen by the lineouts in the vertical and horizontal directions. Each row of pixels is integrated to produce the vertical lineouts, and each column of pixels is integrated to produce the horizontal lineouts. This allows us to make a whole beam comparison.

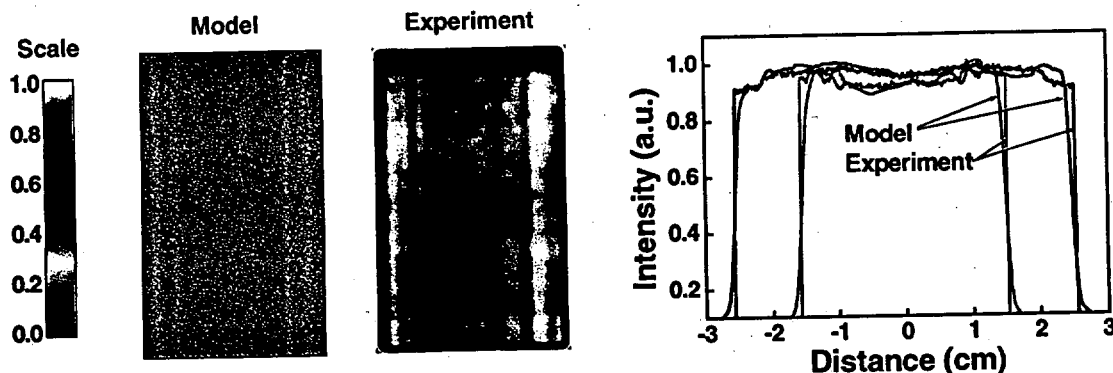


Fig. 2.1.3.2 Intensity maps of the output of the homogenizer showing a flat spatial pump profile and < 5% difference between theory and experiment.

Our next experiment was focused on determining the spatial pump intensity profile at each slab location within in the amplifier head. To accomplish this, we placed a sheet of photo paper at equivalent optical path length positions corresponding to the center of each of the slab. The diodes were fired and the light hitting the photo paper was imaged onto the CCD camera. The photo paper was moved to a new location and the experiment was repeated until all seven images ( $4 \times 6 \text{ cm}^2$ ) were captured. The results of the experiment are shown in Fig. 2.1.3.3a. The close agreement between the model with the data gives us confidence in our modeling capabilities and ability to produce individual 2-D gain profiles. The gain profiles are used in our propagation modeling (see Section 2.1.4) to predict energy output, intensity modulation, and wavefront distortions. In the fully assembled system the slabs would be pumped from both sides and the intensity maps would be more uniform than what is shown in Fig. 2.1.3.3a. With the ray-trace code benchmarked, we can include absorption and saturation effects and predict the gain profile for the entire amplifier (Fig. 2.1.3.3b). The smoothness of the predicted gain profile is acceptable for our system.

In a second set of experiments, we compared experimental data with theoretical predictions for the energy contained in a  $3 \times 5 \text{ cm}^2$  aperture at the same slab locations. This measurement allows us to determine the amount of diode light that reaches the slabs in the extracted area (dotted lines on  $4 \times 6 \text{ cm}^2$  image signify  $3 \times 5 \text{ cm}^2$  area). Transfer efficiency measurements were made with a Moletron PM5K-0615 water-cooled thermopile and a  $3 \times 5 \text{ cm}^2$  mask. The data is shown in Fig. 2.1.3.3c

Measurements taken of the polarization of the diode pump light exiting the homogenizer indicated that 98% of the light was polarized in the vertical direction. The crystals are oriented in the amplifier with the large gain cross section aligned with the vertical direction.

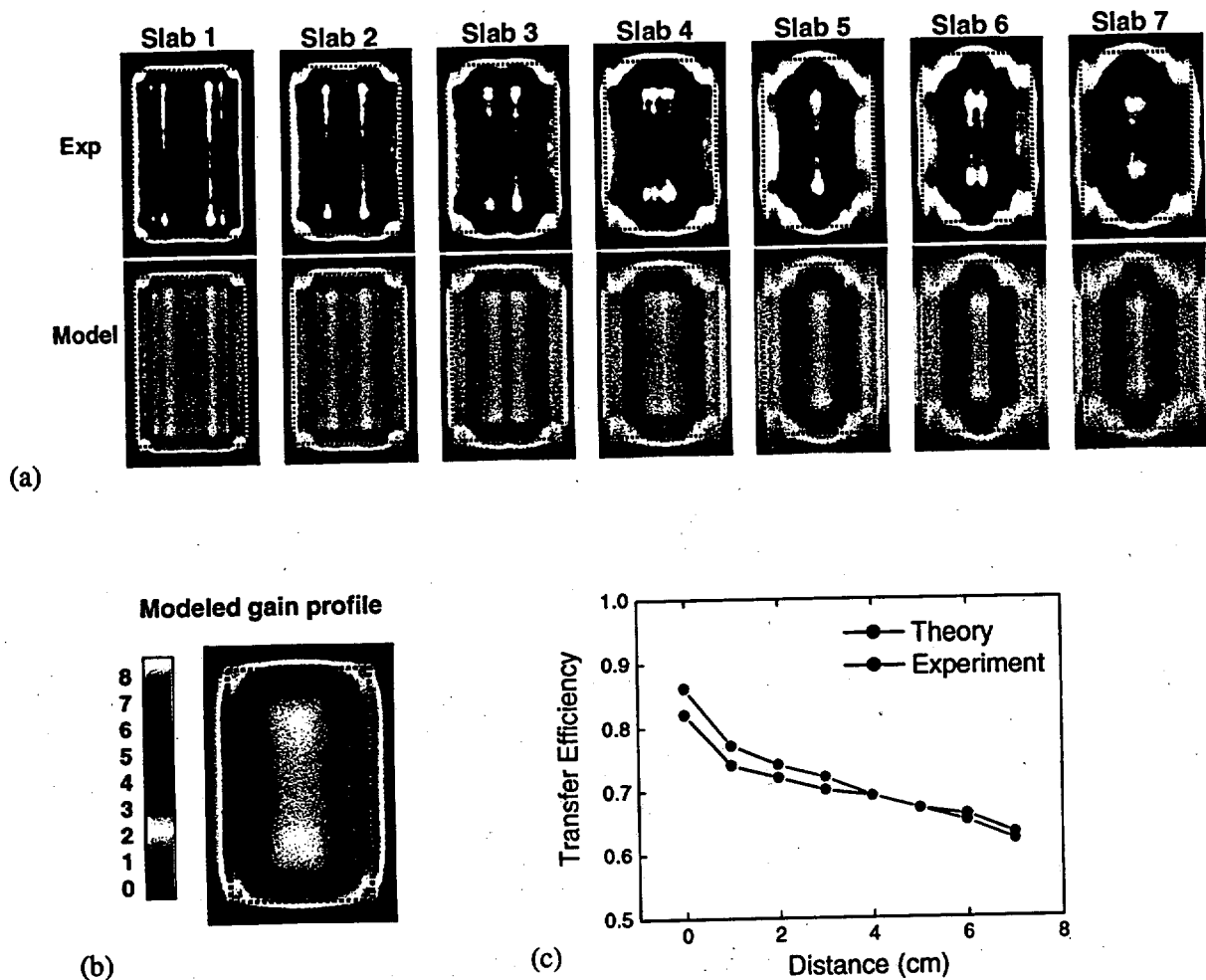


Fig. 2.1.3.3 (a) Measured intensity plots show good agreement with OPTICAD models for free space propagation out of the diode pump delivery system at equivalent amplifier slab locations. (b) Modeled gain profile for the entire amplifier head shows good spatial uniformity over the extractable  $3 \times 5 \text{ cm}^2$  area. (c) The transfer efficiency of diode light into the  $3 \times 5 \text{ cm}^2$  extractable energy also shows good agreement between OPTICAD models and experimental measurement.

#### System Alignment and 4-Pass Propagation

After the pump delivery system was characterized it was positioned in the main beamline and aligned with respect to the amplifier. To accomplish this, a reference beam was injected through the back mirror along the optical axis to the output (Fig. 2.1.3.4). This forms a straight reference line through the system in order to position the pump delivery system, amplifier head and relay telescopes. A precision wedge was then placed at back mirror, which deviated the beam with the proper angle for angular multiplexing. Pinholes were inserted and aligned. Next, the reverser mirrors, which control the injection of the front end and pick off the beam for the reverser, were inserted and aligned. The reverser mirror alignment is critical and difficult since the multiplexing angle must be rotated by 90 degrees within the reverser leg without changing the multiplexing angle or rotating the beam. Figs. 2.1.3.5a-c show the beam profiles in different locations after the system was fully aligned. Fig 2.1.3.5 is a picture of the beam after



the serrated aperture (pass 0). The aperture is made of a chrome mask deposited on glass. The aperture is used to reshape the Gaussian beam coming out of the front end laser into a Super-Gaussian spatial profile. This shape reduces diffraction losses and improves the extraction efficiency of the laser beam as it passes through the amplifier. The beam profile after pass 1 (see Fig. 2.1.3.4) is shown in Fig. 2.1.3.5b and at the output of the entire 4-pass system is shown in Fig. 2.1.3.5c. The modulation observed at the output is mostly due to diffraction effects and imperfect alignment through the system. We have identified methods improving the profile and will implement them in the upcoming months.

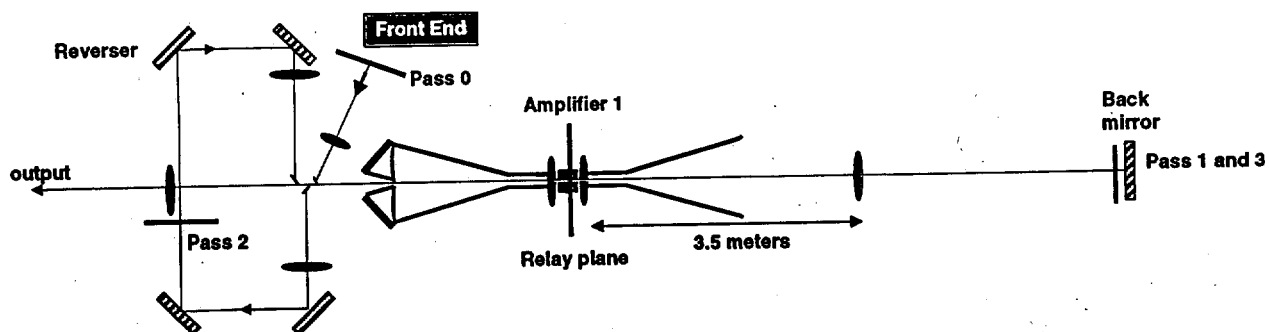


Fig. 2.1.3.4 Schematic diagram of the current half-Mercury system.

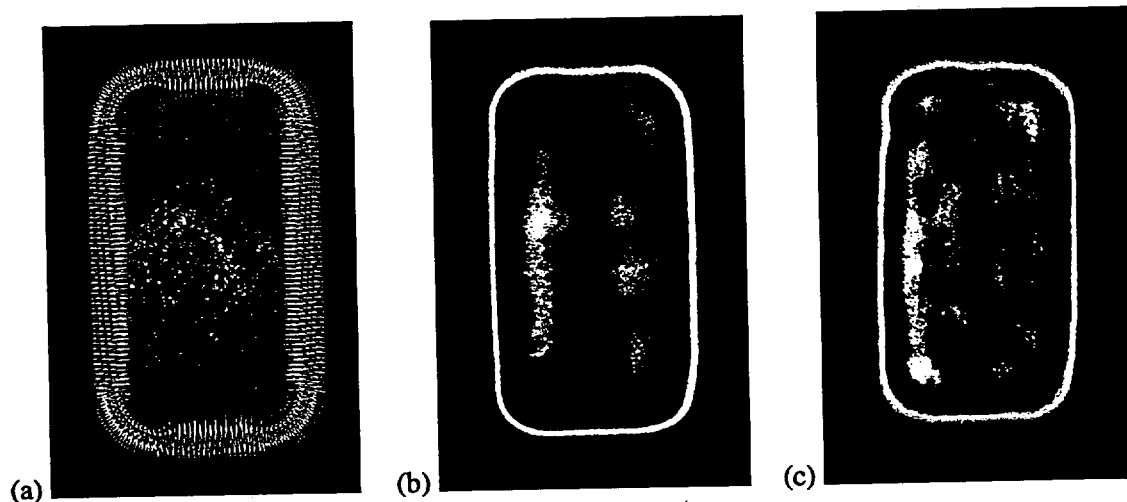


Fig. 2.1.3.5 (a) Measured spatial intensity profile after the serrated aperture showing flat spatial profile and serrates used for apodizing to a supergaussian, (b) Measured spatial intensity after first pass showing the spatially-filtered, apodized beam. (c) Output intensity profile after four passes through the system.

#### ***Gain Measurements with Surrogate Nd:Glass Amplifiers***

The small signal gain was measured with seven Nd:glass slabs mounted in the He gas cooled amplifier head. The glass slabs serve as surrogate gain media until the crystal slabs are ready and allow us to test many aspects of the pump delivery and gas cooled amplifier hardware. The phosphate LHG-8 slabs have a small amount of absorption at 900 nm within the wings of the absorption spectra ( $\sim 10^{-21} \text{ cm}^2$ ). This allows us to perform gain measurements with the same set of diodes that have been optimized for Yb:S-FAP. The slabs were pumped with the two fully populated diode backplanes each holding 36 diode tiles

and operating at a total peak power of 125 kW of diode light in a 750  $\mu$ s pulselength. The diode array was cooled to  $-23.5^\circ\text{C}$  in order to shift the output wavelength to 887.9 nm, which is close to the 880 nm absorption peak in LHG-8 glass. Only 2% of the pump light incident on the amplifier head was not absorbed and leaked out the end of the amplifier. The current state of the half-Mercury system, which was used for small signal gain measurements, is shown in Fig. 2.1.3.4. A 4-pass probe beam with the intensity low enough such that no gain saturation occurs will experience an absolute exponential gain given by:

$$I(t) = I_0 \exp \{ 4 N(t) \sigma L \} \quad (1)$$

where  $I_0$  is the incident probe intensity (well below the medium's saturation intensity),  $N(t)$  is the upper laser level population,  $\sigma$  is the stimulated emission cross-section and  $L$  the gain length. The small signal gain was evaluated by three different methods. The experimental results are shown in Figs. 2.1.3.6a-c. A longpass filter was utilized to eliminate pump light from propagating in the cameras and detectors. The continuous wave (CW) gain experiment was performed by focusing the signals onto the photodiode located in the diagnostic package that was connected to a digitizing oscilloscope. The voltage signal recorded is directly proportional to the gain. As can be seen in Fig. 2.1.3.6a, the gain signal increases during the 750  $\mu$ sec diode pulse length as the population inversion builds and reaches a peak value of 2.26 at the end of the pump pulse. The signal then decays back to its original DC level. During the measurements, a small amount of fluorescence leaked into the photodiode. This background signal was accounted for by measuring the signal level on the oscilloscope with the diode light on and probe laser off. The 4-pass gain can be calculated using:

$$G = \frac{V_{PL} - V_P}{V_L - V_B} \quad (2)$$

where  $V_{PL}$  is the signal with diode pump and laser probe,  $V_P$  is the signal with just diode pump,  $V_L$  is the DC level with the laser probe, and  $V_B$  is the DC level with no light. The pulsed gain experiments utilize a pulsed probe laser with a pulselength of 12.2 ns. The timing of this probe pulse was adjusted to match the peak in the fluorescence signal that corresponds to the peak gain. Using the same photodiode and oscilloscope, pulsed gain measurements resulted in a measured gain of 2.28 as shown in Fig. 2.1.3.6b. Since the fluorescence signal is not detectable on the nanosecond time scale, the gain is simply the signal with diode pump and laser probe divided by the signal with just the probe laser. The third method used to measure the gain was by spatially resolving the gain with a camera. The result shown in Fig. 2.1.3.6c was obtained by once again using equation 2 for each pixel "i" in the image:

$$G(i) = \frac{V_{PL}(i) - V_P(i)}{V_L(i) - V_B(i)} \quad (3)$$

The average gain in the  $3 \times 5 \text{ cm}^2$  for the extractable area is 2.36 with a spatial peak gain of 3.12. Again, much of the structure observed on the spatial gain profile in Fig. 2.1.3.6c is due to diffraction and clipping losses due to pinholes and imperfect alignment through the system. These preliminary effects will be minimized as we continue to operate the system and optimize its performance. The gain measurements are in good agreement with one another, and are in rough agreement with the current 1-D model that predicts a gain of 2.8. Much of the difference is attributed to differences in the coating transmissions for the diodes at 887 nm.

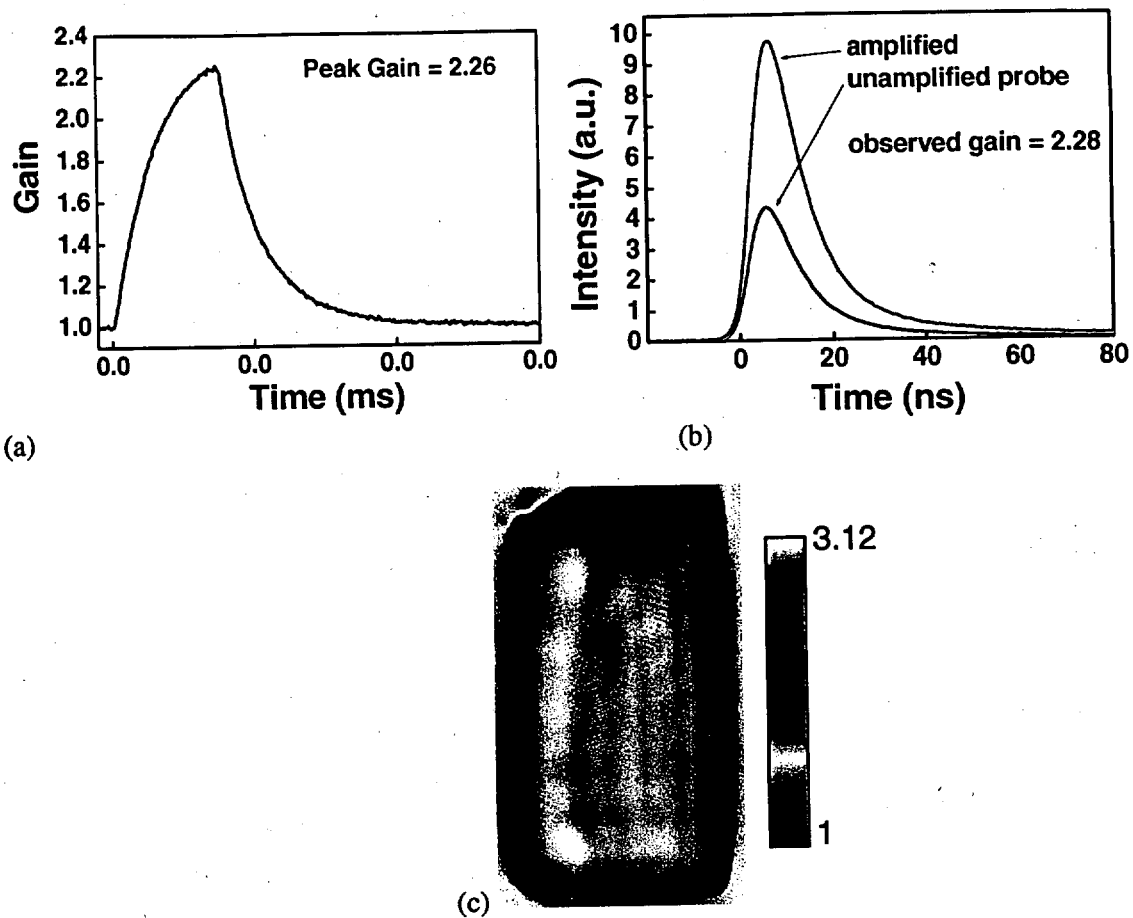


Fig. 2.1.3.6 (a) CW small signal gain with a peak value of 2.26 before the excited state decays back to the ground state. (b) Pulsed gain measurements taken at the peak of the gain curve produces a gain of 2.28. (c) Spatial gain profile taken with a pulsed laser has a peak gain of 3.12 and an average gain of 2.36.

## 2.1.4 Laser System Modeling

Current efforts in laser system modeling are directed towards developing an integrated model that can be used to predict the performance of Mercury and future design efforts. Several independent codes are used to model different aspects of the laser system, such as the energetics, thermal distortions, and optical aberrations. Our main focus this year was aimed at learning how to implement a newly developed two-dimensional propagation code called MIRO. MIRO employs a graphical user interface to run a diffraction code and was developed by the scientists at CEA in France. MIRO uses a Fourier technique to solve the nonlinear Schrödinger equation, to obtain a representation of the single-polarization complex electric field  $E(x,y,z,t)$  in two transverse directions  $(x,y)$  and time as the beam transports through a chain of optical elements. The user-friendly graphical user interface allows visual layout and verification of optical components in the system. To accurately model laser propagation through amplifiers and real optics, several input files and parameters are required including: the spatial gain profile, thermally driven phase distortions, static phase distortions for optics and amplifiers, in addition to spectroscopic, optical, and mechanical properties of system components. Fig. 2.1.4.1 is a flow chart illustrating codes and other inputs required to properly model propagation through the system.

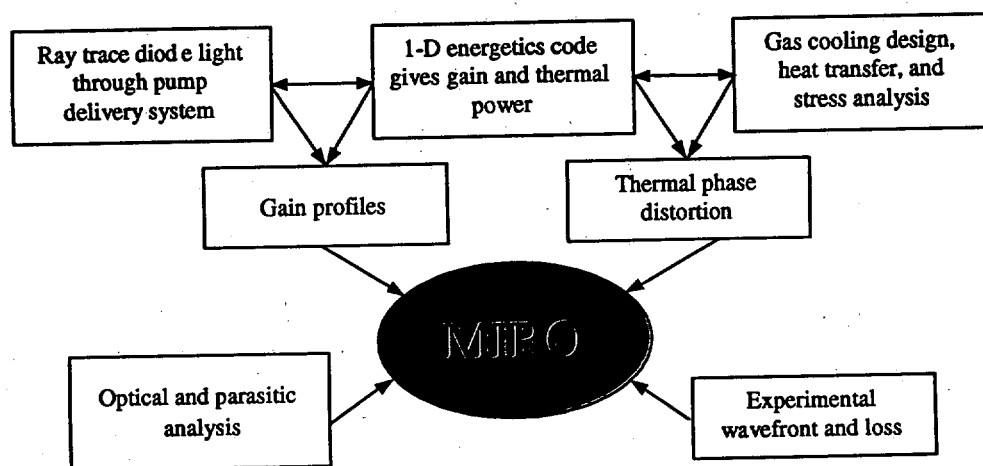


Fig. 2.1.4.1 Flow chart of modeling efforts and the individual codes provide input into the MIRO diffraction code.

An example of the user interface is shown in Fig. 2.1.4.2. A system is defined in the central window by choosing the optical components (shown on the left), placing them in the desired location in the window, and keying in all geometrical, optical, and phase information. The boxes or optical components are connected by "lines" or propagators which indicate the priority of which component is passed through first. Using the run-time parameters at the top of the screen, users can control the calculation mode and resolution of the calculation. Components highlighted in yellow can be opened to display output parameters such as temporal intensity plots, 2-D spatial intensity and phase plots of the beam at selected locations. Users can also bring up histogram plots of energy, B-integral, and many other scalar results for the full system. The Mercury laser system model yields the typical data in Fig. 2.1.4.3. The output spatial intensity profile is shown in Fig. 2.1.4.3a, while scalar histogram plots of energy and B-integral are shown in Figs. 2.1.4.3b and 2.1.4.3c respectively. With current doping levels in the Yb:S-FAP crystals, the MIRO code predicts approximately 83 J output with a B-integral of 0.7 radians for 10 ns. The MIRO model currently predicts that approximately 96% of the energy can be focused to a 5X diffraction limited spot and 81% in a 1X diffraction limited spot. The model will be upgraded next year to include full aperture phase maps of the S-FAP crystals. Current inputs use phase maps extrapolated from

smaller samples. In addition, thermal phase distortions will also be included. Preliminary modeling indicates that about 1 wave of power for each pass through an amplifier head. We plan to use a combination of static phase plates and a deformable mirror to remove the low order thermal wavefront distortions.

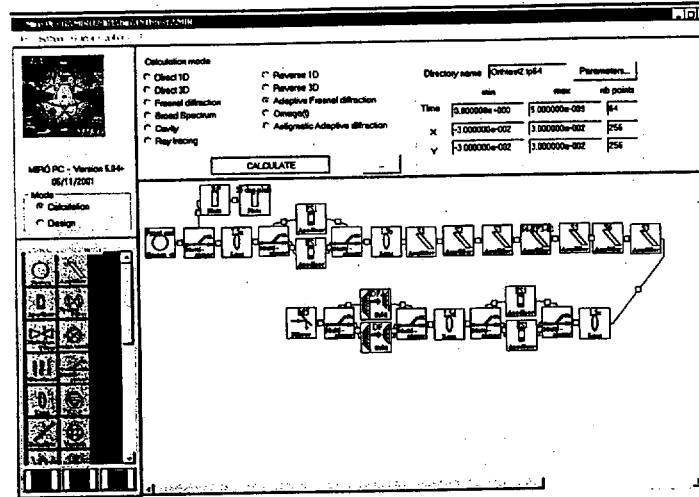


Fig. 2.1.4.2 Graphical user interface of the MIRO program showing user defined optical elements, layout, and run-time settings.

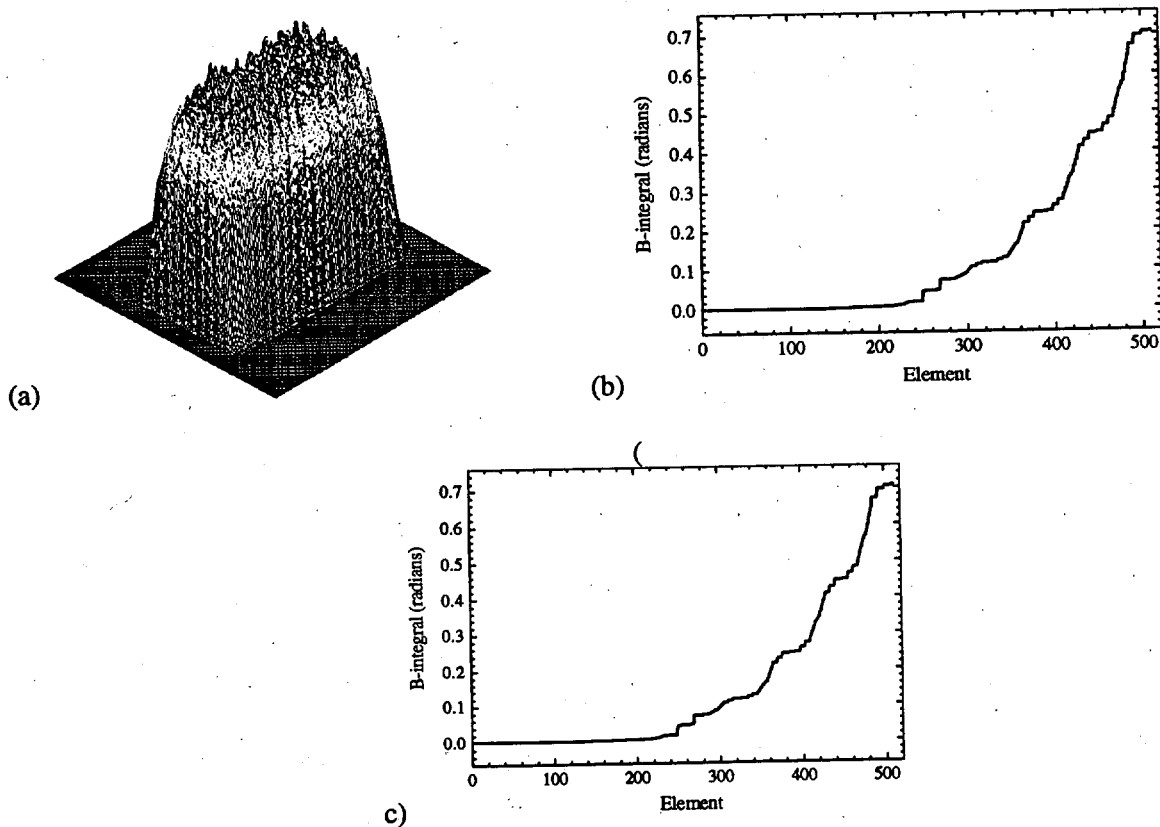


Fig. 2.1.4.3 Typical output from a calculation of the full Mercury system showing: (a) Output near-field 2-D intensity profile, (b) Energy as a function of optical elements encountered in the system, and (c) B-integral as a function of optical elements in the system.

## 2.1.5 Laser Diagnostics

The angularly multiplexed, four-pass architecture of Mercury allows the laser beam to be easily diagnosed on every pass without the use of fast optical switches. A total of five packages will be used on the system to monitor energy and beam quality during the 10 Hz operation. The data gathered from the diagnostics will allow us to track energy growth, beam quality and the onset of damage. The tracking of damage on a shot-to-shot basis is important for rep-rated systems where damage sites can grow quite rapidly and cause optics to fail. A single package is shown below in Fig. 2.1.5.1. We built and activated three packages. They were side mounted on the optical table in order to create a smaller footprint as illustrated in Fig. 2.1.5.2.

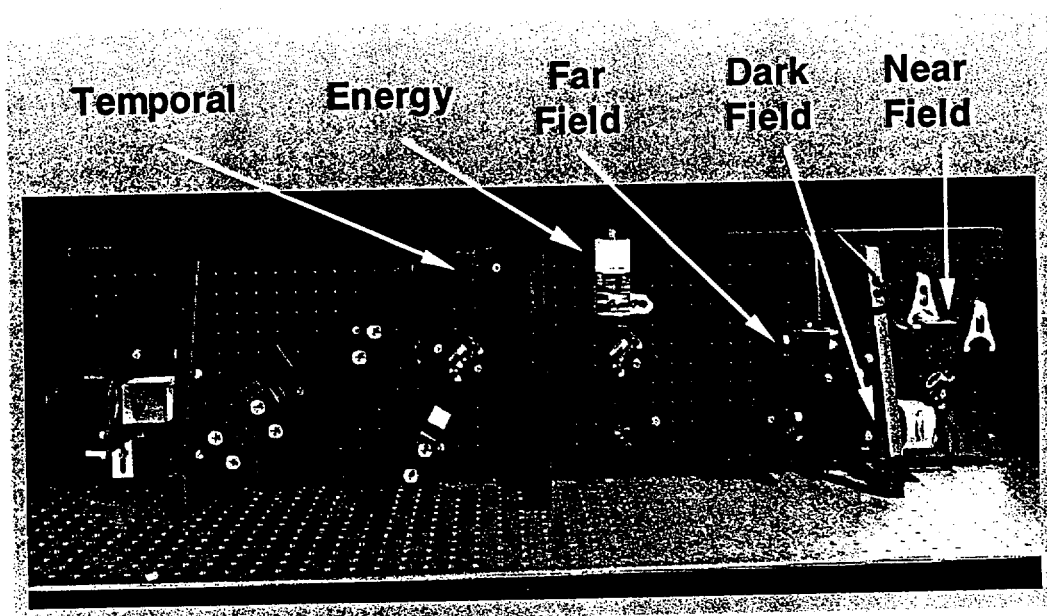


Fig. 2.1.5.1 Single diagnostics package.



Fig. 2.1.5.2 Three packages have been activated. Eventually, five packages will be needed to characterize the beam on every pass through the system.

Each package has a set of diagnostics to simultaneously measure temporal waveform, total energy, and beam intensity in the nearfield (before focusing lens), farfield (after focusing lens), and darkfield. The darkfield image is an important diagnostic for flagging the onset of damage and sending a rapid message to the PLC (see Section 2.10) to block the diodes from firing. An illustration of how a darkfield image differs from near- and farfield images can be seen in Figs. 2.1.5.3-2.1.5.5. When a damaged optic is placed in the beam path, both the near and far field images fail to sharply define the presence of damage. However, if a beam block (cross hair) is properly aligned at the focus of a relay telescope, then the unscattered light is blocked, and the high angle light emanating from the damage site passes around the block and images the damage site onto the camera. We tested the resolution of our system and have determined that damage sites on the order of 50  $\mu\text{m}$  can be resolved. We have developed a software algorithm to integrate the darkfield image file, compare it to a threshold value and determine if the number of illuminated pixels has increased from the previous shot. If there is a difference, then the PLC is notified and the diodes are shut down. The logic sequence is shown in Fig. 2.1.5.6. We are in the process of testing and integrating our software routine into the overall control system.

#### optic with damage

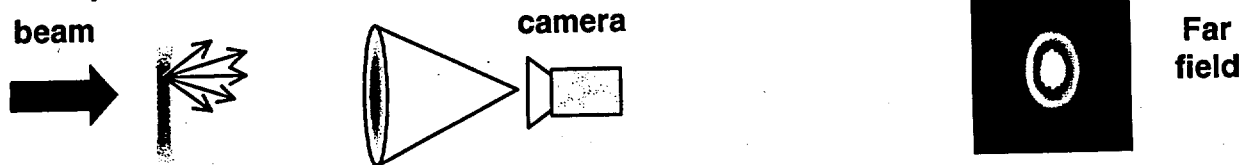


Fig. 2.1.5.3 A farfield image is captured at the focal point of a lens.

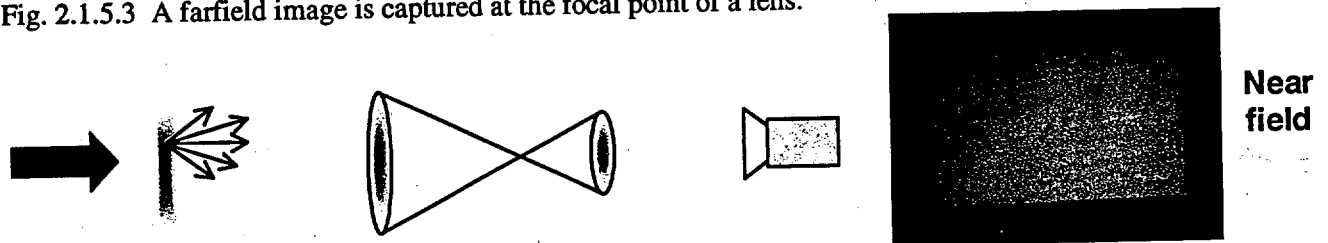


Fig. 2.1.5.4 A nearfield image allow us to view the beam quality at within the amplifier.

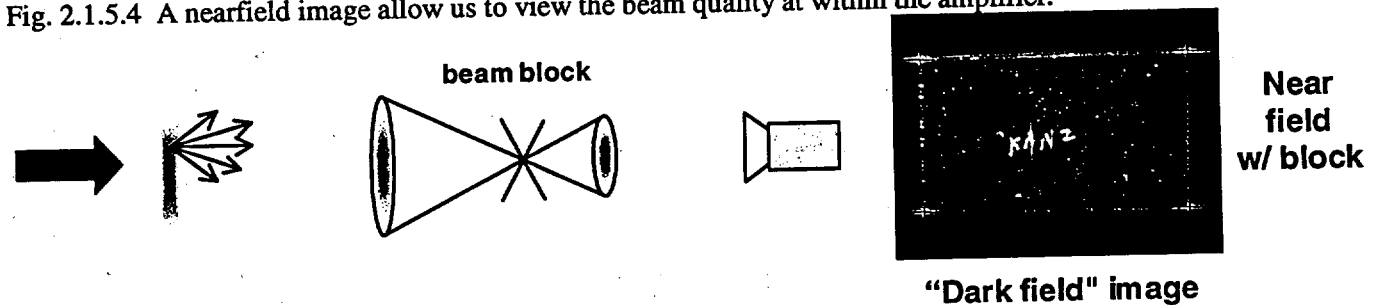


Fig. 2.1.5.5 The darkfield image allow the a high contrast picture of the damage site to be formed.

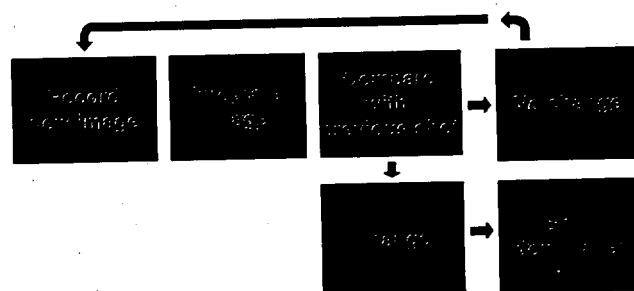


Fig. 2.1.5.6 Algorithm for detecting damage.

## 2.1.6 Pockels Cell Development

### *Electro-optic isolation switch*

An electro-optic switch or Pockels cell is an electronically controlled device, consisting of a nonlinear optical crystal (such as  $\text{KD}_2\text{PO}_4$  (KD\*P),  $\text{KTiOPO}_4$ , or  $\text{LiNbO}_3$ ) and fast power supply, that can control the polarization state of light passing through the switch. As seen in Fig. 2.1.6.1, the Pockels cell (named after its discoverer in 1895) in combination with a polarizer can control the direction of light propagation on the nanosecond time scale. A characteristic voltage, called the half-wave voltage, is used to induce a change in the refractive index of the crystal, thereby changing the speed of light propagation in the crystal.

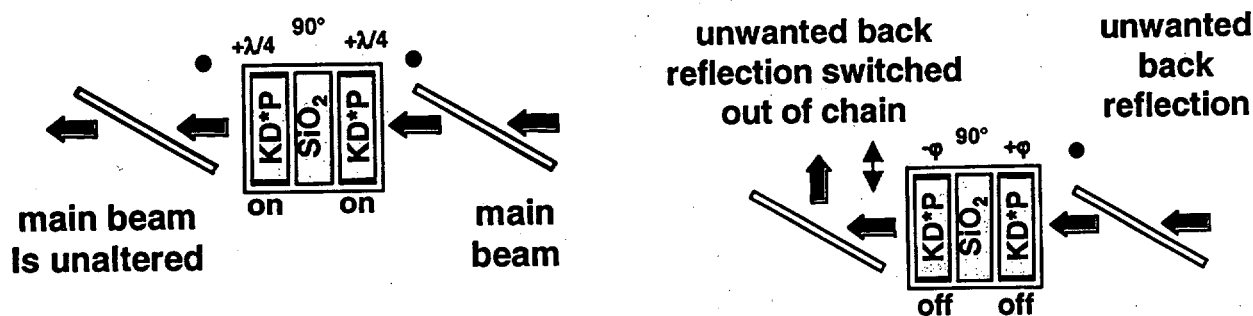


Fig. 2.1.6.1 In the top picture, voltage is applied to both crystals such that the polarization of the incident light is rotated 90 degrees. This voltage is called the half-wave voltage. As the voltage is removed (see lower figure) the incident light polarization is rotated only by the passive optic (90 degree rotator). Thus, the combination of the crystals and polarizers allow control of the direction of light propagation.

For the Mercury Laser application  $\text{KD}_2\text{PO}_4$  (DKDP) is the only electro-optic crystal available in large apertures with high optical homogeneity and with damage thresholds exceeding  $10 \text{ J/cm}^2$ . However, the relatively low thermal conductivity, high near-infrared optical absorption, and low fracture strength makes DKDP difficult to use for high average power applications.<sup>1</sup> A moderate aperture ( $3 \times 5 \text{ cm}^2$ ) electro-optic cell which can handle 100 W of average power is required for use as an isolation device. We have built and tested a scaleable, half-aperture, dual DKDP crystal Pockels cell, which, in off-line testing, exhibits less than 0.5% depolarization when thermally loaded with a 100 W near-infrared laser.

Fig. 2.1.6.2 shows the arrangement of a pair of DKDP crystals in a thermally compensated Q-switch. The DKDP ( $1.5 \times 2.5 \text{ cm}^2$  aperture) crystals and a 90 degree quartz rotator are thermally bonded to an alumina substrate, which provides a sink for the modest amount of heat ( $\sim 2 \text{ W}$ ) deposited in the crystal. The DKDP crystals we utilized were polished to a flatness of  $\lambda/15$  with parallelism better than  $5''$ , as measured on a Zygo interferometer at 632.8 nm. In an ideal pair of identical length crystals, the static birefringence, thermally induced birefringence, and the stress-optic induced depolarization would vanish. When the ideal crystal arrangement of Fig. 2.1.6.1 is placed between parallel polarizers (with



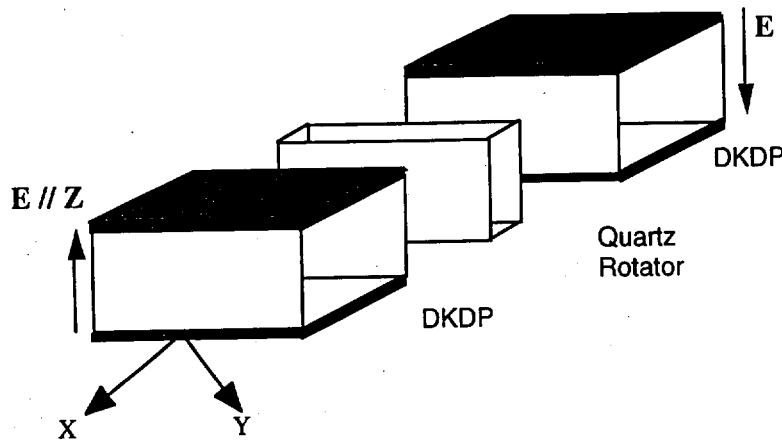


Fig 2.1.6.2 Transverse, bicrystal, thermally compensated switch consisting of DKDP crystals and 90 degree quartz rotator.

polarization axis at  $45^\circ$  to the Z axis) no light would be transmitted across the aperture. If a  $90^\circ$  rotator is placed between the compensated crystal pair, the maximum intensity is transmitted. For a *non-ideal* crystal pair, the fraction of light that is depolarized due to uncompensated birefringence is determined from the expression:

$$I_{\text{depolarization}} = I_{\text{not compensated}} / (I_{\text{not compensated}} + I_{\text{compensated}})$$

Our test setup, shown in Fig. 2.1.6.3, utilizes a 633 nm source coincident with a multimode 100 W Nd:YAG laser. Depolarization is examined utilizing both a camera as well as a photodiode. The depolarization as a function of thermal loading is shown in Fig. 2.1.6.4. At the maximum thermal loading, the compensated crystal pair exhibits less than 1% depolarization at 633 nm (less than 0.5% depolarization at  $1 \mu\text{m}$ ). It should be noted that the compensation of the welding laser represents the extreme of power density that will be encountered, where essentially all heat is deposited into one small area. The Mercury laser will have a uniform beam extending over the full aperture of the crystal at an average power of 100 W, as opposed to a concentrated hot spot. The use of ceramic apertures for the entrance and exit surfaces will help prevent stray radiation from illuminating the crystals in a non-uniform manner. Thus we expect the thermally induced depolarization measured above to be an upper bound.

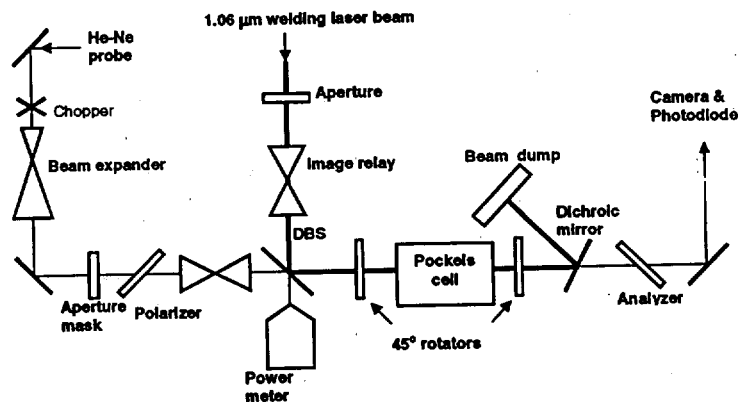


Fig. 2.1.6.3 Apparatus used to thermally load Pockels cell assembly and examine depolarization.

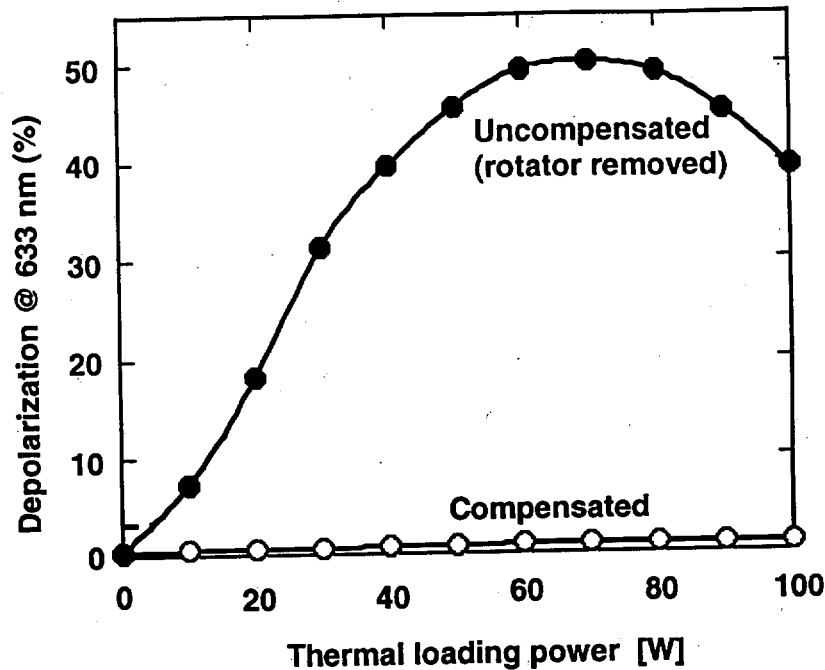


Fig. 2.1.6.4 633 nm depolarization of the uncompensated dual crystal device (90 degree rotator removed) and thermally compensated device as a function of thermal loading.

### Optical Switching

The switching characteristics of the Pockels cell are driven by the switch aperture, the desired rise-time, the capacitance of the switch, and the peak current capability of the switching device. The switching conditions for Mercury do not place too high of a demand on the power supply: A rise-time of the switch (20-80% of the drive voltage) of 10 ns, followed by a 10 ns hold time, and finally a 10 ns fall time. The aperture of the switch is 4 cm x 6 cm x 2 cm (x2 crystals). The switching voltage can be determined from the following relation:

$$V_{\pi} = (d / \ell) \lambda / r_{\text{eff}} \quad (1)$$

$V_{\pi}$  is the switching voltage for a polarization rotation of 90 degrees,  $d$  is the electrode spacing and  $\ell$  is the propagation thickness. For highly deuterated DKDP with  $r_{\text{eff}}$  is 74 pm/V,  $\lambda = 1047$  nm,  $\ell = 2\text{cm}$  (\*2 crystals) and  $d = 4\text{cm}$ , the switching voltage is 14.1 kV. The capacitance of a transverse electrode switch is given by the following:

$$C = \epsilon \epsilon_0 A / d = 8.85 \text{ pf} * \epsilon (A/d) \quad (2)$$

Again, for KD\*P  $\epsilon \sim 40$ , the plate area  $A = 0.06 \text{ m} \times 0.02 \text{ m} * 2$  and  $d$  is 0.04 m. The expected capacitance of the full size Mercury switch is nearly 22 pf. Finally, we can calculate the peak current, an important parameter with respect to the voltage pulser.

$$I = C dV/dT \quad (3)$$

With a switching voltage of 14.1 kV in 10 ns and a capacitance of 22 pf we expect a rather moderate peak current of 31 Amps. This type of current should be easily handled by a variety of switching technologies. The Pockels cell test assembly is shown in Fig. 2.1.6.5. We have demonstrated optical switching at 633 nm and are currently in process of testing the higher voltage (13.5 kV) electro-optic pulser required for switching at 1.047  $\mu\text{m}$ .

In conclusion, the Mercury laser requires a Pockels cell to prevent oscillation of unwanted beams during extraction of the desired energy out of the amplifiers. The Pockels cell is required to handle an average power of 100 W. In particular, the electro-optic switch is required to maintain a low

depolarization less than  $\sim 1\%$ . Finally, the device must switch with a voltage that is within the range of the voltage capability, capacitive load capability, and peak current capability of a voltage driver. We have tested a half-aperture Pockels cell that can be readily scaled to the device required for Mercury. In particular, this device has demonstrated both the static birefringence as well as the thermally loaded birefringence requirements. We have switched this device and have developed a voltage pulser for this system. We have a design for the full-aperture switch and are in process of ordering the full aperture crystals, and will implement this switch during the new fiscal year.

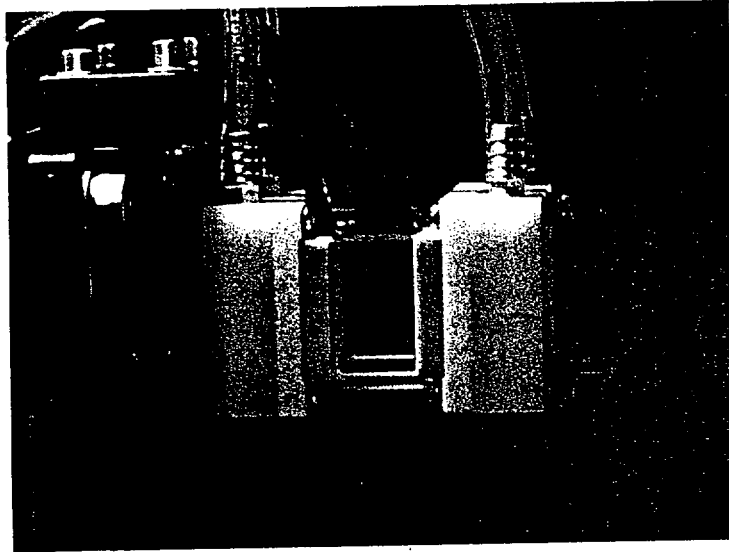


Fig. 2.1.6.5. A picture of the completed Pockels Cell Assembly.

- [1] D. Eimerl, "Thermal aspects of high-average-power electro-optic switches", IEEE J. Quantum Electronics 23 pp. 2238-2251 (1987).

## 2.1.7 Czochralski Crystal Growth

### *Growth Methodology*

The goals of the crystal growth effort are to produce high quality Yb:S-FAP [ $\text{Yb}^{3+}:\text{Sr}_5(\text{PO}_4)_3\text{F}$ ] crystals; this involves developing an outside company resource for the growth of full size crystals and assessing the feasibility of bonding two smaller crystals together to produce full aperture crystals with no compromise to the optical quality. The Mercury design requires 14 crystalline slabs of dimension  $4 \times 6 \times 0.75 \text{ cm}^3$ , Fig. 2.1.7.1, which will be potted into vanes and mounted into two amplifier heads; seven slabs will be required for each head. The growth of full aperture crystals has been a challenge due to a number of defects, including: cloudiness in as-grown boules, bubble core defects, grain boundaries, anomalous absorption, cracking, and inclusions around the outside of the boule. Currently, three Czochralski crystal growth stations are being utilized to accelerate the growth effort, chillers have been added to control cooling water temperatures to the power supplies thus regulating the heat load, and a motor generator is used to damp out fluctuations in the incoming power to the power supplies.

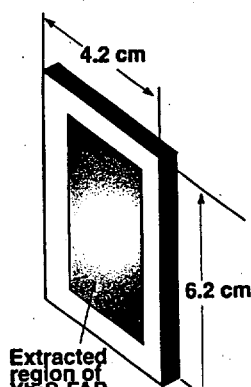
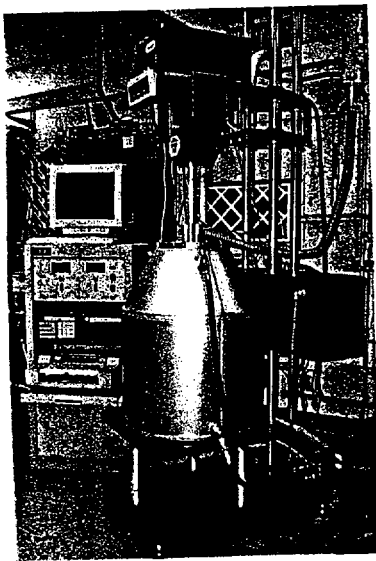


Fig. 2.1.7.1 Schematic of the slab dimensions (including edgecladding) required for the Mercury design.

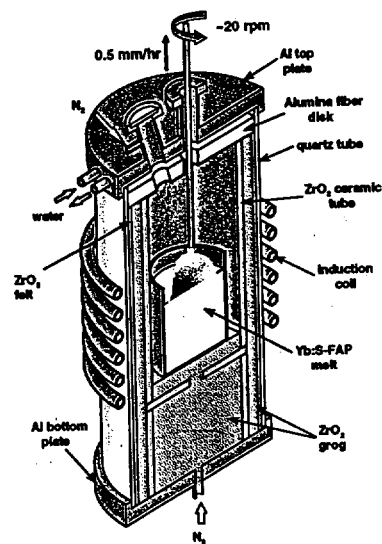
Significant progress has been made in understanding the growth characteristics and defect chemistry of Yb:S-FAP crystals. As part of this effort to understand the defect issues in Yb:S-FAP and find a feasible growth technique for producing high optical quality crystals, a collaborative research effort has been put forth within LLNL and among experts in the growth of high temperature crystals at commercial crystal growth companies: (1) Dr. Robert C. Morris (formerly of Allied Corp.), a world-renowned leader in solving defect problems in optical crystals, has been participating as a consultant in the growth of Yb:S-FAP, (2) Robert S. Feigelson of Stanford University has provided a great deal of technical insight and expertise, (3) Ralph Hutchinson at Scientific Materials (Bozeman, MT) has grown several crystals in a "high thermal gradient" furnace regime. We have continued our work with Northrop-Grumman Poly-Scientific (formerly Litton-Airtron/Synoptics Group) in an effort to develop a commercial source for Yb:S-FAP. One advantage of working with Northrop is that they have a proven facility in place for the growth of high quality crystals of the large dimension needed for Mercury and next generation lasers. In addition, we have engaged Crystal Systems, Inc. with a \$100K contract to explore the feasibility of growing Yb:S-FAP by the Heat Exchanger Method (HEM), which has proven successful for the growth of very large crystals such as sapphire, Ti:sapphire, silicon, and YAG. This effort is part of the advanced growth studies being done and will be discussed in the Advanced Growth section of this report.

### Growth Process

Crystals of Yb:S-FAP are grown by using the Czochralski method in three growth stations one of which is shown in Fig. 2.1.7.2a along with a schematic of the furnace design and basic growth parameters, Fig. 2.1.7.2b. The growth station consists of a Czochralski crystal puller, a 25 kWatt induction power supply, and a computer program that is used for automatic diameter control (ADC) of the crystal. Automatic diameter control is achieved by weighing the crystal as it is growing and calculating the mass gain per unit time (grams/hour or g/h), so that the diameter of the crystal is constant at a given pull rate. A 4" diameter by 4" tall Iridium crucible was chosen to contain the melt because it does not chemically react with Yb:S-FAP and has a high melting temperature. Zirconia is the main insulation component in the furnace as shown in Fig. 2.1.7.2b. The 4" diameter by 4" tall Iridium crucible and melt therein are heated by inductive coupling of the crucible to copper coil.



(a)



(b)

Fig. 2.1.7.2 (a) Picture of the Czochralski crystal growth station used for Yb:S-FAP growth. (b) Schematic of the furnace design with approximate growth parameters.

The time required for the current growth geometry of Yb:S-FAP crystals of suitable size to harvest slabs is approximately 17 days and encompasses a series of four steps that are critical to producing high quality material, Fig. 2.1.7.3. The first step requires that the seed be extended to grow out the grain boundaries from the crystal. The seed is extended at a diameter of approximately 5 mm to aid in growing the defects out toward the sides of the crystal where they will terminate. The cone section of the boule is the next critical step since the overall change in growth rates tend to be much higher than in other parts of the growth process and defects can form. For this reason the cone angle is kept very small or basically, the diameter of the boule is slowly increased to the full diameter. In the cylindrical section of the boule, it is essential that stable growth conditions be maintained to preserve the defect free nature of the crystal from which slabs will be cut. Finally, the crystal is necked in at the bottom and allowed to cool in the melt to decrease the thermal gradients through the boule during cooling and reduce cracking. A pull rate of 0.5 mm/hr is currently used since higher rates have shown an increase in the magnitude of the defects. The rotation rate is typically 15 rpm to provide a convex melt-interface shape that is stable and does not introduce unwanted fluctuations that can perturb the growth. This specific growth technique has significantly reduced the number of defects and yielded high quality material that meets the Mercury specifications.

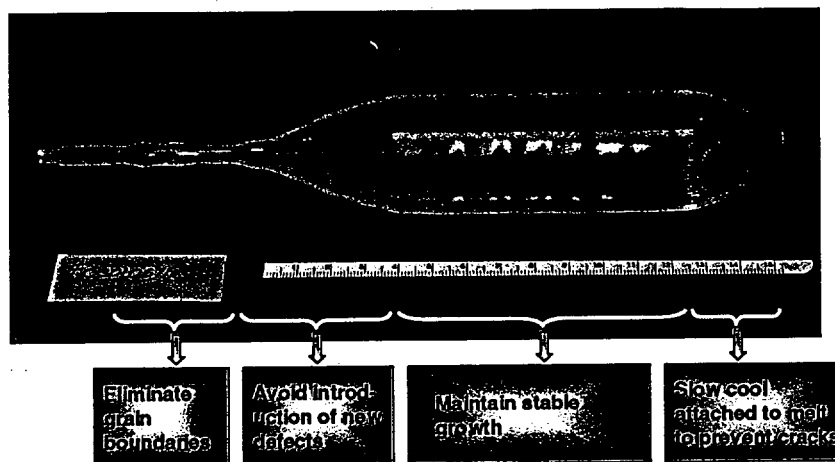


Fig. 2.1.7.3 Current technique for the growth of Yb:S-FAP crystals

### Growth Improvements

Over the last year, several improvements have been implemented to increase the ability to produce high optical quality Yb:S-FAP with reproducibility. A new growth station design was implemented where the furnace is completely encapsulated within a cooling shroud (Fig. 2.1.7.1) to add flexibility in changing the furnace to alter thermal gradients, which have proven critical in controlling the defects during the growth process. By implementing this new growth station design with higher thermal gradients, the bubble core has been successfully diminished and concentrated to the center of the boule so that the slabs can be cut around the core region.

In addition, we have been working with the National Institute of Standards and Technology (NIST) to complete a partial phase diagram for the Yb:S-FAP system, Fig. 2.1.7.4. The phase diagram documents the compositional and structural changes that take place relative to temperature, which helps to pinpoint the exact compositions that will produce the highest quality crystals without unwanted defects.

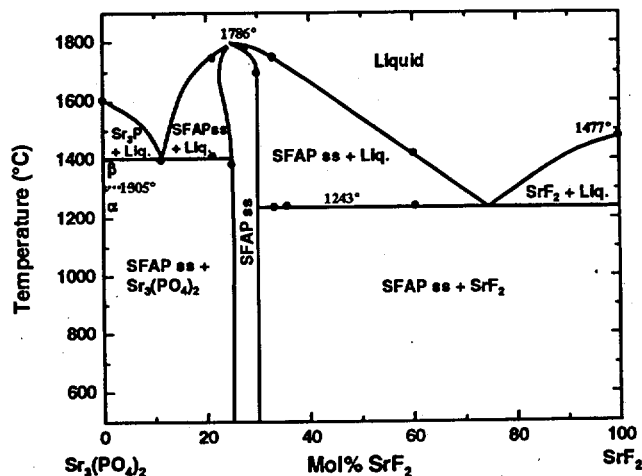


Fig. 2.1.7.4 Partial phase diagram for the S-FAP system.

### Defect Issues

Yb:S-FAP crystals can show a number of defect structures that occur in various forms. In particular, cloudiness, an anomalous absorption, bubble core defects, grain boundaries, cracking, and inclusions around the outside of the boule. Each of these defect structures has been studied in considerable detail and solutions to reduce and /or eliminate them have been implemented as outlined below in Table 2.1.7.1. Remaining concerns include a bubble core that needs to be further reduced and cracking during cooling and fabrication.

Table 2.1.7.1 Summary of defect issues and the solutions.

Issue	Fundamental Cause	Resolution	Growth Efforts	
			LLNL	Northrop
Cloudiness	Precipitation on line defects	<ul style="list-style-type: none"> <li>• excess <math>\text{SrF}_2</math> in melt</li> <li>• annealing over melt</li> </ul>	Under control	Under control
Anomalous absorption	$\text{Yb}^{3+}$ in a different site	<ul style="list-style-type: none"> <li>• c-axis along growth direction</li> <li>• thermal gradients of <math>&lt;70^\circ\text{C}/\text{cm}</math></li> </ul>	Under control	Under control
Grain boundaries	Dislocations from the seed	<ul style="list-style-type: none"> <li>• seed extensions to grow out boundaries</li> </ul>	Under control	Under control
Bubble Core	Constitutional supercooling	<ul style="list-style-type: none"> <li>• growth stability</li> <li>• maximize thermal gradients</li> </ul>	Under control	Under control
Cracking	Internal stresses	<ul style="list-style-type: none"> <li>• cool crystals attached to melt</li> <li>• anneal after growth</li> </ul>	Nearly resolved	Nearly resolved
Size	Control of defects	<ul style="list-style-type: none"> <li>• diffusion bond half-size slabs</li> </ul>	Under control	Under control
"Sparkle" inclusions	Limited Yb solubility in melt	<ul style="list-style-type: none"> <li>• Yb-doping of <math>&lt;0.75</math> At% in melt</li> </ul>	Under control	Under control

One method to reduce the magnitude of the bubble core or concentrate it to the center of the Yb:S-FAP crystal, is to stabilize the growth interface and decrease the amount of unwanted components in the growth boundary layer. This can be accomplished by increasing the thermal gradients in the furnace above and within the growth crucible. By doing this, temperature will effectively drive the convective melt stirring at the interface and reduce the thickness of the boundary layer of unwanted components that can cause unstable interface conditions. This approach has concentrated the bubble core more to the center of the boule, as described above, so that two half slabs can be cut from the outside of a crystal and bonded together as shown in Fig. 2.1.7.5. In addition, we have reduced the bubble core by growing approximate 3.5 cm diameter boules, where the smaller diameter allows for better interface control as well.

Cracking during fabrication has been a concern for us with recent crystals that have been grown at the higher thermal gradients. The gradients cause stress to form during the cool down process and this stress must be relieved prior to cutting the boules into slabs. We have been exploring post-growth annealing techniques in a separate isothermal furnace where the crystal is removed from the growth furnace, packed into crushed old remnant melt material from prior growths to maintain a "growth-type" atmosphere, and heated to an approximate temperature of 1400-1500 C for 6-24 hours to relieve stress.

The crystal is then cooled in an isothermal environment, which prevents any introduction of new stress into the crystal. These experiments are ongoing. In addition, we have found that annealing in this way helps to eliminate cloudiness in the crystals, see Fig. 2.1.7.6. It is likely that the second phase precipitate that has caused the cloudiness is re-dissolved into the lattice of the crystal. Therefore, post-growth annealing is a way to alleviate stress and prevent cracking during fabrication, as well as reducing the cloudiness in the crystals to make previously unusable material useful.

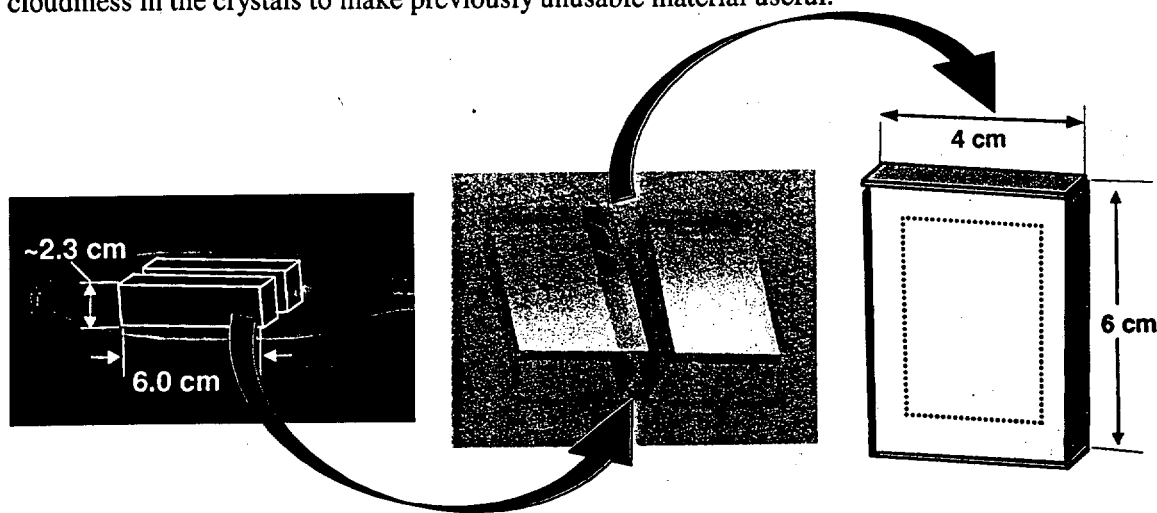


Fig. 2.1.7.5 Picture of the current growth geometry of a Yb:S-FAP boule and the orientation of slabs for diffusion bonding.

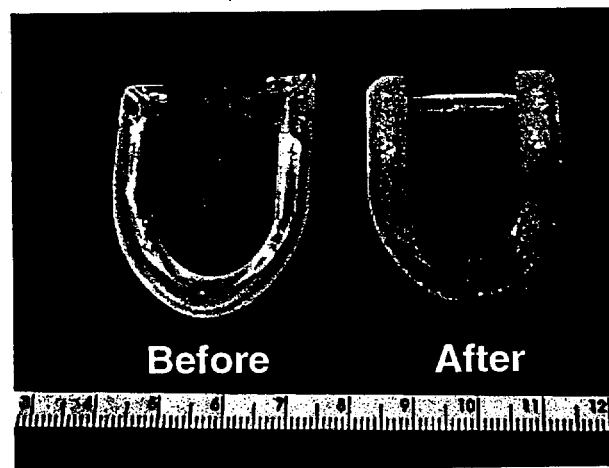


Fig. 2.1.7.6 Picture of a crystal with cloudiness, before and after annealing experiments.

By implementing the new growth furnace design and each of the resolutions to the defect issues (Table 2.1.7.1) we have been able to produce material for the fabrication of two bonded  $3 \times 5 \text{ cm}^2$  slabs and four full size  $4 \times 6 \text{ cm}^2$  slabs for the Mercury laser, see Fig. 2.1.7.7. There are a number of steps that must take place to fabricate a full size slab from the growth of the crystal to the final potting into the vanes. These steps are outlined in Fig. 2.1.7.8 along with the progress of each of the slabs.



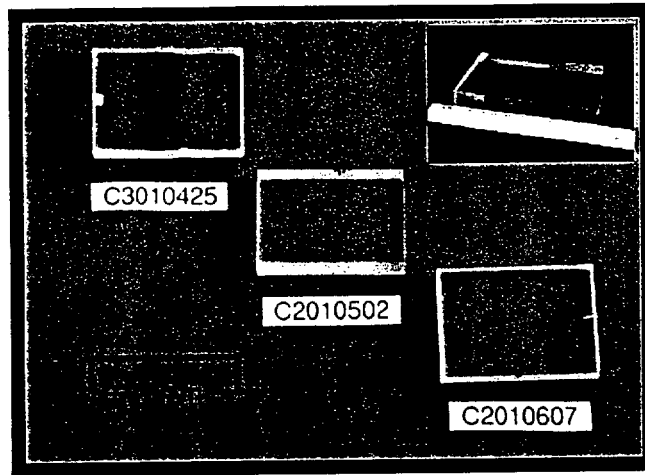


Fig. 2.1.7.7 Picture of the four bonded full size slabs.

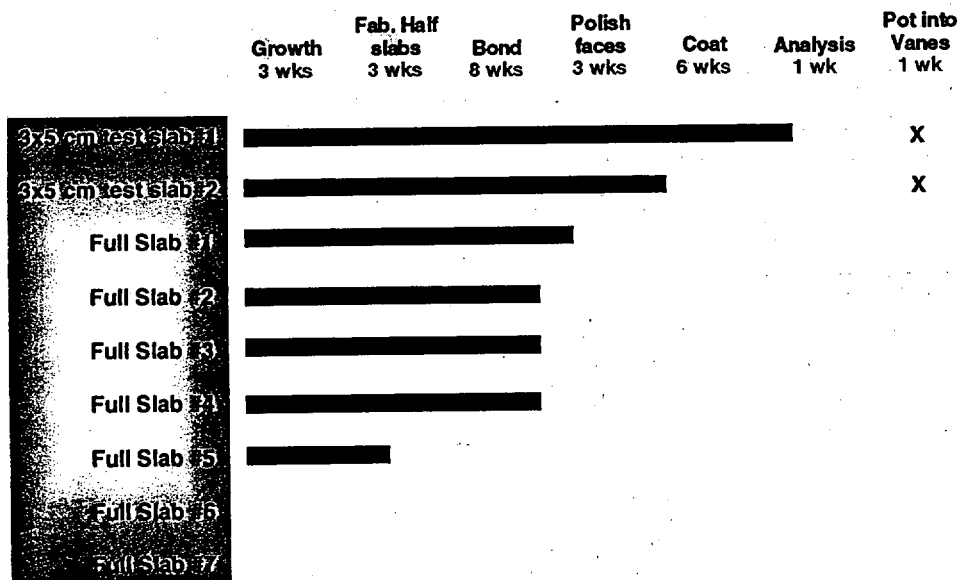


Fig. 2.1.7.8 Schematic of the steps required to fabricate the crystalline slabs for Mercury as well as the progress of each of the current slabs to date.

### Summary

In summary, significant progress has been made in understanding and controlling each of the defect structures in an effort to develop a reproducible growth process for high optical quality Yb:S-FAP crystals. To date, there are two 3x5 cm<sup>2</sup> slabs and five 4x6 cm<sup>2</sup> slabs in fabrication. Results have produced boules with greatly reduced defects which have optical properties that meet the Mercury specifications.

### Advanced Growth Efforts

In FY01, efforts have been made to explore advanced, larger size, Yb:S-FAP growth options for post-Mercury laser deployment. A two-fold approach was taken to look at conventional large diameter Czochralski crystal growth techniques as well as a less conventional technique called the Heat Exchanger Method (HEM).

The standard Czochralski growth yielded a crystal that was 5 cm in diameter and looked very promising; the polished cone section is shown in Fig. 2.1.7.9. There was an approximate 2 cm bubble core and cracking occurred in the full diameter section, however, these defects were expected for the furnace design that was used. The results of this growth are very encouraging for scaling the size of Yb:S-FAP crystals to the sizes necessary for future laser designs. Future experiments will require a modified furnace design and a larger crucible, which are commonly used for other large diameter, commercial oxide crystals.

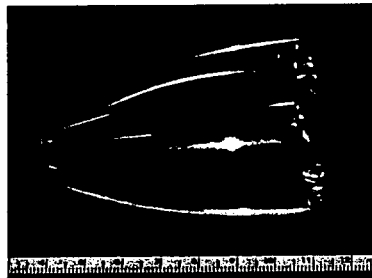


Fig. 2.1.7.9 Picture of the cone section of a 5 cm diameter Yb:S-FAP crystal grown at LLNL.

To explore alternate methods for growing Yb:S-FAP, we placed a contract with Crystal Systems, Inc. to do a feasibility study on growing crystals by the Heat Exchanger Method (HEM). In the HEM, crystals are grown from a seed of Yb:S-FAP placed at the bottom of a crucible under the melt. The growth is controlled by cooling the seed and slowly lowering the seed and furnace temperature to maintain a stable interface while the crystal is grown from the bottom of the crucible to the top. A picture of the furnace design is shown in Fig. 2.1.7.10. The HEM technique looks very promising for producing Yb:S-FAP crystals. Growths done during the contract produced approximate 2-3 cm square by 1 cm thick single crystals. The crystals were brownish in color, which has been attributed to color centers. However, recent annealing experiments done by holding the crystal over a molten Yb:S-FAP mixture for 2 days have shown that the brownish color disappears and clear crystals can be produced, see Fig. 2.1.7.11. In FY02, we plan to do a second feasibility contract with Crystal Systems to continue exploring the HEM technique as a viable pathway for scaling the size of Yb:S-FAP crystals to dimensions required for follow-on laser systems to the Mercury Laser.

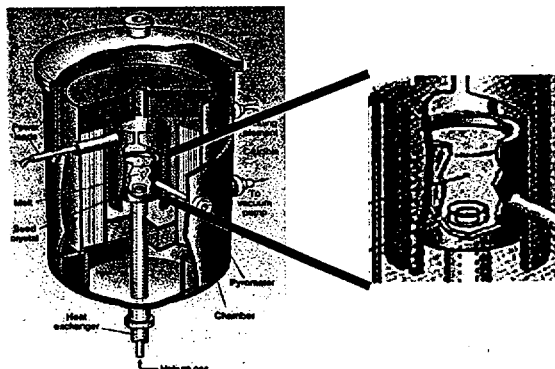


Fig. 2.1.7.10 Schematic of the furnace used in the Heat Exchanger Method at Crystal Systems.



Fig. 2.1.7.11 Picture of a Yb:S-FAP crystal grown by the Heat Exchanger Method, before (brownish color) and after (clear) annealing.

## 2.1.8 Laser Diodes

### 900 nm Diode Bars

The laser diode bars needed for the Mercury laser present several unique challenges. Both the high-peak power and long-pulse operation impose extreme thermal/optical stresses to the output and reliability of the diode bar. In addition, because of the narrow absorption band of Yb:S-FAP crystal, the material growth uniformity as well as the wavelength chirp during the pulse must be kept to a minimum compared to what is usually required in diode pumped solid state laser systems. Finally, it is worth noting that before the beginning of this project, no 900 nm diodes, of any kind, were commercially available. So in addition to the performance/reliability requirements that are unique to Mercury, it was imperative to sort out issues specifically related to growing high quality 900 nm diode material. In particular, we were concerned because the 900 nm wavelength appeared to fall between the AlGaAs and InGaAs semiconductor material systems. We have since established a productive business relationship with Coherent Inc and have received to date over 5000 diode bars that meet the stringent Mercury specifications. These bars are now commercially available, signifying the successful transition between R&D and production. Outlined below in the table are the specific requirements for the diode bars and the achieved performance:

Table 2.1.8.1 Diode Requirements and Status

Requirement	Status
10 nm FWHM at 750 us pulse	<5nm FWHM demonstrated
100 W peak output power per bar	Bars burned in at 115 W per bar
10% droop over pulse	5% droop demonstrated On 1 msec pulse
50% wall plug efficient	44% wall plug efficiency demonstrated
10:1 polarization (TE)	>10:1 TE to TM polarization discrimination
$10^8$ shot lifetime	$1.4 \times 10^8$ shots

With the exception of the 50% wall plug efficiency specification, all of the specifications shown above have been successfully demonstrated. Our demonstrated wall plug efficiency of 44%, while falling short of our goal of 50% is still a very good result for the large (640 kW) diode arrays that will be used to pump the Mercury laser.

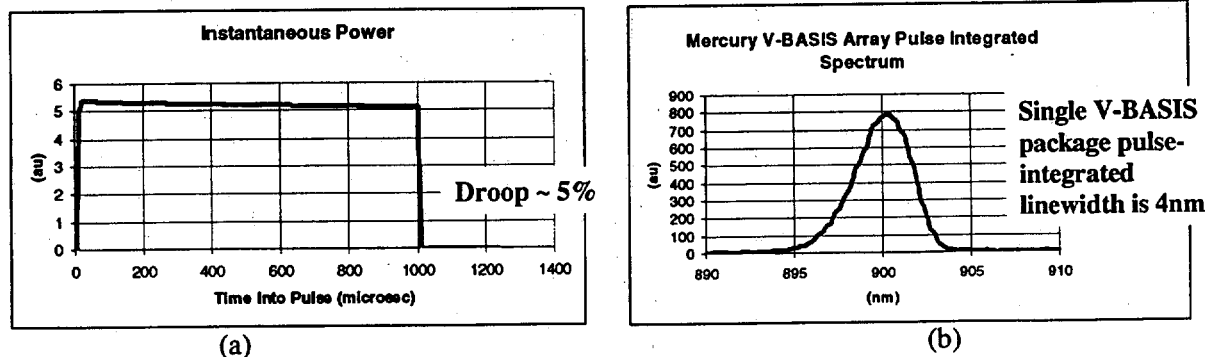


Fig. 2.1.8.1 (a) Instantaneous peak power vs. time into the pulse. Note that the power level has decreased by only ~ 5% at the end of the pulse (i.e., 1 msec). (b) Wavelength shift (i.e., chirp) during the pulse is approximately 4 nm.

Shown in Fig. 2.1.8.1 is the power droop and wavelength chirp of a typical 900 nm diode bar at the design point. The droop is ~5% over a 1 msec pump pulse, well beyond the 10% droop specification for a 750  $\mu$ sec pulse. Also shown is a pulse integrated spectrum with a FWHM of only 4 nm, which is also well beyond the 10 nm specification. Both the droop and wavelength chirp have been modeled previously showing good agreement with our measured performance. The fact that our diodes surpass both droop and chirp specifications is a result of the excellent thermal performance of both the diode bars and the diode package. The diode material used here is "AAA" material: Al-free in the active region, but with Al contained in the cladding layers. The idea is to remove Al from the active layer where it would degrade reliability (e.g., facet damage and bulk defects), while preserving Al-containing compounds in the cladding to maintain good carrier confinement (i.e., higher band gap). The cladding layer allows the use of higher band gap confinement layers that mitigate carrier leakage to provide lower threshold current (18 A), better slope efficiency (> 1 W/A), and lower droop than is feasible with entirely Al-free structures. Higher efficiency mitigates the effects of positive thermal feedback during the pulse, which was earlier observed to be a serious problem impacting both the droop and wavelength broadening due to chirp during a pulse. Other improvements include the use of a long cavity length (1 mm) for better heat dissipation, consistent with the 750  $\mu$ sec to 1 msec pulse widths needed for Yb:S-FAP. In addition, good wall plug efficiency is obtained using the 1mm cavities, as shown in Fig. 2.1.8.2. Shorter cavities have resistive losses that are too high at the design point (100W/bar) while longer cavities (> 1mm) have excessive parasitic optical loss. Even at power levels as high as 150W/bar, the 1mm cavity gives nearly optimum performance in wall plug efficiency.

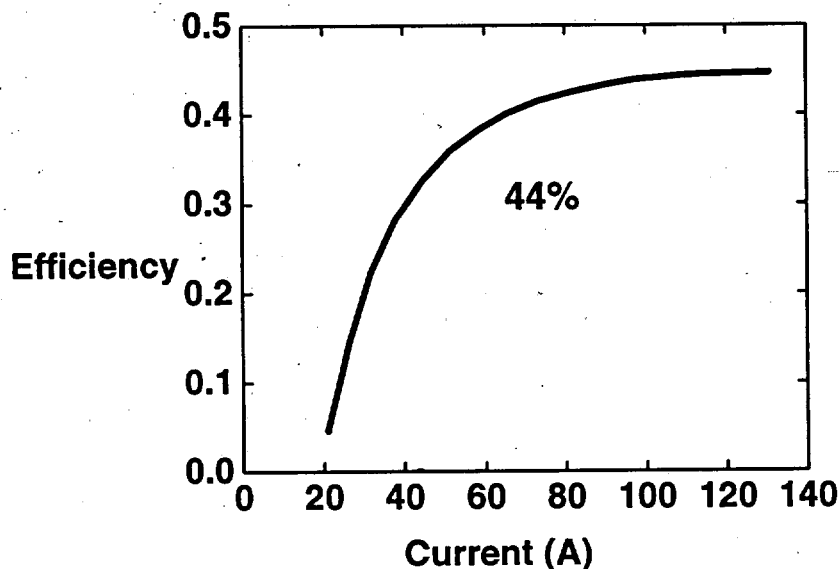


Fig. 2.1.8.2 Wall plug efficiency vs. power level of bar reaches a maximum of 44% at a peak drive current of 130 amps.

Diode lifetime is a complex issue since there are many factors that can negatively impact reliability. For the moment, we concentrate on early failures and long term degradation mechanisms that are specifically associated with the diode bar itself under normal operation. As stated previously, the AAA material represents an optimum design in performance and reliability due to the incorporation of In and the elimination of Al in the active layer, which reduces early failures and minimizes the propagation of darkline defects. We have not observed early failures, and have shown good long-term degradation

rates with the Coherent diode bars and our packaging approach. Shown below in Fig. 2.1.8.3 is data from a typical Mercury diode array reliability test in which a diode array consisting of 23 bars was operated initially at 2.3 kW of peak optical output power corresponding to 100 W peak per bar. This reliability test was carried out using 750  $\mu$ s pulses at 50 Hz. After 500 hours into testing, the peak power was increased to 2.7 kW corresponding to 115 W peak per bar. Over the  $1.5 \times 10^8$  shot life test, no appreciable degradation in diode performance was observed.

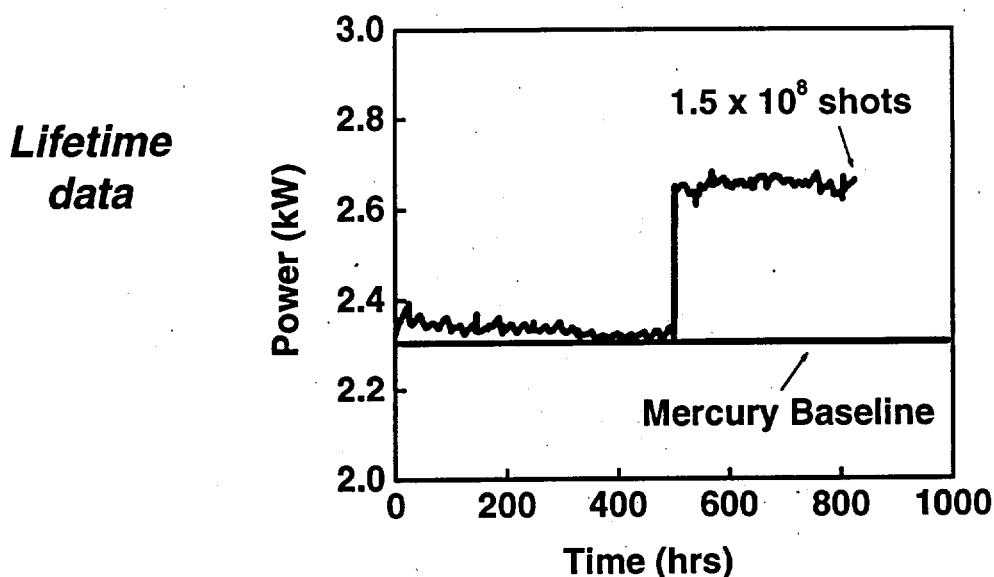


Fig. 2.1.8.3 Laser diode reliability test of 900 nm diode bars. This data is from a diode array consisting of 23 bars that was operated near room temperature. Initially the diode array was operated at a peak power corresponding to 100 W/bar, but was increased 500 hours into the life test to a peak power corresponding to 115 w/bar.

### **Diode Heatsinks**

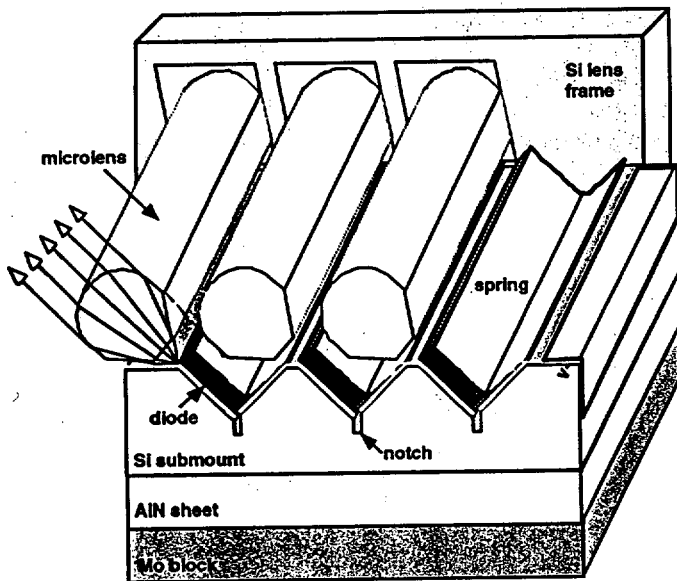
Dramatic improvements in both the performance and cost of packaging laser diode arrays will be critical for demonstrating a plausible pathway to advanced target shooters and IFE laser systems. A significant impediment to reducing packaging costs is eliminating the time and effort associated with handling large quantities of discrete components. We have chosen an approach that addresses these issues and introduces the following attributes:

- monolithic (to reduce the number of parts/processes and maintain accurate registration)
- formed from Si substrates (for large volume with micron-precision tolerances)
- reliable (using fluxless thin film Indium soldering process)
- minimal dead space (to increase excitance)
- simplicity (for low cost)
- microlens attachment to multiple bars in a single step

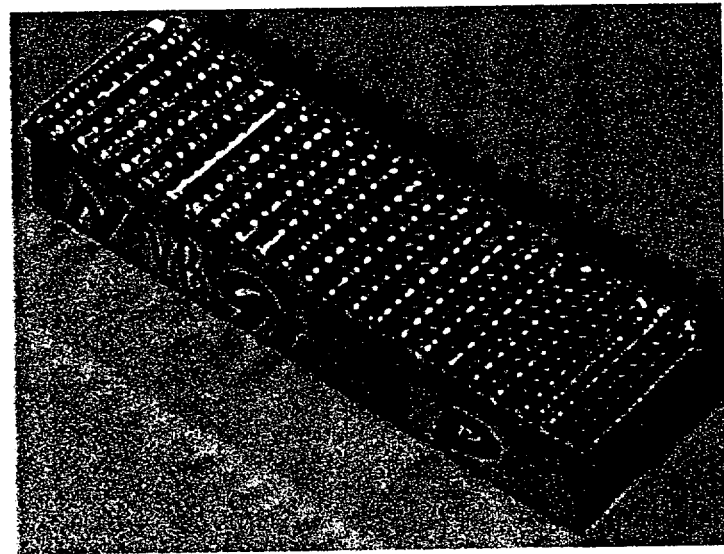
The laser diode array package, which we call V-BASIS (Bars and Springs in Slots) is shown in Fig. 2.8.1.4. The V prefix indicates that this architecture employs a V-shape design for mounting the diode bars, and that the laser emission is angled with respect to the substrate. The heatsink submount can be easily fabricated from a Si wafer that is wet etched at a preferred orientation to exploit the highly

anisotropic nature of the crystal's etch planes. A series of metallization layers deposited on the top of the substrate provides electrical continuity between neighboring diode bars, and a notch at the bottom of the V-groove produces an electrical break, necessary to avoid shorting the diode bars. The bars are directly soldered to these metallization layers, P-side down. A foil contact then completes the electrical connection of the bars by providing a conduction path from the top side (N-side) of the bar to the adjacent wall in the V-groove. Since the high reflector ends of the diode bars rest firmly against one side of the V-grooves, the bars are precision registered relative to one another, enabling a single microlens frame to be used in collimating the emission of all diode bars simultaneously.

Conceptually, the V-groove architecture balances the trade off between two competing problems for IFE suitable diode arrays. On the one hand, high peak irradiance is desirable which tends to reduce the diode spacing. However, the diode spacing must be maintained at some critical level to prevent thermal cross talk between neighboring diodes resulting from the thermal transient that occurs during the pulse. In the case of long pulses (0.75-1 ms) appropriate for IFE, the diode spacing must be kept greater than  $\sim 500 \mu\text{m}$ . With the V-groove design, there is negligible thermal cross talk while still maintaining a reasonably close packing density. The full opening angle of the V-grooves at  $109.5^\circ$  gives a 1.7 mm linear pitch for the 1 mm cavity length diodes used, but allows an optical pitch (looking in the direction of the emitted radiation) of 1.0 mm. Note that the V-groove also allows other manufacturing advantages, such as a simple means for diode insertion and inspection of the submount, which leads to a reliable, low-cost package.



(a)



(b)

Fig. 2.1.8.4 (a) Schematic diagram of V-BASIS laser diode array (3 of 23 diode bars are shown). Both the lenses and laser diode array have precise registration to enable a single active lens alignment. (b) The V-Basis package holds 23 bars and can output  $>2.6 \text{ kW}$  of peak power.

A finished V-BASIS tile is shown in Fig. 2.1.8.4 (b). Each "tile" is 1 cm x 4 cm and holds 23 diode bars. Previously, we had investigated the proper heatsink material to be chosen for Mercury-operated diodes. In the operating regime required for the Mercury laser, the thermal stresses are greatest during the transient pulse, so that a figure of merit (FOM) could be associated with a material in its ability to prevent heating of the laser diode during that pulse. The FOM is given by  $[\text{pC K}]^{1/2}$  (i.e., the temperature rise is inversely proportional to the square root of the volumetric heat capacity times the

thermal conductivity). Note that this expression assumes one-dimensional semi-infinite heat flow for time limits appropriate to Mercury. There are several key trade offs determining an optimum choice of starting material, including: thermal performance, cost, manufacturability, electrical conductivity, toxicity, and thermal expansion mismatch. The two most promising candidate materials were determined to be BeO and Si. From a thermal-performance point of view, BeO was preferable in having a ~40% higher FOM than Si. However, it was unknown if BeO heatsinks could be fabricated within the requisite tolerances and cost goals suitable for Mercury. Accordingly, we began a parallel R&D effort to investigate precision sawing/fabrication of BeO heatsinks. After exhausting the most advanced manufacturers (both external and internal to LLNL), we concluded that state-of-the-art machining had not advanced to the point to be acceptable as feature control and tolerances were insufficient for producing high-radiance, low cost, high volume, highly reliable diode arrays based on BeO. The Si-heatsink was thereby down selected as the baseline Mercury approach. It is noteworthy that the remarkable improvements in diode bar performance that Coherent has achieved during our program has now resulted in near equivalence of BeO and Silicon heatsink performance. Therefore, the outcome of identifying and developing a low cost, high performance diode array technology was successfully attained.

Typically, every V-BASIS diode package now produced goes through an accelerated burn-in for 18 hours at 75 Hz (~5 million shots) at a peak power corresponding to 115 W/bar, to eliminate infant mortalities. To date we have burned in more than 320 kW of finished diode arrays under these conditions, representing more than 3,300 individual diode bars. Fig. 2.1.8.5 shows typical burn-in data from a V-BASIS package.

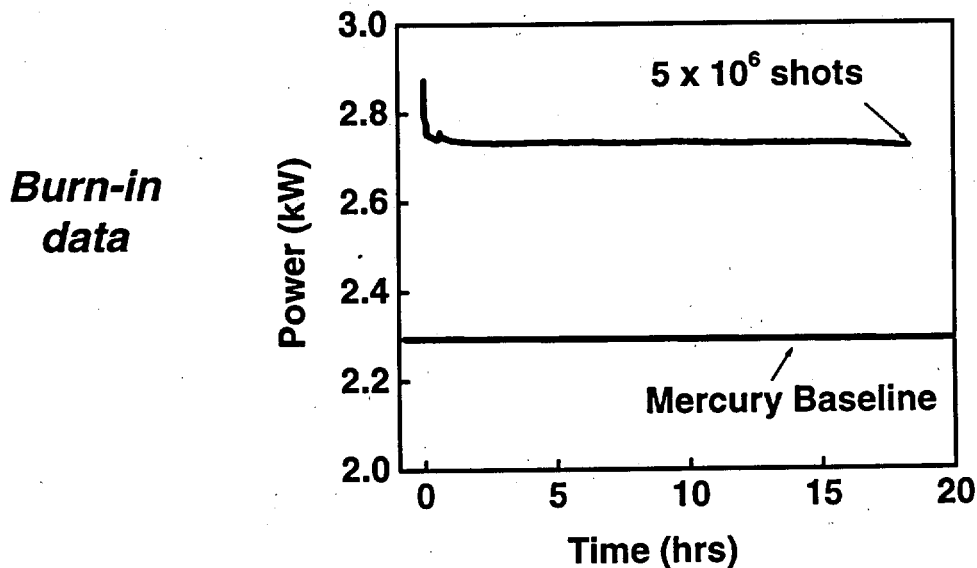


Fig. 2.1.8.5 Typical burn in data from a Mercury V-BASIS diode array. Every diode package is now burned in at a peak power corresponding to 115 W/bar for 18 hours at a 75 Hz prf (~5 million shots) to eliminate sudden failures.

If during a burn-in a bar is observed to fail, then the package is still useable after the bar is removed from the electrical circuit by simply shorting it out electrically. Bar sudden failures that require this shorting process are at about the 1% level (99% yield).



### ***Microlensing***

One of the benefits of the V-BASIS package from a production viewpoint is that it is manufactured using photolithographic techniques to define the V-grooves. This gives a precision of a few microns in the relative position of the V-grooves over the entire package, which then translates to the precision with which the diode bars can be registered relative to one another. It is this positioning precision that allows a tremendous simplification in microlens attachment, eliminating the need to line up individual microlenses with each diode bar. The microlenses can be held in precision frames fabricated in the form of silicon runners using the same anisotropic etching technology that is used to fabricate the V-grooves. Shaped cylindrical microlenses are then preloaded and glued into these silicon runners forming a ladder like structure consisting of 23 lenses as shown in Fig. 2.1.8.6. The entire 23-lens assembly is then attached to the SiMMs package in a single step. The microlens array serves to collimate the fast axis radiation of the laser diode bars from its original  $\sim 30^\circ$  divergence angle into a quasi-collimated beam with a divergence angle of  $\sim 1^\circ$ . The ability to attach microlenses to an entire V-BASIS array in a single step substantially reduces the number of fabrication steps that would be required if diode bars had to be lensed individually. The microlensing technology used on V-BASIS represents the state of the art available today. Fig. 2.1.8.7 shows both the slow and fast axis angular distribution of the emitted light from a V-BASIS package, which was determined by making a farfield intensity profile characterization of the package. The 13 mrad ( $\sim 3/4$  of a degree) fast axis divergence angle is easily maintained and reproduced with the LLNL microlens production and attachment technology that we have developed.

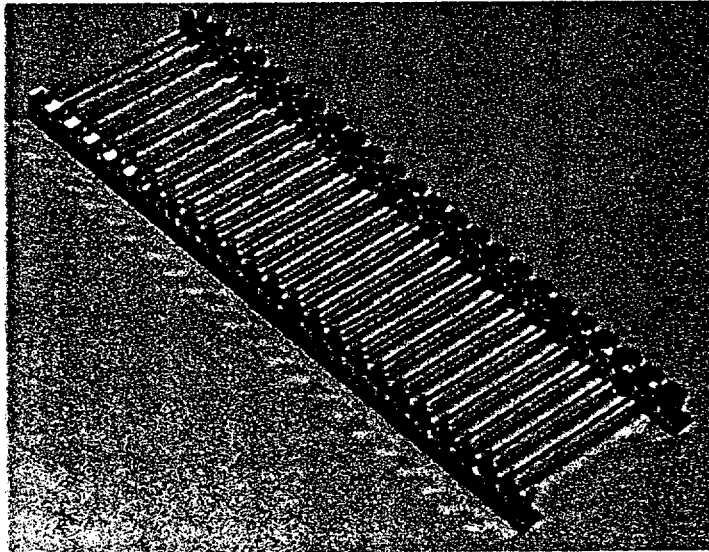


Fig. 2.1.8.6 Two silicon rails fabricated using the same etching technology that is used to define the V-grooves are used to precisely locate 23 shaped cylindrical microlenses that serve to collimate the diode fast-axis radiation. This assembly is aligned and attached to a V-BASIS package in a single step.

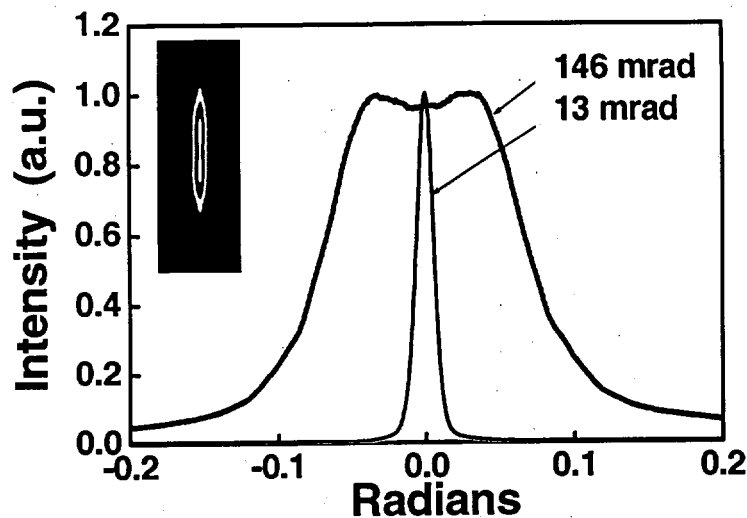


Fig. 2.1.8.7 The slow and fast axis angular distribution of the emitted light from a V-BASIS package, determined by making a farfield intensity profile characterization of the package. The measured fast axis divergence after microlens attachment is 13 mrad ( $\sim 3/4$  of a degree).

#### **Backplane Cooler**

Integration of the diode array tiles into a full array assembly is a challenging task with various trade offs. We designed the backplane with the following goals in mind:

- minimal dead space (for high excitance)
- negligible array pointing errors ( $< 1$  mrad)
- minimize optical delivery losses
- adequate thermal performance
- negligible thermal gradient (to avoid wavelength broadening)
- maintainability of the array (modular tiles)
- mechanical/environmental protection of the diode arrays

The concept chosen was to use a very large fluid-cooled backplane that individual diode array “tiles” are mounted to. Each backplane holds a total of 36 V-BASIS tiles in a 6 by 6 tile arrangement. This scheme is modular so that individual tiles can be removed and replaced in case of failure. To enhance brightness, the dead space between tiles is minimized to  $\sim 25\%$  of the tile area. The dead area between tiles is required for lens frames, electrodes, and mechanical tolerances. Electrical power is brought up through the backside of the backplane as shown in the diagram in Fig. 2.1.8.8. The positive electrode attaches to one side of the tile, and all tiles share a common ground (i.e., the backplane itself). The bottom of each tile is tapped to accept bolts that come through the backplane for good alignment (i.e., horizontal, vertical and angular). In addition, there is an indium foil gasket (not shown) between the mating surfaces to ensure good thermal contact. Adjacent to the bolts are coolant channels that are  $3/8$  inch in diameter in size. The deep, narrow channels are necessary for reducing the thermal impedance of the system,  $R_{th} \sim 1.2$   $^{\circ}\text{C}\text{-cm}^2/\text{W}$ . Despite the relatively low average power under Mercury operating conditions, the thermal power dissipated is a serious issue for the performance/reliability of the diodes, as well as for preserving wavelength control. At the 10 Hz operating design point of the laser, the junction temperature of the diodes is specified to have a temperature rise of  $\sim 15$   $^{\circ}\text{C}$  (roughly same amount of temperature rise during a single 750  $\mu\text{s}$  pulse).

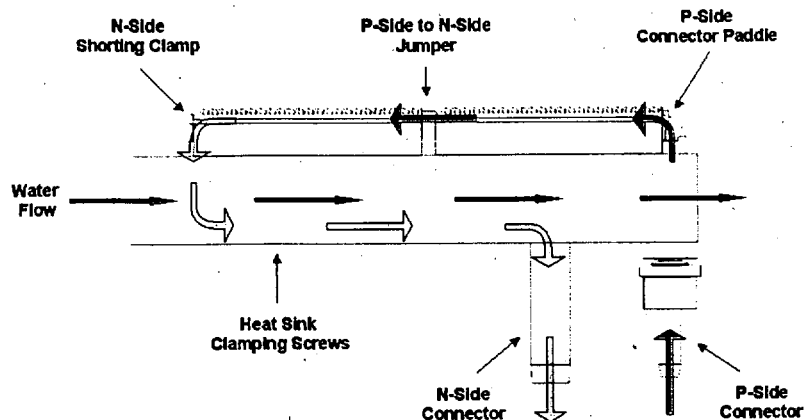


Fig. 2.1.8.8 Attachment of tiles to the backplane is modular allowing individual tiles to be replaced if necessary. The electrical feedthroughs and coolant channels are located on the backplane itself to minimize dead space across the array.

Four backplanes have now been completed and populated with a total of 144 V-BASIS tiles (36 tiles per backplane). In total, these four backplanes contain 3,312 individual diode bars with a combined peak power capability of >320 kW. The backplane is designed to operate from  $-40^{\circ}\text{C}$  to  $20^{\circ}\text{C}$ . This wide temperature range allows for more flexibility of repetition rate and wavelength tuning. To prevent any possible condensation, the diodes are hermetically sealed and are insulated by an outer enclosure that provides adequate thermal insulation, as well as mechanical protection of the diodes. Fig. 2.1.8.9 shows a photograph of two of the four completed backplanes in operation.

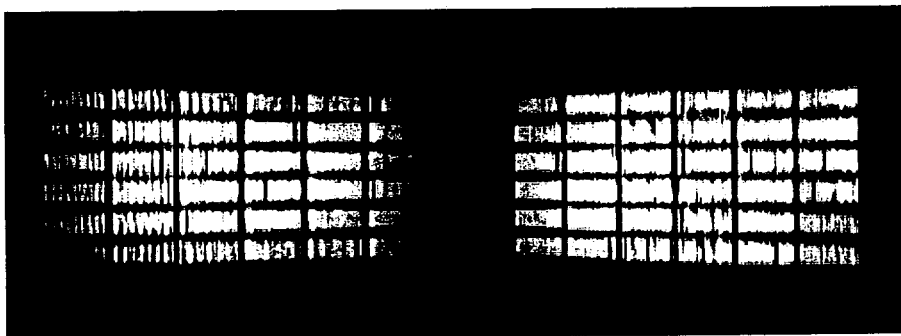


Fig. 2.1.8.9 Two blackplanes placed side by side with the laser diodes pulsing. These two units produce in excess of 160 kW of peak optical output power. In total four backplanes have been completed.

The tight wavelength tolerance that has been held on the diode bars delivered from Coherent Inc. is illustrated by the data of Fig. 2.1.8.10. Shown in Fig. 2.1.8.10 is the integrated spectrum of an output pump pulse from one of the backplanes at the Mercury operating point (750  $\mu\text{sec}$  pump pulse duration) overlaid with the absorption spectrum of Yb:S-FAP. The FWHM spectral spread in the pump pulse is 4.2 nm and matches well the absorption feature of Yb:S-FAP at 900 nm which serves to absorb the pump light.

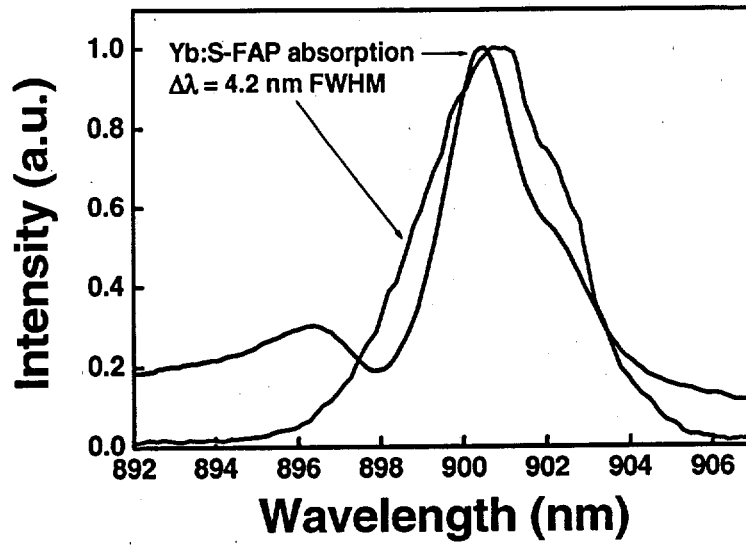
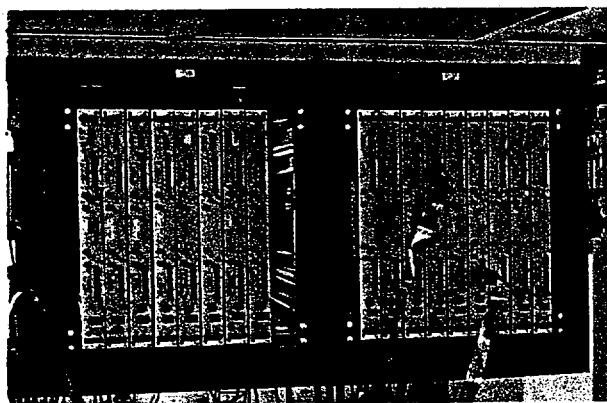


Fig. 2.1.8.10 The integrated spectrum of an output pump pulse from one of the backplanes at the Mercury operating point (750  $\mu$ sec pump pulse duration) overlaid with the absorption spectrum of Yb:S-FAP.

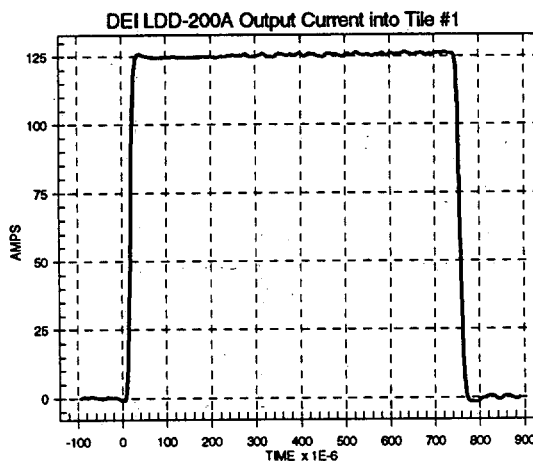
## 2.1.9 Diode Power Conditioning

The basic element in the diode power conditioning system is the LDD-200 pulse current source manufactured by Directed Energy, Inc. of Fort Collins, Colorado where aspects of the module were designed in conjunction with LLNL electrical engineers. Each pulser is connected to a laser diode tile pair through a low inductance strip line cable. The sources are mounted in overhead racks above the laser tables. External DC power is shared among nine pulser chassis. The driver consists of two independent channels in a common enclosure. The drivers share common AC support power, DC high voltage and water-cooling. Each channel is independently controlled via an RS-485 port. The driver provides analog, real-time voltage and current monitors that can be monitored using an oscilloscope. In addition, a measurement of the current and voltage amplitudes are available through the RS-485. The electrical limitations are listed in Table 2.1.9.1

The driver features advanced circuitry to protect both the diode and driver. These features include: A relay closure that mechanically shorts the output to ground when power to the driver is turned off. The internal capacitor bank is also shorted to ground at turn ON; at any time the driver is not pulsing and during a fault condition. The output is electronically crow barred to ground, ensuring that no current flows through the diode except during the on period of the pulse. If a fault is set during operation, the output pulse is truncated (turned off) prior to activation of the crowbar circuitry.



(a)



(b)

Fig 2.1.9.1 (a) Photo of 18 rack-mounted 2-channel pulsers installed in Mercury. (b) Typical output current waveform.

The nominal operating point for a single laser diode tile pair is 105 A at 130 V for 750  $\mu$ S at 10 Hz (example waveform Fig. 2.1.9.1b). Each channel of an LDD-200 can deliver up to 200A at 150 V for 1.5 ms with a 10 Hz repetition rate. This allows for a very flexible experimental envelope and leaves plenty of capacity for future expansion. The current sources monitor themselves for internal failures and "out of specification" computer commands. If a fault is detected the output pulse is immediately terminated, a "crowbar" switch is placed across the output, the high voltage DC power supply is disconnected, and the internal capacitor bank is discharged. A fault indicator lights on the front panel and fault code is made available to the control system. The pulser may not be re-enabled until the fault condition has been cleared.

Table 2.1.9.1 Comparison of diode operating points and pulser limitations

PARAMETER	NOMINAL LASER DIODE OPERATING POINT	MAXIMUM PULSER OUTPUT
Current	120 A	200 A
Voltage	130 V	150 V
Pulse Width	750 $\mu$ S	2 mS
Repetition Rate	10 Hz	10 Hz

### ***Laser Diode Protection System***

The laser diodes represent a significant cost factor in the Mercury Laser. Protection of these diodes during operation is a major design consideration of the pulsed power system. The pulsers developed for the Mercury Laser have a large reserve of available power and in fact are capable of delivering at least a factor of 14 more power than required at the maximum operating point of the laser diode tiles.

In normal operation it would be quite possible for the pulser to destroy its diode load. Additionally at the nominal operating point each pulser's capacitor bank stores approximately 310 J. In the event of a pulser failure this energy must not be delivered to the diode.

A four-pronged approach is taken to the problem:

1. Intelligent operators
2. Control Software to keep the diodes in their safe operating region regardless of operator input
3. Firmware within the pulser units
4. Hardware limits for some parameters and pulser faults

Each critical parameter and its solution are described below with a summary outlined in Table 2.1.9.2.

### ***Diode Current***

The control system software prevents the operator from requesting current outside the safe operating region. This value is stored in a configuration file that can only be edited by an administrative user with the proper password.

The pulsers will reject any command outside of its operating parameters. The pulser will continue to operate as before the illegal command, but an error status will be returned to the computer control system. Currently this limit is set at 220 A (10% above the 200 A rated output of the unit).

In case of a fault that results in current above the set point, the fault protection system is triggered. The output pulse is immediately terminated (within 50  $\mu$ S), a "crowbar" switch is placed across the output, the high voltage DC power supply is disconnected, and the internal capacitor bank is discharged through a series of "dump" resistors in the pulser chassis. A fault indicator lights on the front panel and fault code is made available to the control system. The pulser may not be re-enabled until the fault condition has been cleared.

### ***Diode Voltage***

The operator has no control of this parameter. The operating voltage expected for any requested current is calculated based on the values of  $V_{\text{threshold}}$  and  $R_{\text{slope}}$  input from the configuration file. If the voltage of the pulse sags below this value, such as if a single diode bar fails, this lower limit will be exceeded and a fault will occur. An upper limit of 150 V is built into the DEI firmware. This protection feature defends both the pulser itself as well as the diode load. If many diodes bars in an array should short the pulser would be asked to dissipate too much power possibly resulting in failure of the pulser output switches.

Additionally, the output voltage during the inter-pulse period is monitored (nominally  $V_{out}$  and  $I_{out}$  are zero during this period). If this voltage exceeds 10% of the nominal diode "on" voltage above, a fault condition is generated. Voltage output during this time period indicates a pulser fault that is causing CW current to flow in the load.

#### **Pulse Width**

As with diode current, the control system software will prevent the operator from requesting a pulse width outside the safe operating region. A "gated" mode in which the width of the triggered pulse determines the output pulse width is available but not used. As configured for Mercury, the pulser is edge triggered and an onboard digital counter determines the output pulse width. The DEI firmware has a hard limit of 2ms. As an additional protection the trigger distribution chassis limits (in hardware) the input pulse to 1 $\mu$ s. In the unlikely event that a pulser was placed in the gated mode, only a very short (and therefore safe) pulse could be generated.

#### **Pulse Repetition Rate (PRF)**

The control system software will prevent the operator from requesting a repetition rate outside the safe operating region. PRF is also limited in the Mercury system by hardware in the trigger regeneration chassis. A timed gate rejects any repetition rates greater than 10Hz. In addition, firmware limits the pulser PRF to 10 Hz.

Table 2.1.9.2 Summary of laser diode protection system.

<b>PARAMETER</b>	<b>OPERATOR</b> Values set by the Operator	<b>SOFTWARE</b> Values limited by the control system software	<b>FIRMWARE</b> Values limited by pulser firmware	<b>TRIGGER CHASSIS</b> Values limited by hardware in the trigger regeneration chassis
Diode Current	X	X	X	
Diode Voltage		X	X	
Pulse Width	X	X	X	X
Repetition Rate	X	X	X	X

## 2.1.10 Computer Controls

The architecture of the Mercury Laser necessitated that an automatic control system (Fig. 2.1.10.1) be developed to meet the needs of the system. In its final configuration the Mercury Laser will have 288 diode pulsers, 8 DC power supplies, 4 timing control boxes, 4 diode cooling systems, 2 slab gas cooling systems, and several diagnostic systems (Fig. 2.1.10.2).

### *System Hardware Architecture*

A block diagram of the Mercury control system hardware architecture is shown in Fig. 2.1.10.3. The control system utilizes a computer and programmable logic controller (PLC). These two devices are connected via a proprietary bus with an I/O card located in the computer. The computer is tasked with controlling the power to the diodes by controlling the amplitude and duration of current sent to the diodes. It is also responsible for the control of the external DC power supplies and control of the timing system. The PLC is tasked with control of the diode cooling systems, glass slab cooling systems, and with personnel and equipment safety. The status of the PLC is monitored by the computer system and the PLC accepts commands from the computer system.

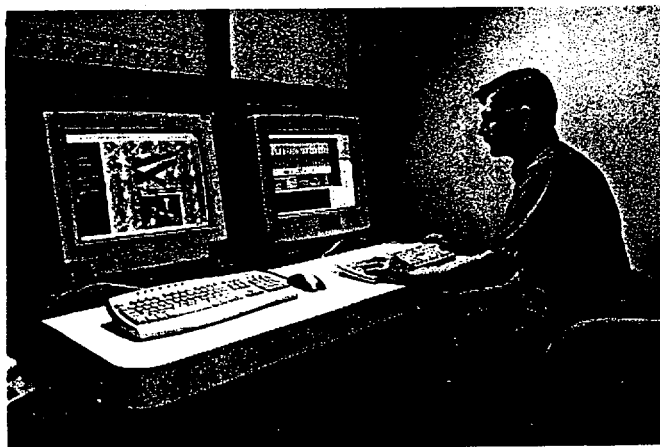


Fig. 2.1.10.1 Control console.

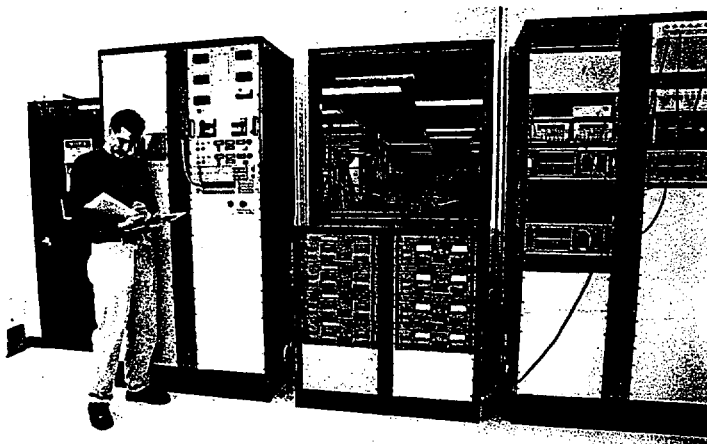


Fig 2.1.10.2 Gas controllers and power supplies.



The PLC controls and monitors the personnel safety interlocks, which includes doors into the laboratory, equipment cabinet doors, as well as other safety monitors as required. The PLC provides permissives to the power supplies and pulsers when requested by the control computer provided that all interlocks are in the safe condition. The PLC removes the permissives to the power supplies and pulsers whenever a condition occurs that could present a personnel hazard or a condition that would harm the equipment. An example of a personnel hazard is if a laboratory door were to be opened without the proper access code being provided. An example of a condition that could cause harm to the equipment would be if the cooling system operated outside of its preset limits.

## Controls – Hardware Diagram

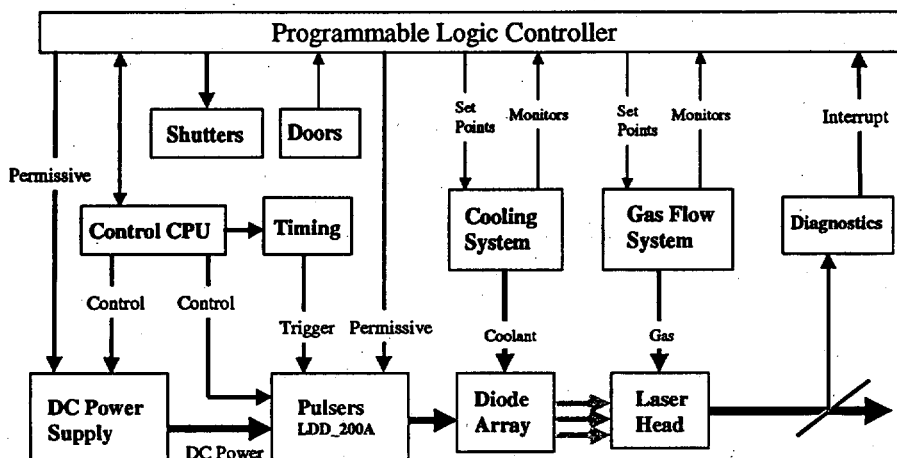


Fig. 2.1.10.3 Controls block diagram.

### System Software Architecture

The software in the control computer is written in LabVIEW. The software consists of modules providing a PLC Graphical interface as shown in Fig. 2.1.10.4 and a Pulser Control interface as shown in Fig. 2.1.10.5. Asynchronous communication between PLC and Pulser Control modules is done using Queues and Globals. Asynchronous communication between the various I/O functions within a module is done with the use of local variables and Queues. Each I/O function has a dedicated program loop such that a delay in one loop will not slow operation of the remaining control loops. For example, each pulser bay has its own COM port. If any one of the pulser channels on a particular COM port disrupts the communications, it will not effect the operation of the remaining pulsers or other I/O functions.

### PLC Operator Interface

The PLC interface (Fig. 2.1.10.4) provides the operator with status information on the cooling, gas flow, and interlock systems. Through the use of sub-menu screens this GUI allows the operator control of the Gas Controls, Interlocks and Shutters. Various systems interlocks may be by-passed.

### Pulser Controls Operator Interface

The main screen is shown in Fig. 2.1.10.5. The upper portion of the screen is a display of the detail status of a selected Pulser Bay. The display details information on the fault status of each pulser channel as well as temperature information and power supply status for the bay at large.

On the lower half of the screen are system wide indicators for Shot Count; Shot Rate; Pulse Width and configuration file name. There are global controls to configure and clear the pulsers; request permissives from the interlock system; control the power supplies and turn the pulsers ON and OFF. A "Fire" button is displayed during single shot operation.

The operator may select the "Edit Configuration" button to open a configuration editing screen as displayed in Fig. 2.1.10.6. From this screen the operator may modify operation parameters such as the whether a particular pulser channel is selected for operation and/or set the  $I_{op}$  and  $V_{th}$  for each pulser channel. The remaining indicators are for information purposes only and are not available to the operator.

This screen is initialized by displaying the current configuration that is in use. The operator has the choice of loading a new configuration from file or modifying the displayed configuration. Edited configurations may be saved to file for later use. Subsequently the operator has the option of returning to the main program with either the modified configuration or canceling the changes and returning with the original configuration.

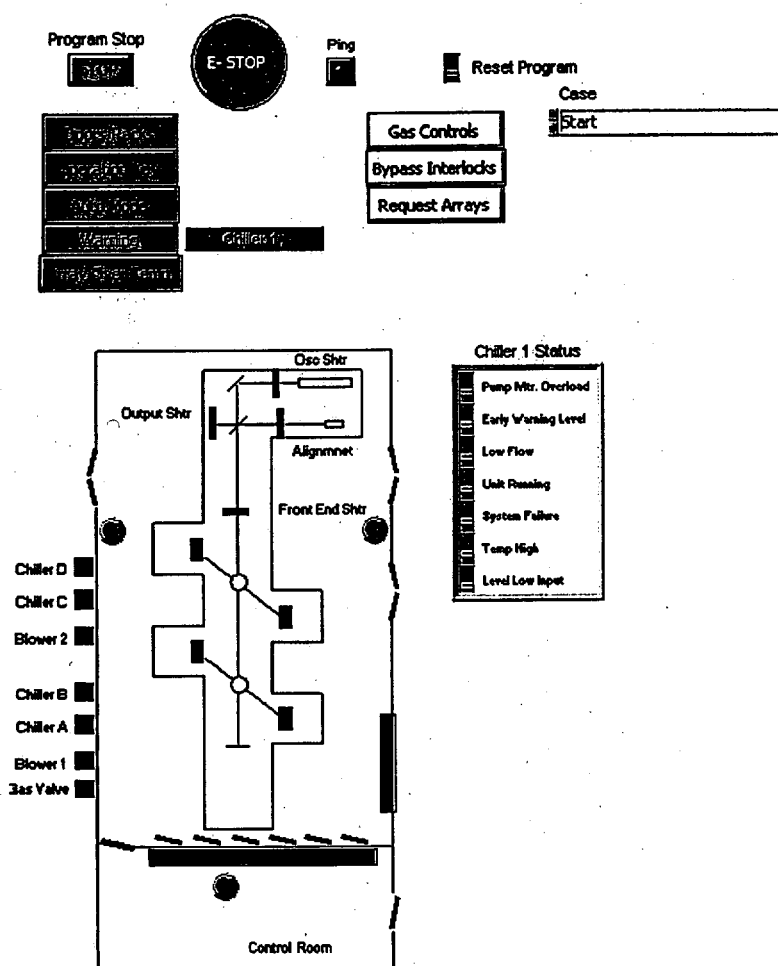


Fig. 2.1.10.4 PLC graphical user interface.

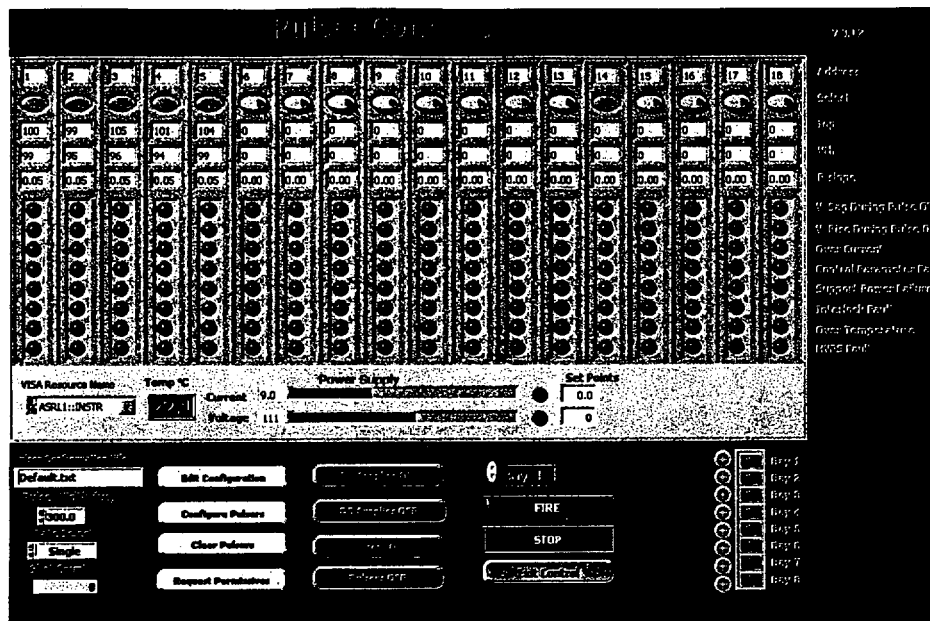


Fig. 2.1.10.5 Pulser control graphical user interface

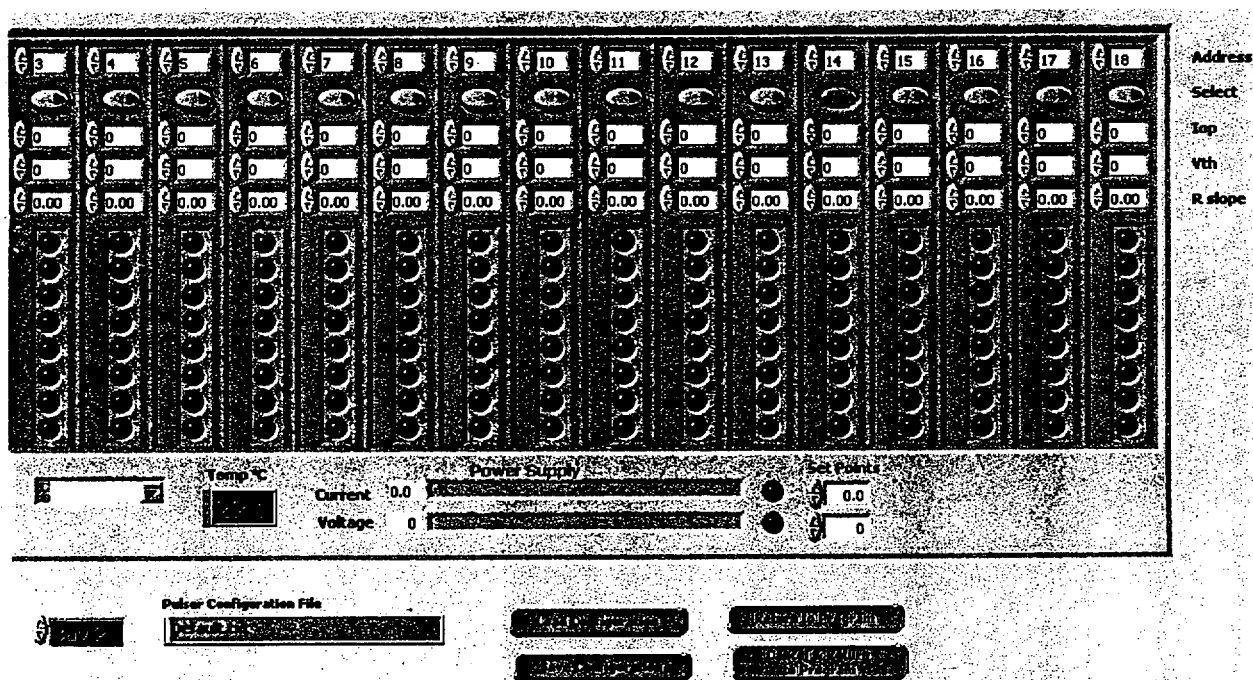


Fig. 2.1.10.6 Edit configuration screen.

## 2.1.11 Laser Generation of Neutrons (University of Texas)

### Summary

Work conducted under this project explored whether a fusion neutron source based on exploding clusters can be implemented on the completed Mercury laser (with a short pulse front end). Such a neutron source would enable materials radiation damage studies of various types, relevant to fusion reactor wall material development. We performed experiments this year to answer whether such a neutron source is feasible with the laser parameters available on Mercury. We experimentally examined whether longer laser pulses can be used in this approach (ps vs fs), and we ascertained the energy scaling of the fusion yield with laser energy.

### Principal goals of the work this year

- Measure scaling of DD neutron yield from current levels to 10 J on the LLNL JanUSP laser
- Explore means of scaling current femtosecond laser driven fusion to picosecond pulses
- Examine whether larger clusters can enhance yields for Mercury-like conditions

### Experimental Results

To date we have successfully initiated a set of measurements on the JanUSP laser at LLNL and have activated a cryo-cooled deuterium cluster jet. We conducted the first shot series in June of 2001 with the principal aim of measuring the yield scaling of DD fusion from exploding clusters of a sonic jet nozzle using both 100 fs and 1 ps laser pulses. This has allowed us to examine yield scaling well beyond the initial LLNL Falcon measurements at 0.1 J up to 10 J. We also successfully examined fusion yields to 10 J with 1 ps laser pulses. Our experiments used an  $f/2$  focusing parabolic mirror to direct the 10 J short pulses into a neat  $D_2$  cluster jet containing clusters of roughly 6 nm in diameter. Data from this experimental run are shown in Fig. 2.1.11.1a.

Our best observed neutron yields occurred at laser energy  $>5$  J; we measured up to  $3 \times 10^6$  n/shot when 100 fs pulses were employed. An examination of yield scaling from 0.1 J to 10 J (illustrated in Fig. 2.1.11.1b, with recent data from this project compared to older Falcon laser data) indicates that the yield increases roughly as the square of the laser energy. This trend is well understood and suggests that, it may be possible to produce  $10^8 - 10^9$  n/shot on Mercury, with no other changes than increased laser energy. Our measurements of yield at 1 ps (shown in Fig. 2.1.11.1a) also indicate that, while the yield is reduced somewhat when 1 ps pulses are used, the decrease is modest (much less than one order of magnitude.)

We intend to extend these studies to larger clusters yet (using deuterated methane). We have also designed a cryo-cooled supersonic jet, under test currently in University of Texas, Austin. This better collimated jet should mitigate the roll over in yield seen in figure 1a at higher energy, an effect attributed to absorption by the diffuse sonic cluster jet. We now have a shot series on JanUSP planned in January to explore these possibilities.

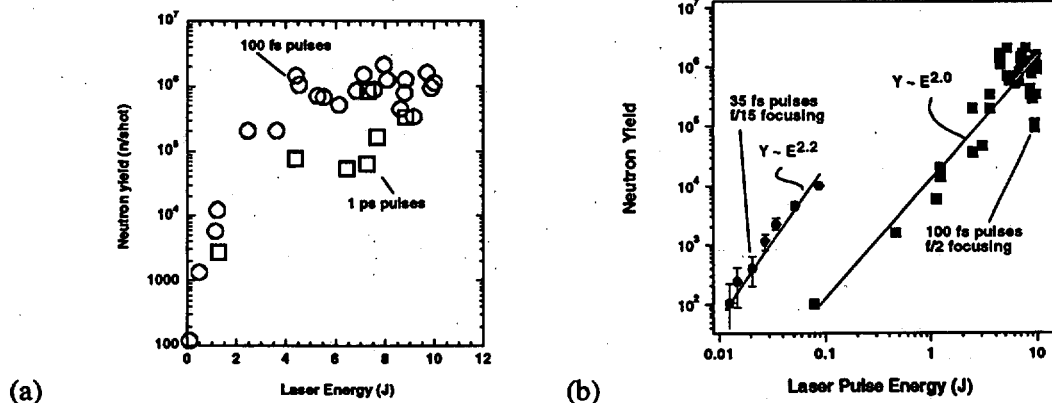


Fig. 2.1.11.1 (a) Measured neutron yield vs laser energy (b) Neutron yield scaling from 0.1 to 10 J.

## 2.1.12 Spectral Sculpting Experiments and Evaluation of Average Power Frequency Conversion Design (University of Rochester)

### *Spectral Sculpting Experiments*

All solid-state laser systems envisioned for Inertial Fusion Energy (IFE) applications, such as the Mercury laser, will require some form of advanced beam smoothing in order to improve the single-beam on-target uniformity. This beam-smoothing requirement dictates that these lasers have an amplified FM bandwidth of  $\sim 1/3$  THz prior to frequency conversion. This is comparable to the gain-bandwidth of solid-state gain materials such as  $\text{Yb}^{+3}:\text{SFAP}$ , and thus gain-narrowing in these amplifiers will significantly reduce the on-target bandwidth. In addition, gain narrowing will also produce severe, potentially damaging, amplitude modulation (AM) at the output of the laser system. Precision spectral sculpting permits relatively narrow-band laser systems to produce purely Frequency-Modulated (FM) (i.e., with no AM) pulses at their output with FM bandwidths approaching that of the system's gain bandwidth.

Spectral sculpting precompensates the effects of gain narrowing. Prior to amplification, the FM spectrum of the input pulse is "sculpted" by exactly the amount of gain-narrowing expected. Specifically, a spectral mask that attenuates the high-gain line-center sidebands and wholly transmits the distant low-gain sidebands is applied to the pulse at the input to the laser system. After sculpting, this low-energy, low fluence, input pulse no longer has a purely FM spectrum and is thus heavily amplitude modulated. As the pulse is amplified through the system, the sculpted spectrum evolves toward a purely FM spectrum with no AM. At the output of the system, precisely where the energy, fluence, and concomitant damage threat are highest, the purely FM spectrum is recovered, with no AM.

This project had the primary goal of successfully demonstrating broadband FM amplification in a model narrowband solid-state gain medium ( $\text{Nd}^{+3}:\text{YLiF}_4$ ). A successful demonstration would deliver a pulse amplified by the same amount of gain expected for the Mercury system with the original purely-FM spectrum. A successful demonstration would also show a reduction or elimination of the AM at the output of the model system. Finally the project should explore the range of practical applicability of the particular embodiment of spectral sculpting used. All of these goals were met.

Our spectral sculpting approach is based on the Fourier transform pulse shaping technique described by Weiner<sup>1</sup>. A diagram of the shaper is shown in Fig 2.1.12. The spectrum of a temporally smooth, FM pulse is spatially dispersed by a diffraction grating and focused onto a spectral mask. The mask is a computer-controlled, pixilated, liquid-crystal spatial light modulator (SLM) that provides control of both the amplitude and spectral phase of the FM spectrum. The dispersion and imaging of the shaper are designed such that each FM sideband is incident on a single SLM pixel. After modification by the SLM, the input spectrum is re-imaged and recombined.

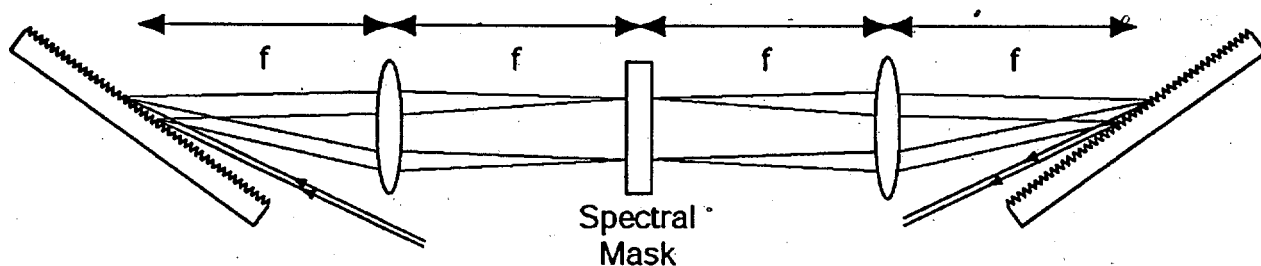


Fig. 2.1.12.1. A diagram of the spectral sculptor.

The experimental parameters for our demonstration system were chosen to be similar to those required for the Mercury laser system. In specific, a gross small signal gain in  $\text{Yb}^{+3}:\text{SFAP}$  of  $\sim 10^4$  and an infrared bandwidth of 330 GHz are required. Our system produced the same gross gain as required for Mercury, but, since the gain bandwidth of  $\text{Nd}:\text{YLF}$ , used in our system, is about two-thirds as broad as that of  $\text{Yb}^{+3}:\text{SFAP}$ , we chose to work with a bandwidth that is two-thirds as large (ie. 220 GHz).

The spectrum of the original FM pulse (Fig. 2.1.12.2a) has a center wavelength of 1.053  $\mu\text{m}$  and is composed of over 25, 10.4 GHz spaced sidebands. The corresponding smooth temporal profile of this pulse is shown in Fig. 2.1.12.2b. Without sculpting, the effects of spectral gain narrowing on the amplified pulse spectrum are clearly evident, as shown in Fig. 2.1.12.2c. The corresponding temporal measurement (Fig. 2.1.12.2d) of this pulse shows significant amplitude modulation due to gain narrowing.

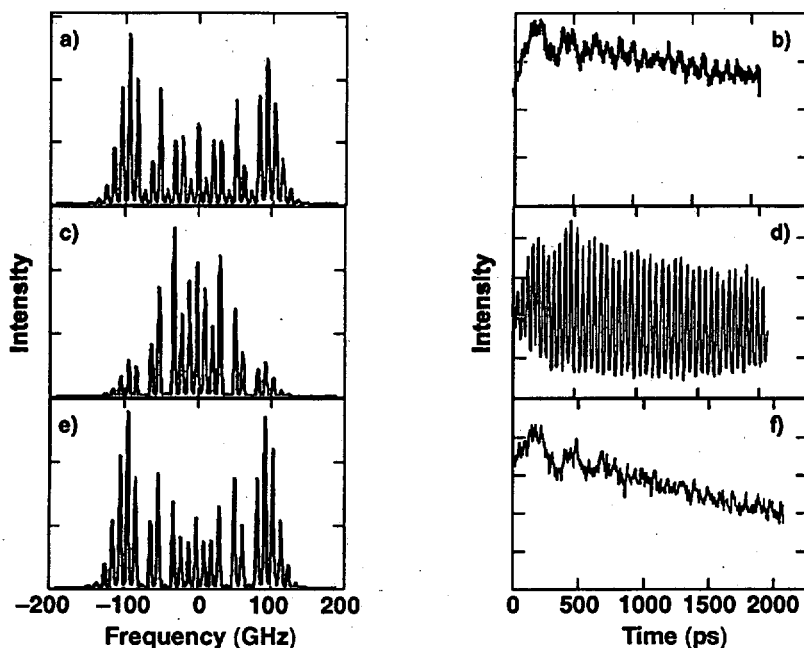


Fig. 2.1.12.2 (a) Unamplified FM pulse spectrum. (b) Streak camera measurement of the temporal profile of the pulse whose spectrum is shown in (a). (c) Gain narrowed, amplified FM spectrum. (d) Temporal profile corresponding to the gain narrowed spectrum shown in (c). (e) Amplified, sculpted FM spectrum. (f) Temporal profile corresponding to amplified, sculpted spectrum shown in (e). Note that amplitude and phase sculpting produce an amplified pulse with the original FM spectrum and no amplitude modulation.

Given a measurement of the gain-narrowed spectrum, the transmission of the LCM can be programmed to produce the original FM power spectrum at the amplifier output (Fig. 2.1.12.2e). In addition to producing the specified amplified spectral bandwidth, temporally smooth pulses are also required. We found that amplitude sculpting alone was not sufficient to eliminate all of the AM shown in Fig. 2.1.12.2d. Taking advantage of the fact that the programmable SLM is also capable of spectral phase sculpting, we were able to compensate the anomalous dispersion associated with the narrowband Nd:YLF transition, producing an amplified temporal pulse with no amplitude modulation (Fig. 2.1.12.2f).

For total gross gains exceeding that required for the Mercury laser, we have shown that with proper amplitude and phase compensation, one can successfully amplify broadband FM pulses in a narrowband solid-state gain medium. We generated amplified pulses whose spectra are identical to the initial unamplified FM spectra. In addition, with proper phase control, we were also able to produce amplified pulses that do not exhibit temporal amplitude modulation.

[1] A. M. Weiner, Rev. Sci. Instrum., 71 1929 (2000).

### *Evaluation of Average Power Frequency Conversion Design*

The crystals available for large aperture, high average power frequency conversion of the Mercury laser system have been evaluated. The materials suitable for efficient narrow-band frequency conversion include DKDP, YCOB, and BBO (KD<sub>2</sub>PO<sub>4</sub>, YCa<sub>4</sub>O(BO<sub>3</sub>)<sub>3</sub>, and BaB<sub>2</sub>O<sub>4</sub> respectively). Using the existing data, these materials were evaluated based upon standard frequency conversion models which take into account thermal loading, nonlinear coefficient, optical absorption, and conductivity. Our computational models have simulated the expected performance of each of these materials and were summarized in a detailed internal presentation entitled "New Materials for High Average Power Nonlinear Optics". In addition we have put together a conceptual hardware design based on the gas cooling concept that has already been implemented on the Mercury Laser for Amplifier slabs.

Finally, we have begun collaborating with Dr. John Lambropoulos and his graduate students of the University of Rochester. The team consisting will be working on upgrading the frequency conversion models to include thermal dephasing.

## 2.2 Chambers

Our primary goal for FY01 was to initiate the design process for alternate (e.g., other than the gas-protected, dry-wall Sombrero concept) chamber concepts. This process began with an extensive literature review, which was followed by a down-selection to three chamber concepts. Following additional review, we further down-selected to two areas of study: magnetic protection and fast ignition. These areas are supported by an additional effort in safety and environmental analysis, which also supports the broader HAPL program through the Laser IFE Materials Plan and the Materials Working Group. We also support the mainline Sombrero chamber concept through our work in neutron damage modeling for chamber materials such as graphite. Finally, we are improving the laser IFE systems modeling tools and using these tools to conduct systems studies for laser IFE power plants.

### 2.2.1 Magnetic Protection

Currently available laser IFE target designs emit a significant fraction of their output in the form of energetic ions. These ions represent a significant threat to the first wall and final optics. Sombrero utilized sufficient gas to stop all ions before they damaged the first wall and final optics. Fig. 2.2.1.1a shows ion trajectories for 1.65 MeV carbon ions, which were the dominant ion threat for Sombrero. Note that all ions stop short of the first wall, which would sit at a radius of 6.5 m. Recent work, however, suggests that large fluxes of high-energy ions will reach not only the first wall but also the final optics. A plot of the charged particle trajectory for carbon ions emitted by the NRL radiation pre-heated target is shown in Fig. 2.2.1.1b.

These results assume charged particle transport through a neutral gas. An outstanding issue that has not been addressed in the ion damage work thus far is the effect of the pre-ionization of the chamber gas by the x-ray pulse that precedes the ions. Significant ionization of high-Z gases might significantly increase the stopping effectiveness of the gas, thereby reducing the threat to the first wall and optics. This effect will be investigated and quantified in future work.

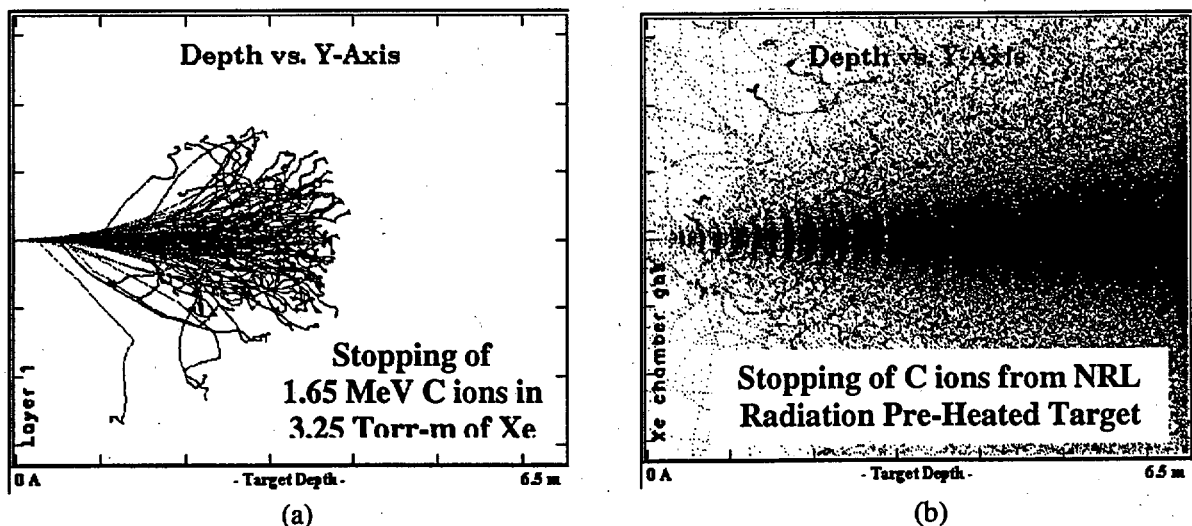


Fig. 2.2.1.1 (a) The original Sombrero study used 3.25 Torr-m of xenon gas to stop all ions. (b) Recent work suggests that large fluxes of ions may reach the first wall.

A literature search was conducted for ion radiation damage to materials of interest to laser IFE. Our findings suggest that the high fluxes of ions that are to be expected would lead to significant changes



in chamber wall and optical materials. Properties such as the thermal conductivity and even strength would be affected in chamber wall materials. Optical properties such as reflectivity and transmissivity would also be affected. Significant ( $> \lambda$ ) thicknesses of optical materials might be removed by sputtering, and exfoliation might be even more severe. Chamber walls would experience 10's of microns of material removal per year. This would likely be acceptable from a structural standpoint, however, migration of the resulting 10's-100's of kilograms of wall material per year might be problematic for the optics and/or cause excessive tritium co-deposition.

Two factors have combined to increase the threat to the first wall. First, the ion output from target designs such as the NRL radiation pre-heated targets is considerably "harder" than that used in the Sombrero study. It is worth noting that target design activities were not a part of the Sombrero study. Direct-drive targets that have been analyzed in detail have charged particle spectra extending to 20 MeV and higher.

The second factor that has worked to increase the ion threat is the reduction in the chamber fill gas. Work completed under the auspices of the ARIES program included the discovery that target heating during injection was excessive. To reduce target heating, the gas density was reduced from 0.5 Torr to only 10 mTorr. At this level, the chamber wall heating from ions and x-rays is thought to be acceptable (melting and/or vaporization is avoided).

Given the large increase in ion fluxes incident upon the first wall, radiation damage from ions is a significant issue. One method to deal with the large ion output is to protect the first wall and optics via magnetic deflection of ions towards an engineered sink. Magnetic deflection may not only protect the first wall and optics from ion radiation damage, but it may reduce tritium co-deposition with carbon, which is a significant safety and environmental concern.

Redirected ions must be confined long enough for them to escape through loss cones at the "ends" of the magnetic fields where they will flow into either a beam dump or direct converter. MHD instabilities may cause travel across field lines and result in "lost" (unconfined) particles, which may strike the first wall or final optic. We require a three-dimensional, fully electromagnetic code that can model electrons as a fluid. The code must be multi-species because the target contains elements in addition to D and T, and we need to model the presence of background gases such as xenon. The electrons need to be a fluid so that the code time steps can be of reasonable length. A particle in a cell (PIC) formulation of this problem contains the necessary physics. A survey of available PIC codes was completed, and a decision to use Lsp, which is developed and distributed by Mission Research Corporation (MRC), was made. The code was procured, and MRC personnel are providing consulting services.

Lsp will be used in conjunction with TOSCA3D. TOSCA3D is produced by Vector Fields Corporation. It is a three-dimensional finite element code that is an "industry standard." TOSCA3D contains a very general magnet configuration package and includes a module that calculates the effects of the magnetic field generated by an ion beam on an external magnetic field. This will enable us to account for the effects that high-energy ions may have upon the fields produced by the external magnetic coils.

Fig. 2.2.1.2 shows one magnet layout that will be analyzed with Lsp and TOSCA3D. Large (15-m-diameter) magnet coils are shown above and below chamber center in a mirror configuration. Exit ports for the deflected ions are located at the top and bottom of a variation of the Sombrero chamber/blanket design.

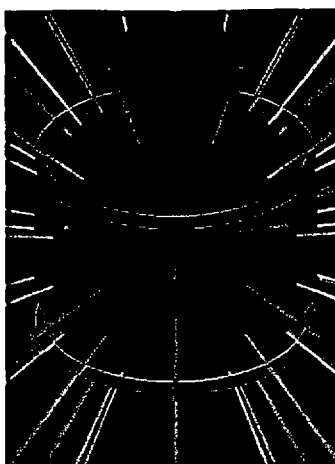


Fig. 2.2.1.2 Sombrero can be equipped with deflection magnets to reduce the ion fluxes incident upon the first wall and final optics. Shown are sixty beamlines (some are truncated in this view), exterior of the blanket, and two deflection magnets.

Magnetic deflection calculations will be performed for a variety of coil configurations and assumptions. Key results will include the ion capture efficiency and the escaping ion fluxes and spectra incident upon the first wall and final optics.

## 2.2.2 Fast Ignition

In FY01 we completed a preliminary assessment of Fast Ignition laser IFE. This work was reported in a presentation and paper for the ISFA2001 conference. We included economic potential, target fabrication and injection, final optics requirements. This initial evaluation pointed out several potential advantages including:

- High gain ( $> 100$ ) at low driver energy ( $< 1$  MJ) reduces the recirculating power for the driver, driver cost and the cost of electricity (COE).
  - Possibility for smaller-scale, lower-cost development steps
  - Competitive COE with smaller plant sizes ( $< 1000$  MWe)
- High gain with two-sided, indirect-drive for fuel compression
  - This would allow use of thick-liquid-wall chambers giving long-life structures
- Less demanding requirements for fuel compression
  - Perfectly symmetric implosion not required as in hot spot ignition
  - Lower overall density ( $\sim 100\text{-}300$  g/cm<sup>3</sup> vs.  $500\text{-}600$  g/cm<sup>3</sup>)
- Relaxed fuel compression requirements lead to other benefits
  - Relaxed drive symmetry (indirect-drive, possibly even one-sided?)
  - Relaxed target fabrication requirements
  - Targets less susceptible to thermal and mechanical damage during injection
- Possibility of igniting advanced fuels with reasonable driver energies
  - Tritium self-breeding in target would allow use of non-Li bearing liquids in thick-liquid-wall chambers
  - High charged particle output compatible with direct conversion
  - Advanced fuels, however, ignite at a higher temperature, so will require more compression.

Achieving that extra compression will require tighter specs, perhaps offsetting gains listed in the first bullet.

There are also several significant challenges that must be addressed. These include:

- Target physics
- Target fabrication – Added features such as high-z cone for ignitor beam complicate fabrication
- Target injection and tracking – How do requirements differ from direct drive?
- Beam propagation through blow-off plasma from compression beams
- Beam focusing to small spot size (typically  $< 50 \mu\text{m}$  diameter) and timing to  $< 100 \text{ ps}$  (compressed core dwell time)
- Size, location, and protection of final optics
- Impact of chamber conditions (e.g., residual vapor) on propagation, focusing of ignitor beams

Fig. 2.2.2.1 shows the diffraction limited focal spot size as a function of focal length for two different size optics, 50 and 100-cm diameter. To hit a  $33 \mu\text{m}$  spot, typical of fast ignitor target requirements, will limit the standoff to no more than 13 m for 50-cm-diameter optics and 27 m for 100-cm-diameter optics. Large standoff is desirable to reduce the open solid-angle fraction and possibly protect the final optics from radiation damage caused by target emissions. This indicates the importance of developing large scale focusing optics.

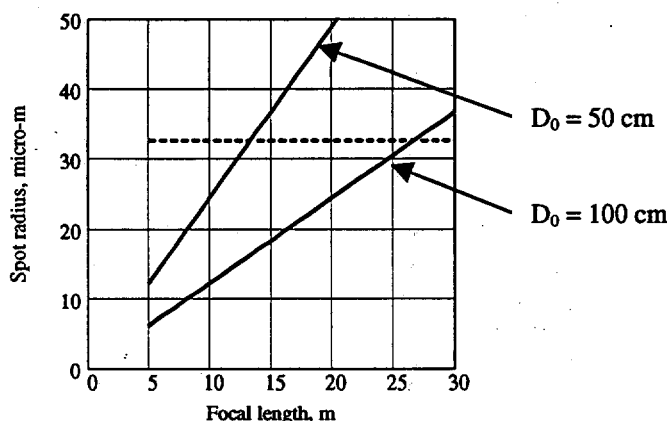


Fig. 2.2.2.1 Spot radius versus focal length for 50 and 100-cm-diameter final focus optics assuming diffraction-limited beams. The dashed line at  $33 \mu\text{m}$  is a typical spot size requirement for FI targets.

## 2.2.3 Safety and Environment

In FY01 we completed safety analyses for the baseline Sombrero design. These included loss of coolant and loss of vacuum accidents. This work demonstrated the importance of ensuring that oxygen does not reach the C/C composite chamber and blanket when it is still at an elevated temperature. Following our initial analyses, work at INEEL confirmed our results, and the UW proposed possible mitigation schemes.

We provided support to the Materials Working Group during the latter part of FY01. This consisted of guidance in the selection of target (high-Z overcoat) and first wall materials. Radiological indices of interest were calculated for all naturally occurring elements from lithium to bismuth. We also provided a summary of the neutron, ion, gamma-ray, and x-ray threat spectra for the first wall and final optic.

Finally, we implemented the ability to calculate clearance ratings within our neutron activation code. Cleared materials would be even more desirable than those that could be disposed of as low-level waste via shallow land burial. Such materials would no longer be counted as "waste." This tool was applied to the baseline Sombrero design. Unfortunately, it appears unlikely that the major components will qualify for clearance. Clearance results will be presented at the ISFNT-6 conference.

## 2.2.4 Radiation Damage Modeling for Chamber Materials

During FY01 we have implemented an interatomic potential to study C/H/O systems in our parallel molecular dynamics code, the so-called bond order potential. This potential is the most accurate empirical potential to date to study graphite and graphite-like structures since it stabilizes the  $sp^2$  and  $sp^3$  bonds in carbon. The potential includes H, therefore calculations of migration energies and binding energies of H with defects produced during irradiation are possible. Our simulations show a large binding energy between H and a single vacancy, 3.8 eV. These energies are essential input parameters for predictive models of tritium retention and tritium inventories in irradiated carbon-based materials.

This potential is also being used to study the damage produced by energetic recoils in graphite. We have calculated the damage produced by a 200 eV recoil. This energetic atom produces vacant sites in the graphite planes (see Fig. 2.2.4.1) that could act as trapping sites for tritium. This information will be combined with the number of defects produced as a function of energy in order to predict dpa levels on these materials. This information is being calculated with our molecular dynamics simulations.

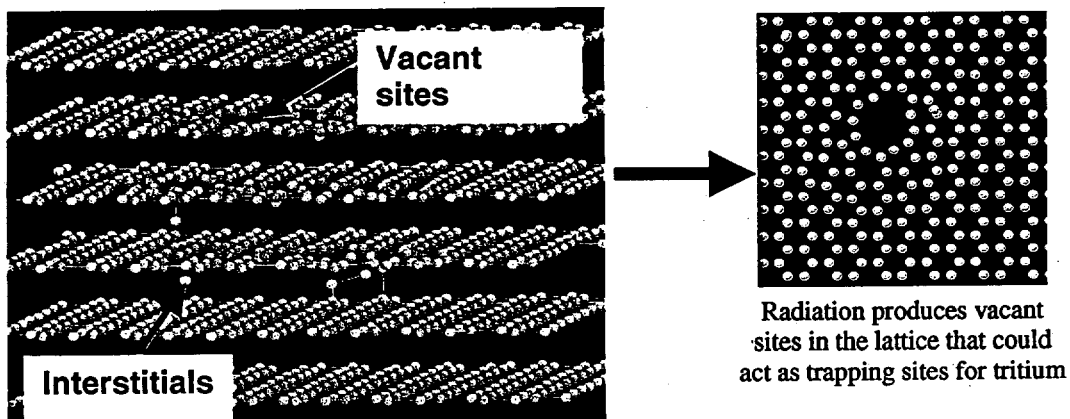


Fig. 2.2.4.1 Damage produced by a 200 eV C recoil along the c-direction in graphite

## 2.2.5 Systems Modeling

During FY01, advances in systems modeling were made in three main areas. First, the potential economic benefits of Fast Ignition for Laser IFE were evaluated using the existing system models for the Sombbrero chamber and plant. The laser cost was parameterized on a \$/J basis and the laser efficiency was fixed making the result more general than specific to a particular driver (DPSSL or KrF) model. Fig. 2.2.5.1 shows the potential economic benefits of fast ignition. With FI targets, the cost of electricity is 12-37% lower than direct drive targets (depending on which adiabat  $\alpha$  is assumed), and the optimal driver energy is significantly lower, which could have some development path benefits.

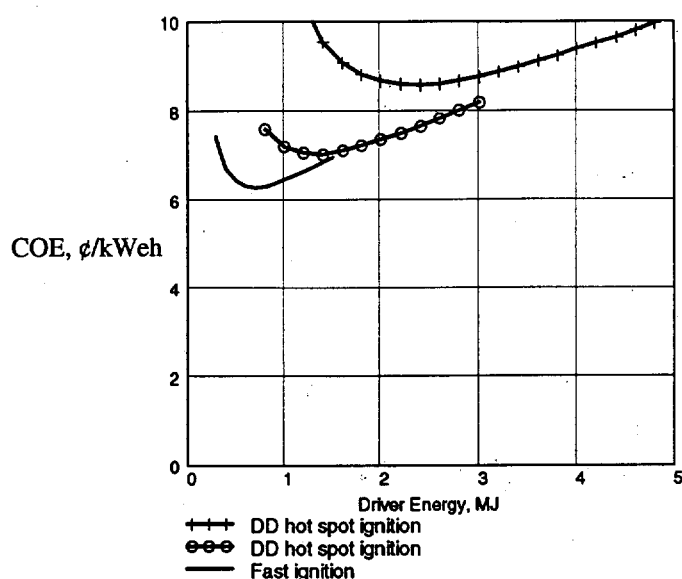


Fig. 2.2.5.1 Cost of electricity versus driver energy for different target gain curves: top curve is for direct-drive hot spot ignition with  $\alpha = 2$ , middle is direct-drive hot spot ignition with  $\alpha = 1$  and beam zooming during implosion, and the lowest is for fast ignition.

Second, the LLNL DPSSL code (written by Charles Orth) was used to develop a simple driver cost scaling relationship for a DPSSL. This simple scaling was used in the Mathcad version of the Sombrero power plant code to evaluate the sensitivity of the cost of electricity to direct-drive target performance and laser efficiency. Fig. 2.2.5.2 shows that the importance of high driver efficiency increases as target gain performance decreases. These results were reported at the November 13-14 HAPL meeting in Pleasanton.

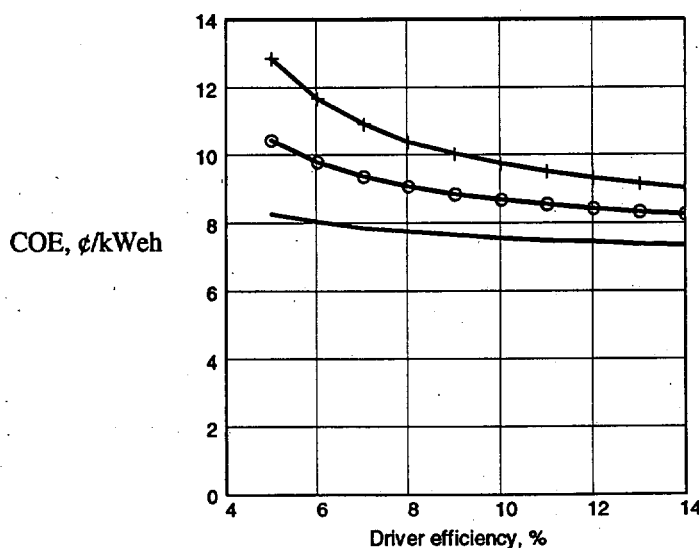


Fig. 2.2.5.2 Cost of electricity (COE) versus driver efficiency for direct drive targets with implosion adiabats of  $\alpha = 3, 2$ , and  $1$  (from top to bottom). Assumes 1000 MWe net power for plant. For  $\alpha = 2$ , increasing the driver efficiency from 5 – 10% decreases the COE by 17%.

Third, significant progress was made in restructuring the LLNL DPSSL code. The code has been divided into subroutines to allow easier identification and improvement of the physics, engineering and costing modules. This is necessary first step in the process of updating the code with improved and new models and improving its flexibility to examine applications other than power plants (i.e., to allow assessment of IRE drivers).

## 2.3 Final Optic

The most fundamental threat experienced by the final optic in inertial fusion energy is that imposed by the neutrons and gamma rays, since MeV ionizing radiation cannot be blocked without impeding the laser light itself. These threats are also important in NIF, although much less severe because of its lower repetition rate.

### 2.3.1 Gamma and Neutron Irradiation Studies

During FY01, most of our effort has been applied to devising a solution for the 355 nm SiO<sub>2</sub> final optic. The crucial issues have been substantially addressed: radiation-hardness, cooling, and fabrication. The suggestion is to use a thin (< 0.5 mm) diffractive optic, which both focuses and deflects the 355 nm beam. The optic becomes absorptive as a consequence of the generation of defects, which leads to the need for cooling.

The conclusions are based on the availability of SiO<sub>2</sub> 1 cm<sup>3</sup> samples that were irradiated on LANSCE (at LANL) in the 1995 timeframe for a period of about 3 months. The neutron spectrum of LANSCE, peaking near 10 MeV, is a reasonable rendition of the expected IFE neutron irradiation. In any case, the LANSCE dose is probably more severe than that of IFE, since neutrons as high as 100 MeV are present. The samples are extremely "hot" having contact doses of >1 rem/hr, presenting problems in safety and handling.

The most significant result was the realization that the defect formation *saturated* at an absorption level of 1 cm<sup>-1</sup> at 355 nm. The six different samples irradiated at temperatures between 100 – 200 °C all saturated at the same level to within 20 %. Fig. 2.3.1.1 is a plot of the absorption spectra for a sample that was irradiated at 105 °C and annealed at 380 °C. A pair of samples irradiated at 426 °C evidenced far less absorption at 355 nm (~0.1 cm<sup>-1</sup>). Fig. 2.3.1.2 shows the absorption resulting from irradiation at higher temperature. The absorption of these high temperature samples was confused at first because the surfaces exhibited enormous amounts of scatter, in the range of 10-13 %/surface. After consideration of the mechanisms of surface scatter, it was concluded that it is likely a chemical phenomenon (perhaps due to etching in the acidic environment of the LANSCE chamber). Another important observation of the samples was that they exhibited internal scatter on the order of 0.5-0.7 %/mm. This may be due to O<sub>2</sub> bubbles, since the release of O<sub>2</sub> (in small quantities for small doses) has been widely reported in the literature.

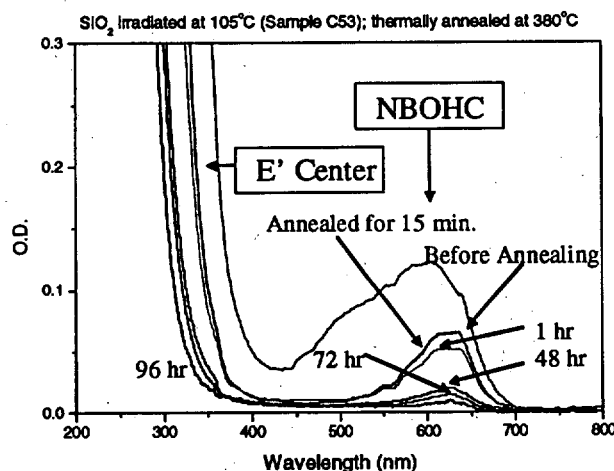


Fig. 2.3.1.1 Non-bridging oxygen hole centers (NBOHC) and E' centers are created and annihilated simultaneously.

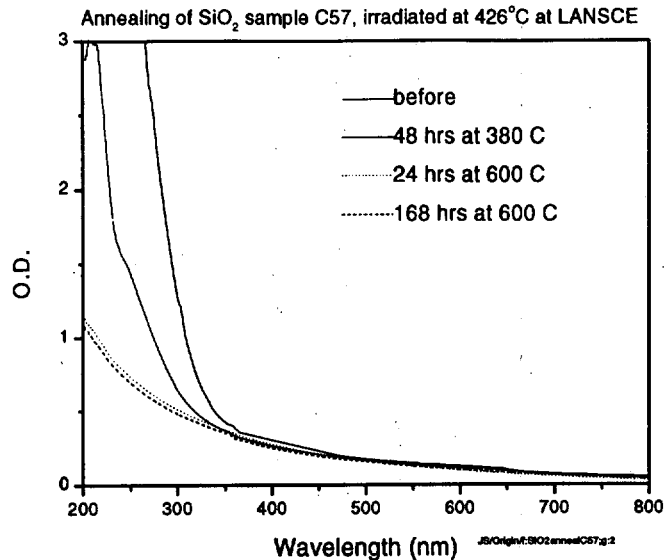


Fig. 2.3.1.2 Absorption spectra for SiO<sub>2</sub> sample irradiated at 426 °C. Note that while E' centers can be annealed, scattering, which is primarily a surface effect, cannot be annealed.

In summary, the LANSCE dose of  $10^{11}$  rads, corresponding to about 0.16 FPY (full-power-years) for an optic at a 20 m, causes (at 100-200 °C) a net absorption loss of 10%/mm and a scattering loss of <1%/mm. By employing optics 0.5 mm in thickness, the total loss becomes manageable at 6%. (It is moreover reasonable to employ SiO<sub>2</sub> optics as thin as 0.2 mm in thickness, although this would require additional development.) Fig. 2.3.1.3 shows a picture of a 1-mm-thick Fresnel lens that was fabricated from SiO<sub>2</sub>. Similar techniques could be used to produce large aperture IFE final optics.

It is suspected that the O<sub>2</sub> bubbles will not damage at the operating fluence of 2 J/cm<sup>2</sup>, although this is not certain. The optic is calculated to radiatively reach a steady-state temperature of 380 °C, taking the chamber view factor and ambient (75 °C) wall temperature into account.

The response of several additional optical materials is currently in the process of being evaluated at this time. They have been irradiated at ACRR at SNL (Annular Core Research Reactor), and include high-quality commercial-grade Al<sub>2</sub>O<sub>3</sub>, CaF<sub>2</sub>, and MgF<sub>2</sub> transmissive optics, as well as 3ω, 4ω and Al mirrors.

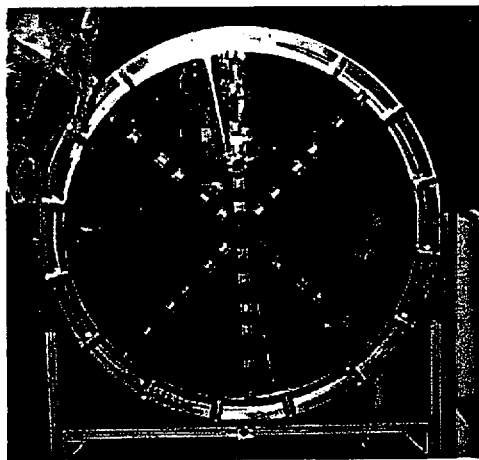


Fig. 2.3.1.3 High-efficiency, off-axis Fresnel lenses can be fabricated as thin as 0.5 mm with polishing. Thinner lenses can be produced via chemical etching in HF.



## 2.3.2 Molecular Dynamics Simulations of Neutron-Induced Defects

During FY01, Molecular Dynamics Simulations were used to confirm the experimental observation of radiation annealing in  $\text{SiO}_2$ . While this is a well-known behavior in metals, it had never been observed in an optical material. (It is noteworthy that the molecular potentials were available from prior work on optical damage of  $\text{SiO}_2$  performed for  $3\omega$  damage modeling of NIF optics.) Fig. 2.3.2.1 shows the track of a 2keV primary knock-on in  $\text{SiO}_2$ . While many structural defects are created, a significant number of them recombine on the order of picoseconds.

When the same location experiences another PKA (see Fig. 2.3.2.2), it is observed that the number of surviving defects does not increase, while the number of replacements is double that after only a single pulse. These initial results nicely support the radiation-annealing model, based on the observation that overlapping collisional cascades saturate after a single event. The difficulty of obtaining additional irradiations of high-energy neutrons makes the MDS calculation more important for finalizing our conclusions on the radiation-hardness of  $\text{SiO}_2$ .

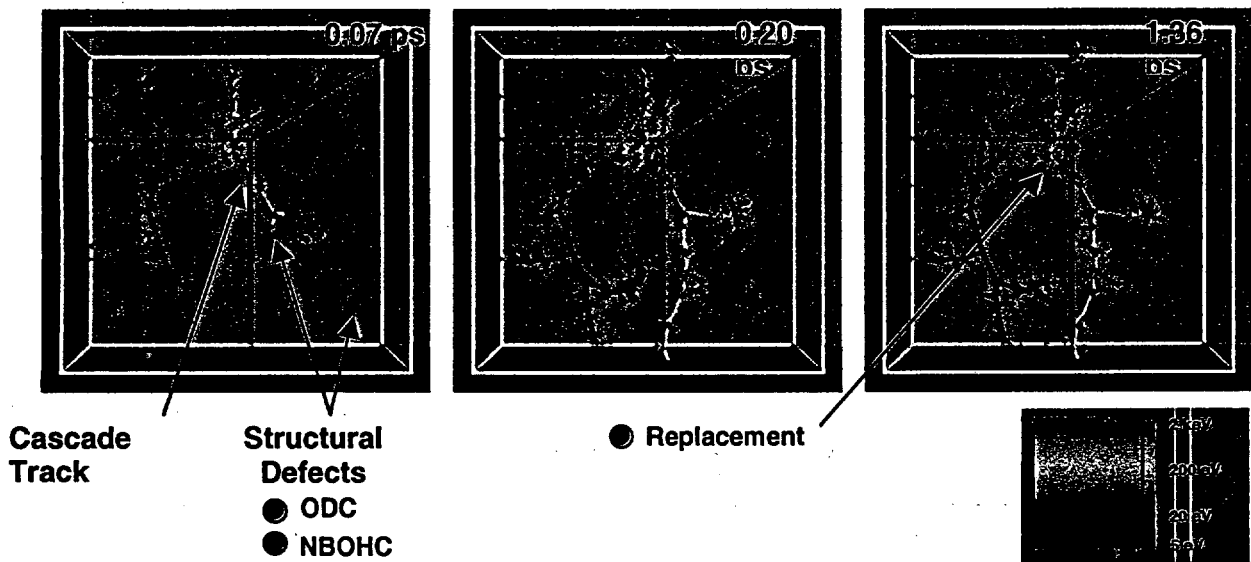


Fig. 2.3.2.1 A 2 keV cascade in fused silica rapidly forms many structural defects. On the order of picoseconds, however, many of these defects recombine.

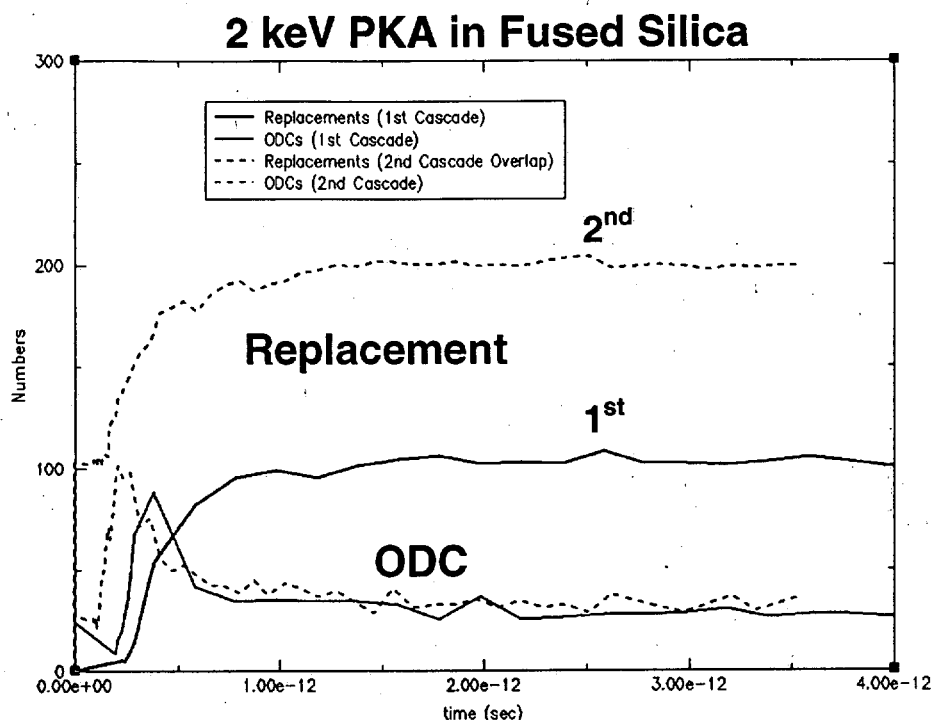


Fig. 2.3.2.2 After an initial surge in the production of structural defects, many defects recombine to reduce the number of surviving defects to the value observed after only a single pulse.

### 2.3.3 X-Ray Ablation of Optical Materials

The Falcon laser together with a Xe gas jet or metal target was proposed as moderate average power, x-ray source for investigating damage of target chamber components relevant to IFE. For example, the final optic in any high energy inertial fusion system is very sensitive to ablation from its surface, since material removal of  $< 1$  micron will adversely impact the quality of the optic. While IFE-relevant x-ray fluences are likely to be on the order of  $5 \text{ mJ/cm}^2$  (essentially below the single-shot ablation threshold), the repetitive nature of the damage experienced by the final optic ( $> 10^8$  shots) together with its sensitivity to sub-micron changes, suggest that experiments are needed to define the extent of this threat for a range of x-ray fluences. The FY01 goal was to generate  $\sim 5 \text{ mJ/cm}^2$  x-ray pulses in  $\sim 2$  nsec to explore the ablation of final optic sample surfaces. The tasks required to perform these experiments included: (1) modifying the Falcon laser to increase energy and reduce pulse length and to improve its reliability for long lifetime experiments and (2) integrate it with either an Xe gas jet or a moving solid copper wire to produce the desired x-rays at 10 Hz pulse repetition rates. Preliminary experiments on metal foils indicated that in order to meet the desired x-ray fluence, the target would have to be situated in close proximity to the x-ray source. Analysis indicated that for either Xe gas clusters or metal wire, it would be impossible to discern damage caused by laser generated x-rays from laser driven electron and ion damage. After operating the laser, performing preliminary metal foil experiments and analyzing the results to determine the feasibility of using Falcon as a high-brightness, high-average power x-ray source, it was determined in March that this effort should be stopped.

## 2.4 Target Physics

We have applied 2D and 3D radiation-hydrodynamics codes, developed in the Stockpile Stewardship Program, to the direct-drive targets of interest to the HAPL Program. These calculations test the capabilities in our 3D ASCI codes, help validate the codes for High Energy Density physics applications, and explore the optimization of targets for inertial fusion energy.

During this last year, we have calculated the output "threat" spectra for direct-drive targets with yields of 160MJ and 400MJ, driven with a KrF laser. The spectra include high-energy fusion burn products (gammas, neutrons, protons, deuterons, tritons, alphas, etc), capsule debris (i.e., ions from hydrodynamic expansion of target constituent materials in the keV-MeV range) and x-radiation. Our results led to the understanding that the dominant threat to the chamber walls are the target debris and burn product ions and *not* the emitted radiation as had been previously supposed. Our high-resolution studies of burn product transport have elucidated features of the physics of the nuclear interactions occurring within a burning target; an example is shown in Fig. 2.4.1 (for the 400MJ target).

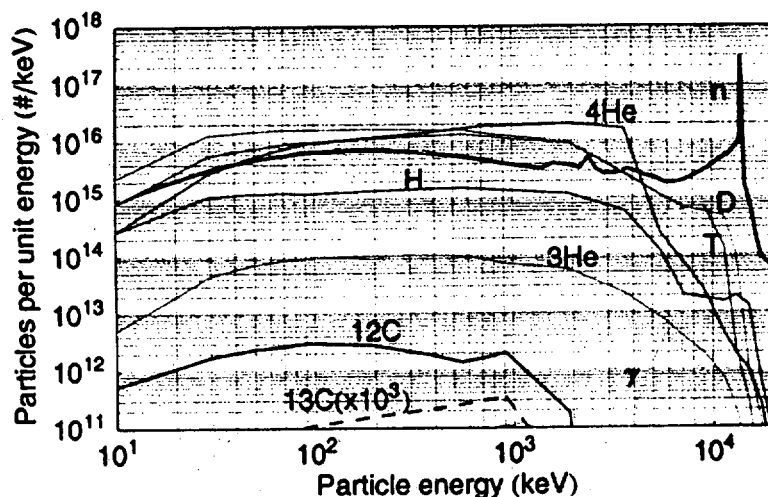


Fig. 2.4.1 Burn product spectrum from a 400MJ direct-drive target.

We have studied the 2D stability of several direct-drive capsule designs. Particular attention was paid to reducing numerical noise inherent in laser energy deposition when modeling the 2D single-mode growth rates. For the first time, we were able to demonstrate a full, time-dependent implosion to ignition with 2D laser ray-trace from time zero. Numerical noise growth amplitudes at the fuel/ablator interface at ignition were reduced to  $\sim 10^{-11}$ - $10^{-10}$  cm, comparable to that observed with indirect-drive targets driven by a uniform x-ray source. Calculated 2D growth factors were in good agreement with the Betti-Goncharov predictive model. An ancillary, Mathematica-based post-processor was developed to permit rapid estimation of the stability of such targets based on fits to 1D profiles.

Our present analyses predict that (single mode) growth factors peak around perturbation mode numbers of  $\ell \sim 250$ -300. However, when non-linear saturation models are applied, the dominant contribution to the RMS amplitude of final shell perturbation arises from mode numbers around  $\ell \sim 100$ . Employing such saturation models to reduce high frequency growth, and assuming initial surface roughness spectra from NIF specifications, we find final shell perturbations to be 30% of the shell thickness. However, if either (a) nonlinear saturation mechanisms are not so effective, (b) the initial roughness spectra are greater, or (c) laser imprint and ice inner surface roughness have comparable or greater contributions to growth, then final shell perturbation amplitudes will be larger. Thus, methods to ameliorate shell perturbations will form an important study area in the coming year. In particular, we need to delineate the interplay between saturated and unsaturated growth.

## 2.5 Table of Deliverables and Accomplishments

<b>3.1 DPSSL DEVELOPMENT</b>	<b>Deliverable:</b>	<b>Accomplishment:</b>
<b>3.1.1 Pump Delivery Systems</b>		
3.1.1.1 Diode Tiles	Produce and characterize 150 tiles.	100% Completed
3.1.1.2 Pulsed power and control system	Installation and full operation of 144 tiles with upgraded control system.	75% Completed Installation 144 tiles with upgraded control system. 72 tiles operational.
3.1.1.3 Pump delivery system	Full characterization and assembly of two pump delivery systems.	75% Completed Assembly of two pump delivery systems. Full characterization of one pump delivery system
<b>3.1.2 Fabricate Yb:S-FAP Crystals</b>		
3.1.2.1 Litton Airtron contract	Produce at least one high optical quality half-aperture crystal, with fourteen as goal.	100% Completed
3.1.2.2 LLNL crystal growth	Produce at least one high optical quality half-aperture crystal in cooperation with industrial partner.	100% Completed
3.1.2.3 Crystal bonding	At least one bonded and coated full size 4x 6 cm <sup>2</sup> Yb:S-FAP crystal, with seven as a goal.	75% Completed Two sub-size 3x 5 cm <sup>2</sup> Yb:S-FAP crystals bonded and coated. Two full size (4x6cm <sup>2</sup> ) bonded and in process of being coated.
<b>3.1.3 Build Wedged Amplifier Head</b>		
3.1.3.1 Wedged amplifier cassette	Activation of amplifier head with wedged Nd:glass surrogate slabs, and evaluation of performance.	50% Completed Activation of amplifier head with solid wedged vanes and evaluation of performance.
<b>3.1.4 Build Injection and Reverser Hardware</b>		
3.1.4.1 Injection and reverser hardware	Installation of injection and reverser hardware into main beamline.	100% Completed
3.1.4.2 Sub-aperture Pockels cell demonstration	Provide a Pockels cell that leads to a full aperture design.	100% Completed
3.1.4.3 Full-aperture Pockels cell design	Complete full aperture Pockels cell design, drawing and cost analysis package.	100 % Completed
<b>3.1.5 Integrated Tests and Code Benchmarking</b>		
3.1.5.1 Integrated system performance	Integrated operation of the laser system at 10 Hz repetition rate with Yb:S-FAP or 3 Hz with wedged Nd:Glass slabs	50% Completed Integrated tests at 0.1 Hz with non-wedged Nd:Glass slabs
3.1.5.2 Diagnostic packages	Full integration of diagnostics packages with laser and control systems.	75% Completed Four diagnostics packages completed. Integration into control system postponed
3.1.5.3 Ray trace and propagation codes	Comparison of experimental and theoretical predictions.	100% Completed
<b>3.1.6 Advanced Yb:S-FAP Crystal Growth</b>	Report on whether these two methods offer a pathway to large aperture Yb:S-FAP crystals.	100% Completed
<b>3.1.7 Laser Generation of Neutrons (Univ. Of Texas)</b>	Develop advanced gas jet to evaluate applicability of Mercury Laser parameters to laser neutron generation.	50% Completed Energy dependence verified, cluster size experiments in process.
<b>3.1.8 Spectral Sculpting Experiments and Evaluation of Average Power Frequency Conversion Design (Univ. of Rochester)</b>	Demonstrate efficacy of LCLV spectral sculptor. Develop a conceptual design of a frequency converter for Mercury.	100% Completed

<b>3.1 CHAMBERS DEVELOPMENT</b>	<b>Deliverable:</b>	<b>Accomplishment:</b>
<b>3.2 Chamber</b>		
3.2.1 Chamber Design	Documentation of design effort and progress.	75% Completed Preliminary assessment of fast ignition completed. Down selection to primary alternate chamber concept made. Initial assessment underway. Safety and environmental support provided to Materials Working Group. Required code modifications made that will enable tritium retention calculations in graphite first wall.
3.2.2 Systems Modeling	Documentation of model improvements and results of system and assessment studies.	100% Completed
<b>3.3 Final Optics</b>		
3.3.1 Gamma and Neutron Irradiation Studies	Quantitative measurements and analysis of candidate final optic materials extrapolating to IFE-relevant gamma ray and neutron doses. Evaluate the potential of radiation induced pulsed effects of relevance in NIF diagnostics.	75% Completed Measurements, analysis and design concept completed for fused silica. Gamma-ray irradiations and analysis completed for several materials. Analysis of additional neutron irradiated materials needed.
3.3.2 Molecular Dynamics Simulations of Neutron-Induced Defects	Modeling of neutron-damaged fused silica, including the type and amount of defects that are created.	100% Completed
3.3.3 X-ray ablation of optical materials	Quantitative x-ray ablation measurements and analysis of candidate final optic materials, and extrapolations to IFE-relevant x-ray doses.	25% Completed After performing preliminary experiments it was determined that this effort should be stopped due to the difficulty in discerning damage caused by laser generated x-rays from laser driven electron and ion damage.
<b>3.4 Target Design</b>	Documentation of design effort and progress.	100% Completed

### **3. PROGRAM PLAN DESCRIPTIONS**

#### **3.1 DPSSL DEVELOPMENT**

##### **3.1.1 Build Two Pump Delivery Systems**

A contract will be placed with Coherent to purchase diode bars, which will then be packaged at LLNL and mounted on a fluid-cooled support block. The pulsed power will be purchased and activated along with the computer control software. The optics and hardware to deliver the diode light to the amplifier will be assembled and tested. The goal of this effort is to build and characterize two 160 kW peak power pump delivery systems for the second amplifier.

###### **3.1.1.1 Diode Tiles**

A contract will be placed with Coherent to deliver up to 4000 diode bars. The diode bars will be mounted onto silicon-molybdenum submounts or "tiles". Each tile can hold up to 23 bars for a total peak power of 2.3 kW. The silicon submounts are precision etched at LLNL and provide the diodes with a thermally conductive heat path to the cooled support block. The tiles will be characterized under Mercury conditions for power, wavelength and reliability. We expect to produce an additional 150 tiles by the end of CY02.

###### **3.1.1.2 Pulsed power and control system**

Power supplies and pulsers will be purchased and installed along with the electrical wiring, timing, and trigger systems. The control system software will be upgraded to accommodate the additional tiles added to the system and allow for the operation of 8 backplanes or 640 kW of diode power

###### **3.1.1.3 Pump delivery system**

Two pump delivery systems will be assembled for the second amplifier head. The pump delivery system includes a diode light shield, focusing lens, lens duct, and homogenizer. The lens duct serves to condense the diode light into the required  $3 \times 5 \text{ cm}^2$  aperture and provide uniform divergence of the pump light. The homogenizer smoothes the spatial profile while maintaining the polarization and divergence. Measurements of the angular divergence, polarization, power and uniformity of the diode pump light exiting different stages of the pump delivery system will be made. Experimental data will be compared with ray-trace code predictions.

##### **3.1.2 Fabricate Yb:S-FAP Crystals**

A contract will be placed with Litton Airtron to grow half-size crystals. The crystals are precision oriented and then bonded together through a contract with Onyx Optics to produce full-size ( $4 \times 6 \times 0.75 \text{ cm}^3$ ) crystalline slabs. The crystals are then finished to the desired geometrical shape, precision polished, and anti-reflection coated before they are mounted into the amplifier vanes. The vanes are aerodynamic support structures that allow the crystals to be gas cooled. Crystal growth efforts at LLNL will be primarily focused on production with limited focus on R&D. The goal of the CY02 effort is to produce seven full-size crystals.

###### **3.1.2.1 Crystal growth (Northrup Grumman)**

A contract will be placed with Northrup Grumman to produce crystalline boules from their Czochralski (CZ) furnaces. Each boule will be large enough to harvest two half-sized crystals. The crystals will be fully characterized in terms of doping, wavefront, and spectroscopic requirements. Our goal is to fabricate at least one high optical quality crystal.

#### **3.1.2.2 Crystal growth (LLNL)**

Two furnaces will be dedicated to producing crystals for slab fabrication while the third furnace will be used to continue exploring the impact of thermal gradient, doping, gas-purge, and rotation rate on the crystalline quality. The goal is to reduce core and surface defects. Information learned at LLNL will be shared with our industrial partners.

#### **3.1.2.3 Crystal fabrication**

Once a crystal has been cut and characterized and has been shown to meet Mercury specifications, the crystal will be sent to Onyx optics for optical bonding. This is a process that allows two crystals to be bonded together to form one substrate with no compromise to wavefront quality. This process has already been demonstrated on full-scale samples. Our goal is to use this process to fabricate 7 crystalline slabs. After the half-size crystals are bonded together, they are finished into wedged shaped slabs and coated with a low loss anti-reflection coating. The final step involves precisely mounting the wedged slabs and edge-cladding into the vane elements to complete the amplifier assembly.

#### **3.1.3 Build Second Wedged Amplifier Head**

A second amplifier head will be built to accommodate a wedged vane structure. The current helium gas cooling system will be modified to accommodate the second head along with the control system software.

##### **3.1.3.1 Wedged amplifier cassette**

The second amplifier head will be built and installed. The amplifier hardware will be constructed with inverted flow conditions with respect to the first amplifier head. This will allow for compensation of the wavefront distortions generated from the first amplifier. The piping, vibration isolation hardware, and control system interfaces will be installed. Flow tests will be conducted with solid aluminum vanes to ensure that the flow conditions do not induce vibrations in the system.

#### **3.1.4 Build Full Scale Reverser**

The reverser hardware and will be tested with a full-aperture average power 100W, and high extinction (>98%) Pockels cell. The goal of this effort is to demonstrate that isolation optics provide adequate protection from parasitics that can otherwise damage the laser during operation.

##### **3.1.4.1 Reverser hardware**

The reverser hardware was originally constructed with a half-aperture beam footprint in order to accommodate the prototype half-aperture Pockels cell developed in FY01. The primary purpose of the reverser is to re-inject the beam back into the beamline for two more passes. The Pockels cell helps prevent the build-up of amplified spontaneous emission (ASE) and prevent ghosts from recirculating in the cavity and cause damage. The injection hardware and optics will be upgraded to allow for the insertion of a full-aperture optics Pockels cell.

##### **3.1.4.2 Full-aperture Pockels cell demonstration**

The isolation optics will include a full aperture KD\*P Pockels cell (3x5 cm<sup>2</sup> clear aperture), 45 degree rotators, and two polarizers. The design of the Pockels cell employs a set of alternating X-Y cut KD\*P crystals separated by a 90 degree quartz rotator. This arrangement compensates for the thermally induced birefringence incurred during high average power operation. The specifications require that the extinction be greater the 1:100 and that the wavefront distortion be less than 1/10 wave. In addition to the optical specifications, an in-house power supply and charging circuitry with the capability of less than ten nanosecond charging and discharging times will be tested with the full aperture cell.

#### **3.1.4.3 Kilowatt Integrated Research Experiment (IRE) class Pockels cell design**

The design of a full aperture Pockels cell of an IRE will require scaling the full-aperture design to accommodate three-times larger aperture crystals and ten-times higher average power while maintaining the same cooling capacity. Designs that can potentially meet these requirements will be investigated and summarized in a written report.

#### **3.1.5 Integrated Tests and Code Benchmarking**

This milestone involves the simultaneous activation of the front end, reverser, pump delivery and one fully populated (with Yb:S-FAP) amplifier system, along with the diagnostics packages required to diagnose the energy, pulse shape, wavefront, near-field and far-field of the amplified beam. Experimental data will be benchmarked against ray trace and propagation codes. The goal of this milestone is to validate the Mercury architecture and demonstrate integrated performance with one Yb:S-FAP amplifier head by producing 20 J of output energy at 1047 nm at 10 Hz repetition rate.

##### **3.1.5.1 Integrated system performance**

The simultaneous activation of the front end, injection, reverser, amplifier, and pump delivery subsystems will be demonstrated by injecting a seed beam from the front end into the beamline and tracking the beam throughout the system. The beam energy, pulseshape, wavefront, and nearfield will be monitored on each pass to determine that the beam is properly aligned and the amplifiers are suitably pumped. A front-end energy of 300 mJ, Gaussian in time but uniform in space is predicted to produce up to 20 J of output energy at 1047 nm at a 10 Hz repetition rate, with seven Yb:S-FAP crystals installed in the amplifier head.

##### **3.1.5.2 Diagnostic packages**

A second set of diagnostics packages will be deployed to help monitor the beam characteristics during the 4-pass amplification process. The packages will be identical to those developed in FY01. The packages will be placed in the laser system to diagnose the beam after the third pass and at the output. These packages will allow the beam energy, pulseshape, farfield, nearfield, darkfield, and wavefront to be measured. Tests will be performed to ensure adequate timing and control system software interfaces have been deployed.

##### **3.1.5.3 Ray trace and propagation codes**

The pump delivery characterization will provide experimental data in which to validate the ray trace codes used to design the hardware. The experimental near-field intensity pattern at the output of the lens duct and homogenizer will be compared with the ray trace predictions. The diagnostics package will provide experimental data with which to benchmark the propagation code. The propagation code tracks the energy, temporal pulseshape, near-field, and wavefront of the beam as it passes through every optic. Validation of this code will provide confidence in designing next generation systems such as the IRE.

#### **3.1.6 Advanced Yb:S-FAP Crystal Growth**

We will continue to perform tests to define the pathway to growing larger crystals of Yb:S-FAP. Our current Czochralski growth method will be modified to produce a nearly flat interface between the melt and crystal. The advantage of this approach is that the core defects can be eliminated and a full size slab can be cut directly out of the center of the boule. The disadvantage is that the crystal growth furnace must have enhanced stability to avert the formation of defects. We will continue investigating scaling techniques to grow up to 5 cm sized boules with repeatability and scalability.

Secondly, we will continue our efforts to grow larger crystals by the Heat Exchanger Method (HEM). In this method a small crystal is placed in the bottom of a container with a melt above it and the crystal is grown upward by gradually increasing the cooling applied to the seed and lowering the furnace temperature. Current as-grown crystals have been brownish in color due to what is believed to be color centers. However, we have found that the brownish color can be eliminated by an annealing process to



yield good quality material. Combined with this annealing process this method could also prove successful in producing up to 5 cm sized slabs. We will focus on increasing the size of the boules to 5 cm diameter and on eliminating the brownish color during the growth step, which is believed to be feasible.

### **3.1.7 Facility Upgrades**

The Mercury Laser facility will require additional utilities, electrical connections to support added pulsed power, and optical tables for laying out the second amplifier system optics and hardware. Plumbing and insulated piping for the diode chillers and second helium gas system will be installed. Vibration isolation pads and bellows will be added to help dampen and isolate mechanical vibrations. Existing optical tables will be shifted in order to accommodate the insertion of new tables and the second amplifier head assembly.

## 3.2 CHAMBERS

An inertial fusion energy chamber must perform several functions: it must contain the fusion energy pulse, convert the fusion power to thermal power at a temperature suitable for efficient electricity production (or possibly provide for direct conversion of part of the output), and breed tritium. Design of the chamber requires close interaction and integration with the target design (characterization of output spectrum), target injection and tracking systems (target survival in chamber, precision requirements), and the laser design (illumination geometry, beam port requirements, beam propagation through chamber). One of the most difficult challenges for chamber design is development of a first wall that can withstand or be protected from the x-rays, ions, and neutrons emitted by the target. This challenge is equally important in rep-rated target experiments and radiation sources for defense research.

We will continue to work on concept development, assessments, experimental planning for chamber concepts other than the gas-protected, dry-wall design employed by Sombrero. This work will be focused primarily on a magnetically protected chamber, but we will also address some of the key issues (advantages and disadvantages) related to implementation of fast ignition for laser IFE. As needed, we will provide general safety and environmental support to the overall HAPL program as well as to the Materials Working Group and the magnetically protected chamber design effort. Modeling of the damage and tritium retention caused by neutron irradiation of graphite will continue. Finally, we will continue to enhance our efforts on systems modeling for laser IFE power plants in coordination with modeling efforts at NRL and overall plant modeling efforts by the ARIES team.

### 3.2.1 Magnetic Protection

Design a chamber employing magnetic deflection to increase options for chamber wall materials, protect the chamber and final optics against damage from embedded ions, reduce/eliminate the threat of tritium co-deposition, and/or increase overall plant efficiency.

3.2.1.1 Install and learn to operate Lsp, a 3-D PIC code, on the PC. Work with Mission Research personnel to generate a relevant geometry input file and select the appropriate cross section libraries. Initial scoping calculations will be performed on the PC, but production runs will be run on the supercomputers at NERSC in Berkeley, where Lsp is already running.

3.2.1.2 Benchmark Lsp results against those obtained previously by John Perkins in collaboration with General Atomics (using a code that is not available to us). This calculation assumed a cusp magnetic field and no background gas. It was completed for 20 keV protons with 2 keV thermal spread and a field strength of 5 T at the coils.

3.2.1.3 Calculate the time-of-flight spread (i.e., no external magnetic field) of the burn and debris ions at the first wall. Compare these results to those obtained by LASNEX and BUCKY.

3.2.1.4 Use LASNEX to examine the extent of gas ionization and its effect upon the charged particle stopping power. LASNEX will be used to provide the charged particle fluences, per shot, at the chamber wall and optics assuming 10 mTorr of Xe gas and radii of 6.5 and 30 m, respectively.

3.2.1.5 Run Lsp for a case with an ideal magnetic field (mirror) and vacuum conditions. Calculate charged particles trajectories, collection efficiency, confinement time, and fluxes at the exit ports as a function of time and magnetic field strength.

3.2.1.6 Perform shielding, nuclear heating, radiation damage, and neutron activation calculations for NbTi superconducting magnets. Estimate total cold mass, cooling requirements, radiation lifetime, and radioactive waste.

3.2.1.7 Use OPERA3D (finite element code) to generate the mesh for the external field resulting from various coil configurations. This mesh will be fed into Lsp and used to update the results obtained in task (3.2.1. 5).

3.2.1.8 Use the Vector Fields code SCALA in an iterative fashion with OPERA3D to include effects that the expanding plasma ball will have upon the external magnetic field. Update the results obtained in tasks (3.2.1. 5) and (3.2.1. 7).

3.2.1.9 Propose experiments and calculations that could be performed to benchmark Lsp (coordinate this proposal with UCSD or other groups with relevant experimental capabilities).

3.2.1.10 Report with risk/benefit analysis and recommendations for future work, if any.

### 3.2.2 Fast Ignition

Assess laser-IFE power plant implications of fast ignition. Fast ignition offers the *possibility* of a significantly reduced plant size and cost as well as what *may be* a more affordable development path. These possibilities, however, are unproven. The advantages, disadvantages, and risks of fast ignition need to be evaluated on an integrated, self-consistent basis.

3.2.2.1 Continue literature review including gathering most recent info from IFSA2001 conference that features several papers on the subject.

3.2.2.2 Obtain best estimate of DT ice surface roughness that can be tolerated (through collaboration with John Perkins). If a significantly higher roughness is tolerable, the need for enhanced layering may be eliminated and/or target fabrication may be simplified. This may also enable the use of hard-frozen targets, which would be less susceptible to heating during target injection.

3.2.2.3 Consult with General Atomics on target fabrication issues. Key issues to be covered include fabrication of the cone-focused indirect-drive target and alternate techniques for target fill. Alternate techniques for target fill may help reduce tritium inventories in the target fabrication facility.

3.2.2.4 Assess the laser pointing and timing requirements and the implications for target injection, tracking and beam steering. The target injection analysis will account for the delay between the compression and ignitor beams.

3.2.2.5 Complete basic beam and chamber layout. This task must account for the very high intensities required for the ignitor beams, which will push the design to multiple lasers. The layout also must include consideration of the background gas pressure that is allowable for the ignition beams. Finally, this task will assess the compressor beam layout benefits provided by fast ignition (e.g., are the symmetry requirements significantly reduced such that the beam layout enables use of a significantly smaller building?).

3.2.2.6 Evaluate of potential for directional target output and its effects upon the chamber and optics if the cone-focused target is used.

3.2.2.7 Assess chamber design implications of FI target emissions compared to direct drive targets.

### **3.2.3 Safety and Environment**

Provide safety and environmental support to the overall HAPL Program (including the Materials Working Group) as well as to the LLNL effort in Chamber Studies. Collaborations with INEEL are important in this area.

3.2.3.1 Provide neutron and gamma-ray transport and activation calculations for the magnetically protected chamber design concept. Calculations will be needed to estimate the required shielding, nuclear heating of the magnets and shielding (yields cooling requirements), and neutron activation of the magnets and shielding.

3.2.3.2 Provide neutron and gamma-ray transport and activation calculations for either a direct conversion system or ion dump.

3.2.3.3 Provide the Materials Working Group with ongoing support in the selection of chamber and target materials. Support will be provided on an as-needed basis.

### **3.2.4 Radiation Damage Modeling for Chamber Materials**

Develop predictive capability for assessment of the macroscopic effects of neutron-induced radiation damage in IFE chamber wall materials. Computational capability will include means to predict generation, migration, and agglomeration of vacancies within graphite and other carbon-based materials as well as a model for hydrogen and tritium retention by such materials. This work leverages highly off of radiation damage work on fused silica.

3.2.4.1 Calculate activation energies for hydrogen and tritium transport and detrapping in graphite. Activation energies will be calculated using the bond-order potentials implemented in FY01.

3.2.4.2 Calculate migration and binding energies of H with vacant sites, single vacancies and vacancy clusters, as well as migration energies of defects, vacancies and interstitials, produced during irradiation.

3.2.4.3 Compare values calculated in task (2) to experimental measurements whenever possible and to those values used in trapping models such as the two-region model of A.A. Haasz, et. al [A. A. Haasz et al., J. Appl. Phys. 77 (1995) 66].

3.2.4.4 Perform ab initio calculations for single defects in order to validate the empirical potential.

3.2.4.5 From molecular dynamics, calculate threshold displacement energies for graphite (The number of defects produced in graphite during irradiation is also an input parameter for models of defect production and migration.).

3.2.4.6 Using the threshold displacement energies (calculated in task (5)) in conjunction with the Kinchin-Pease formulation, estimate the total number of defects produced. Perform calculations for displacement cascades at higher energies to test the validity of the Kinchin-Pease approximation.

### **3.2.5 Systems Modeling**

Overall objective is to provide useful information to the laser IFE community, including a) identification of high leverage items to help make R&D decisions, b) evaluation of near-term integrated facilities, and c) consistent comparisons of laser IFE design options (different drivers/chambers/ target combinations). To accomplish this, we must update the existing systems models to account for new (last 10 years) information on drivers, chambers and target gain.

3.2.5.1 Update and improve DPSSL model which dates to 1994. For example, include beam smoothing, improve extraction model, and consider different architectures.

3.2.5.2 Incorporate improved KrF laser model from NRL (current model dates to Avco work in early 1990's) when it becomes available. For example, architecture scaling tied to physics; include current thinking on component cost and performance, etc.

3.2.5.3 Update target gain curves to reflect target physics results and include dependence on other laser parameters (e.g., number of beams).

3.2.5.4 Update Sombrero chamber model to reflect ARIES and HAPL results on chamber radius vs. protective gas density and target yield.

3.2.5.5 Incorporate new chamber design models (e.g., magnetic diversion) as they become available.

3.2.5.6 Review balance of plant and economics models and benchmark conventional subsystems (e.g., electric plant equipment) to MFE systems code.

3.2.5.7 Include option to use component costs that are appropriate for near term systems to allow evaluation of IRE design space.

3.2.5.8 Examine parameter space of IRE design options to define a limited number of attractive points for more detailed design effort.

3.2.5.9 Assess IFE power plant design space including impact of success in a) cost reduction R&D (e.g., diode costs, pulsed power), b) technology development R&D (crystal growth, hibachi lifetime), and c) performance (e.g., laser efficiency and target gain).

### **3.3 FINAL OPTIC**

#### **3.3.1 Gamma and Neutron Irradiation Studies**

Determine the operating window of reflective and transmissive optics that are exposed to the gamma and neutron radiation environment of IFE. Samples will be irradiated at ORNL and SNL.

3.3.1.1 Complete the analysis and write a detailed journal article on the deployment of a SiO<sub>2</sub> final optic.

3.3.1.2 Complete the irradiation studies of the Al<sub>2</sub>O<sub>3</sub> and MgF<sub>2</sub> transmissive optics, and the 3 $\omega$ , 4 $\omega$  and aluminum mirrors. Examine materials for scattering and absorptive losses. Consider alternative materials suggested by ORNL, and use the HFIR and ACRF facilities for irradiations. Develop models of defect formation and final optic operation.

#### **3.3.2 Molecular Dynamics Simulations of Neutron-Induced Defects**

Determine the operating window of reflective and transmissive optics that are exposed to the gamma and neutron radiation environment of IFE. Due to the difficulty in obtaining additional high-dose neutron irradiations, this program element will take on an increased importance in the overall optics development effort. This area leverages highly from work being performed on other projects, including the modeling of radiation damage for chamber wall materials.

3.3.2.1 Complete the Molecular Dynamics Simulations of  $\text{SiO}_2$ , including: systematic calculations of defect generation versus the neutron impact energy, varying the amount of overlap of collisional cascades (to understand the radiation-annealing mechanism), and increased primary knock-on collisional energy.

3.3.2.2 Begin evaluation of the neutron-induced damage of aluminum mirrors.

### 3.3.3 Rep-Rated X-Ray Ablation (New Program Element)

Overall objective is to develop and experimentally benchmark a predictive capability, which can be used to analyze x-ray ablation from optical and chamber wall materials. While one can design components to avert single-shot melting and/or vaporization, little data are available for many-shot exposures at sub-threshold fluences. Similarly, only limited knowledge exists on the effects that impurities, surface contamination, rough surfaces, and neutron/gamma-ray irradiation have upon x-ray ablation. Through use of the PLEX or related x-ray facility and further development of the ABLATOR code, our understanding of these areas will be advanced. Key collaborations in this area include: UCSD for reflective optics characterization and methods of producing and characterizing IFE-relevant surface contamination. LLNL's Laser Science and Technology Group for transmissive optics and optics characterization. LLNL's target design groups for IFE target output calculations.

3.3.3.1 Form the x-ray ablation Steering Committee to assist in setting of program priorities. Steering Committee will also provide access to national assets for pre- and post-irradiation testing of samples.

3.3.3.2 Develop detailed experimental plan. Elements of this plan include: materials of interest, application of experimental results using line energies to broader IFE output spectrum, diagnostic needs and capabilities, conduct of operations, phase-in of contaminated, non-uniform, and/or damaged samples, and collaborations and/or other facility users. Finally, the plan must include an exit strategy.

3.3.3.3 Procure, install, and operate the PLEX or related x-ray irradiation facility using nitrogen and xenon fill gases to produce x-rays at 113 and 430 eV.

3.3.3.4 Equip x-ray source with a suite of real-time diagnostics for characterization of the Z-pinch and x-ray output (e.g., current rise time, x-ray spectrometer, etc.). Obtain and/or identify available facilities for pre- and post-irradiation analysis of samples (e.g., profilometer, white-light interferometer, photon tunneling microscope, etc.).

3.3.3.5 Upgrade ABLATOR x-ray deposition model with coupling to a Monte Carlo particle transport code.

3.3.3.6 Characterize x-ray output (spectrum and pulse length) for the two fill gases with and without filters. Characterization must include repeatability.

3.3.3.7 Complete an experimental campaign for two leading materials in either the optics or chamber wall arena as suggested by the Steering Committee. If PLEX operations begin with optics, materials are likely to be aluminum mirrors and fused silica lenses. If operations begin with chamber wall materials, materials are likely to be graphite (C/C composite) and tungsten or a tungsten alloy. Campaign will begin with single-shot exposures and progress, in steps, to many ( $10^4$ - $10^5$ ) shot exposures: 1) Analyze samples to determine per-shot material removal depths (averaged and as a function of the number of shots) and removal mechanisms; 2) Upgrade ABLATOR, as needed, with new materials and removal models; 3) Benchmark ABLATOR against the experimentally measured material removal depths; 4) Apply ABLATOR using the full IFE x-ray output spectrum and predict annual material removal depths.

## **3.4 TARGET PHYSICS**

### **3.2.1 Target Design**

The target output spectra (burn products, X-rays and debris) will be characterized for several designs. We will continue assessing the impact of 2D hydrodynamic stabilities for baseline direct drive targets, including the coupling of single mode perturbations into the non-linear, saturated regime. Particular attention will be paid to the investigation of using thin, high-Z target coatings to ameliorate early-time laser imprint. Finally, calculations will be performed to investigate the wavelength-dependence of target gain for application to both DPSSL and KrF laser drivers.

## 4. STATEMENTS OF WORK AND DELIVERABLES

### 4.1 DPSSL DEVELOPMENT

#### 4.1.1 Build Two Pump Delivery Systems

##### 4.1.1.1 Diode Tiles

*Statement of work:*

Order diodes and fabricate tiles.

*Deliverable:*

Produce and characterize 150 tiles consisting of 23 diode bars per tile. Each amplifier will require 144 tiles for the 100 J, 2-amplifier system.

##### 4.1.1.2 Pulsed power and control system

*Statement of work:*

Purchase power conditioning hardware and implement control system upgrades.

*Deliverable:*

Installation and full operation consisting of at least  $1 \times 10^5$  shots for 144 tiles with the upgraded control system.

##### 4.1.1.3 Pump delivery system

*Statement of work:*

Purchase hardware and align pump delivery optics.

*Deliverable:*

Full characterization (nearfield, farfield, darkfield, polarization, power and wavelength) and assembly of two pump delivery systems.

#### 4.1.2 Fabricate Yb:S-FAP Crystals

##### 4.1.2.1 Crystal growth (Northrup Grumman)

*Statement of work:*

Place crystal growth contract with Northrup Grumman, and help guide operations.

*Deliverable:*

Produce at least one high optical quality crystal, with three as goal.

##### 4.1.2.2 Crystal growth (LLNL)

*Statement of work:*

Upgrade CZ furnaces, explore fundamental aspects of crystal growth, and share results with industrial partners.

*Deliverable:*

Produce seven high optical quality crystals.

##### 4.1.2.3 Crystal fabrication

*Statement of work:*

Deliver crystals to Onyx Optics for bonding. Following bonding process, have crystals polished and anti-reflection coated.

*Deliverable:*

Produce seven bonded and coated full-size  $4 \times 6 \text{ cm}^2$  Yb:S-FAP crystals.



### **4.1.3 Build Second Wedged Amplifier Head**

#### **4.1.3.1 Wedged amplifier cassette**

*Statement of work:*

Design and fabricate wedged amplifier head.

*Deliverable:*

Activation of second amplifier head with seven Nd:glass surrogate slabs, and evaluation of flow performance. Replace with Yb:S-FAP slabs as they become available.

### **4.1.4 Build Full Scale Reverser**

#### **4.1.4.1 Reverser hardware**

*Statement of work:*

Assemble and align full scale reverser hardware with one-to-one magnification optics.

*Deliverable:*

Installation of injection and reverser hardware into main beamline.

#### **4.1.4.2 Full-aperture Pockels cell demonstration**

*Statement of work:*

Assemble and test full aperture (3x5 cm<sup>2</sup> clear aperture) Pockels cell and high voltage Pockels cell driver.

*Deliverable:*

Integrate full aperture Pockels cell into reverser system.

#### **4.1.4.3 Kilowatt IRE class Pockels cell design**

*Statement of work:*

Produce conceptual design for a Kilowatt IRE aperture Pockels cell.

*Deliverable:*

Complete conceptual design of IRE aperture (10x15 cm<sup>2</sup>) Pockels cell and high voltage driver.

### **4.1.5 Integrated Tests and Code Benchmarking**

#### **4.1.5.1 Integrated system performance**

*Statement of work:*

Simultaneous activation of sub systems (front end, reverser, one amplifier, and pump delivery systems).

*Deliverable:*

Integrated operation of the laser system at 20 J and 10 Hz repetition rate with Yb:S-FAP slabs in one amplifier head.

#### **4.1.5.2 Diagnostic packages**

*Statement of work:*

Assemble and test two diagnostic packages.

*Deliverable:*

Full integration of diagnostics packages with laser and control systems.

#### **4.1.5.3 Ray trace and propagation codes**

*Statement of work:*

Experimental data will be compiled, entered into theoretical codes, and used to generate realistic predictive capabilities.

*Deliverable:*

Comparison of experimental and theoretical predictions.

#### **4.1.6 Advanced Yb:S-FAP Crystal Growth**

*Statement of work:*

Attempt to grow at least one >5cm S-FAP crystal employing the flat-interface Czochralski growth and HEM technique.

*Deliverable:*

Report on whether these methods offers a pathway to large-aperture Yb:S-FAP crystals.

#### **4.1.7 Facility Upgrades**

*Statement of work:*

Facility work will be conducted to add electrical connections, plumbing, piping, pulsed power and optical tables in preparation for installation and testing of the second amplifier head.

*Deliverable:*

Full installation, operation, and interface of diode chillers and helium gas blower to control system.

### **4.2 CHAMBERS**

#### **4.2.1 Magnetic Protection**

*Statement of Work:* Complete initial assessment of using magnetic protection for the chamber wall and final optics.

*Deliverable:* Document design effort and suggest future analysis and experiments.

#### **4.2.2 Fast Ignition**

*Statement of Work:* Demonstrate opportunities and challenges offered by laser IFE fast ignition.

*Deliverable:* Document findings and suggest key areas of future research and development.

#### **4.2.3 Safety and Environment**

*Statement of Work:* Provide safety and environmental support to other elements within the HAPL program such as the Materials Working Group and the magnetically protected chamber design.

*Deliverable:* As needed, identify and address key safety and environmental issues.

#### **4.2.4 Radiation Damage Modeling for Chamber Materials**

*Statement of Work:* Perform mechanistic modeling of neutron-induced knock-on damage for graphite and relate the results to experimental data.

*Deliverable:* Modeling of neutron-damaged graphite, including the type and amount of defects that are created and tritium retention that would result.

#### **4.2.5 Systems Modeling**

*Statement of work:* Improve systems modeling for laser IFE power plants and conduct system studies. Continue assessment of future energy market place and IFE's role.

*Deliverable:* Documentation of model improvements and results of system and assessment studies

### **4.3 FINAL OPTIC**

#### **4.3.1 Gamma and Neutron Irradiation Studies**

*Statement of Work:* Perform neutron and gamma radiation tests of transmissive optics as well as baseline reflective optics such as Al and dielectric mirrors. Relate these results to requirements of the final optic element.

*Deliverable:* Quantitative measurements and analysis of candidate final optic materials extrapolating to IFE-relevant gamma ray and neutron doses.

#### **4.3.2 Molecular Dynamics Simulations of Neutron-Induced Defects**

*Statement of Work:* Perform mechanistic modeling of neutron-induced knock-on damage for final optic materials and relate the results to experimental data.

*Deliverable:* Modeling of neutron-damaged optical materials, including the type and amount of defects that are created.

#### **4.3.3 Rep-Rated X-Ray Ablation**

*Statement of Work:* Analytically and experimentally investigate pulsed x-ray irradiations effects in optical (and chamber wall, where feasible) materials. Relate results to IFE-relevant conditions and requirements for each candidate material.

*Deliverable:* Complete a campaign of exposures, culminating in a series of  $10^4$ – $10^5$  pulses, for two candidate optical and/or chamber wall materials. Report findings in a peer-reviewed journal.

### **4.4 TARGET PHYSICS**

#### **4.4.1 Target Design**

*Statement of Work:*

Perform calculations for direct-drive targets employing thin films to reduce imprint, and evaluate the wavelength dependence and “threat spectra.” Continue assessing the impact of 2D hydrodynamic instabilities.

*Deliverable:*

Provide documentation of direct-drive target performance in terms of gain, threat spectra, and the utility of metal film.

## **5. COST BY ELEMENT (Total = \$10,094,000)**

### **5.1 DPSSL DEVELOPMENT (Total = 8,330,000)** *(Major procurements listed)*

<b>5.1.1</b>	<b>Build Two Pump Delivery Systems</b> <i>(Diodes: Coherent, \$640k, Pulsers: DEI, \$250k)</i>	<b>\$2,425,000</b>
<b>5.1.2</b>	<b>Fabricate Yb:S-FAP Crystals</b> <i>(Crystals: Northrup, \$300k, Fab: \$500k, Power supplies, Pillar: \$170k)</i>	<b>\$1,998,000</b>
<b>5.1.3</b>	<b>Build Second Wedged Amplifier Head</b>	<b>\$750,000</b>
<b>5.1.4</b>	<b>Build Full Scale Reverser</b>	<b>\$682,000</b>
<b>5.1.5</b>	<b>Integrated Tests and Code Benchmarking</b>	<b>\$1,142,000</b>
<b>5.1.6</b>	<b>Advanced Yb:S-FAP Crystal Growth</b> <i>(Crystals: Crystal Systems: \$100k)</i>	<b>\$300,000</b>
<b>5.1.7</b>	<b>Facility Upgrades</b> <i>(Utilities: Bay Voltex, \$100k)</i>	<b>\$1,033,000</b>

### **5.2 CHAMBER (Total = 539,000)**

<b>5.2.1</b>	<b>Magnetic Protection</b>	<b>\$245,000</b>
<b>5.2.2</b>	<b>Fast Ignition</b>	<b>\$49,000</b>
<b>5.2.3</b>	<b>Safety and Environment</b>	<b>\$49,000</b>
<b>5.2.4</b>	<b>Radiation Damage Modeling for Chamber Materials</b>	<b>\$98,000</b>
<b>5.2.5</b>	<b>Systems Modeling</b>	<b>\$98,000</b>

### **5.2 FINAL OPTIC (Total = 931,000)**

<b>5.3.1</b>	<b>Gamma and Neutron Irradiation Studies</b>	<b>\$147,000</b>
<b>5.3.2</b>	<b>MDS of Neutron-Induced Defects</b>	<b>\$98,000</b>
<b>5.3.3</b>	<b>Rep-Rated X-Ray Ablation</b>	<b>\$686,000</b>

### **5.4 TARGET PHYSICS (Total = 294,000)**

<b>5.4.1</b>	<b>Target Design</b>	<b>\$294,000</b>
--------------	----------------------	------------------

## 6. TECHNICAL CONTRIBUTORS TO THIS PLAN

### Lawrence Livermore National Laboratory

Andy Bayramian (Lead Experimentalist)  
Camille Bibeau (Mercury Project Leader)  
Ray Beach (Diodes, Laser Modeling)  
Bill Behrendt (Control System)  
Chris Ebberts (Pockels Cell)  
Jeff Latkowski (Fusion Materials)  
Wayne Meier (Chambers, System Modeling)  
Stephen Payne (Associate Program Leader)  
John Perkins (Target Physics)  
Kathleen Schaffers (Crystal Growth)  
Ken Skulina (Mercury Project Engineer)

### LLNL Managers:

Lloyd Hackel (Program Leader for Laser Science and Technology)  
John Lindl (Program Manager for MFE and IFE)

### University of Texas (Laser Neutron Generator)

Todd Ditmire

### University of Rochester (Spectral Sculpting)

Jack Kelly  
Leon Waxer

### Coherent, Inc.(Didoes)

Paul Rudi

### Northrup Grumman (Crystals)

Mark Randles  
David Witter

### Onxy Optics, Inc. (Diffusion Bonding)

Helmuth Meissner  
Oliver Meissner

This work was performed under the auspices of the U.S. Department of Energy by the University of California, Lawrence Livermore National Laboratory under Contract No. W-7405-Eng-48.